EFFECT OF CHARGING/DISCHARGING ON PLASTICITY AND FRACTURE IN Si ANODES FOR BATTERIES

THÈSE N^{O} 7506 (2017)

PRÉSENTÉE LE 20 JANVIER 2017
À LA FACULTÉ DES SCIENCES ET TECHNIQUES DE L'INGÉNIEUR
LABORATOIRE DE MODÉLISATION MÉCANIQUE MULTI-ÉCHELLE
PROGRAMME DOCTORAL EN MÉCANIQUE

ÉCOLE POLYTECHNIQUE FÉDÉRALE DE LAUSANNE

POUR L'OBTENTION DU GRADE DE DOCTEUR ÈS SCIENCES

PAR

Seyed Mostafa KHOSROWNEJAD

acceptée sur proposition du jury:

Prof. J. Botsis, président du jury
Prof. W. Curtin, directeur de thèse
Prof. B. Sheldon , rapporteur
Prof. T. Pardoen, rapporteur
Prof. M. Ceriotti, rapporteur

ÉCOLE POLYTECHNIQUE
FÉDÉRALE DE LAUSANNE
Suisse
2017

Abstract

Lithium-ion batteries provide the power for portable electronics and found many other interesting applications, such as in electric vehicles. It is desirable to design batteries with high energy density, long cycle life and safe operation. Silicon is among the highest Li-storing anode materials in Li-ion batteries, but the large capacity is accompanied by significant volume expansion that causes mechanical failure and capacity fading after few charging/discharging cycles. Crystalline silicon undergoes a phase change into amorphous silicon during the first lithiation cycle and there is evidence that the mechanical behavior of lithiated silicon depends on the history of charging and discharging. The goal of this thesis is to better understand the mechanical properties and behavior of lithiated silicon, specifically the dependence of its properties on the state of charging/discharging, through atomistic simulation, constitutive modelling and finite elements method calculations.

Every lithiation cycle is accompanied by significant swelling and shrinkage of the silicon anode. These large strains are accommodated by plastic flow. Amorphous high-storage-capacity Li-Si flows at lower stresses than crystalline materials but there is evidence that the plastic flow stress decreases with charging and discharging, indicating important non-equilibrium aspects to the flow behavior. In this thesis, a mechanistically-based constitutive model for rate-dependent plastic flow in amorphous materials, such as $\mathrm{Li}_x\mathrm{Si}$ alloys, during charging and discharging is developed based on two physical concepts: (i) excess energy is stored in the material during electrochemical charging and discharging due to the inability of the amorphous material to fully relax during the charging/discharging process and (ii) this excess energy reduces the barriers for plastic flow processes and thus reduces the flow stress. The existence of such an excess energy within the atomic structure of the silicon along with potentially long relaxation time would help rationalize the strong hysteresis observed in experimental measurements of the electrochemical potential during charge/discharge cycles. Plastic flow stress in our model is a result of a competition between the time scale of charging/discharging and the time scale of glassy relaxation. The two concepts, as well as other aspects of the model, are validated using molecular simulations on a model Li-Si system.

The model is applied to examine the plastic flow behavior of realistic geometries using the finite element method. I develop and implement a finite element method to capture the full complexity of coupled chemical-mechanical evolution including plastic flow that arises in these amorphous battery materials.

Fracture is the main cause of degradation and capacity fading in lithiated silicon during cycling and recent experimental studies on the fracture of lithiated silicon show conflicting results, thus it is essential to develop mechanistic models for the fracture of Li_xSi to interpret the experiments and facilitate the design. In this thesis I perform systematic atomistic simulations of crack propagation for three different Li compositions ($x = 0.5, 1.0, 1.5$ in Li_xSi) and three discharged samples ($x = 0.5$ discharged from $x_\infty = 1.0, 1.5$ and $x = 1.0$ discharged from $x_\infty = 1.5$ in Li_xSi). I measure similar fracture energies for all as quenched samples, with void nucleation and coalescence observed to be the primary mechanism of crack growth. With increasing Li content, the plastic flow stress decreases but the material becomes more susceptible to void nucleation and growth.

Because of the similarities between the fracture mechanism of Li_xSi and ductile fracture, Gurson's model is used to help interpret the simulation results. Quantitative agreement between the trends predicted by Gurson's model based fracture simulations and MD simulations of cracks in Li_xSi is demonstrated. Gurson-type models predict that the fracture energy scales with the yield stress and void spacing D ($J_I = \alpha\sigma_y D$, $\alpha \simeq 1$). In all tested cases the nucleated voids spaced within few nanometers of the crack tip, which explains the low fracture energy of Li_xSi as it scales with spacing of the voids. Thus Li_xSi fracture brittle like despite its ability to flow plastically. Generalized plane-strain equi-biaxial expansion simulations of uncracked samples are performed to provide complementary information on the void nucleation and growth. We then investigate the effects of discharging on fracture, and show that the increased structural disorder generated by discharging decreases the flow stresses but facilitates void nucleation and growth. However, in all tested samples the fracture toughness and fracture energy is increased by discharging, indicating that the flow and fracture of lithiated silicon depends on the history of charging/discharging.

The contribution of this dissertation is twofold. First, a new mechanistically-based constitutive model for lithiated silicon is developed which considers the effect of charging and discharging on the plasticity. Second, I demonstrate the merit of Gurson's model of ductile fracture to qualitatively describe the fracture behavior of lithiated silicon and analyzed the effect of charging and discharging on fracture properties of silicon anodes.

Key words: Lithium-ion Battery, Plasticity, Fracture, Charging/Discharging, Excess energy

Zusammenfassung

Lithium-Ionen-Akkumulatoren speichern Energie für portable Elektrogeräte und haben viele andere interessante Anwendungen gefunden, zum Beispiel in Elektroautos. Bei der Entwicklung solcher Akkumulatoren sollen hohe Energiedichte, lange Lebensdauer und Betriebssicherheit angestrebt werden. Silizium ist eines der Anodenmaterialien mit der höchsten Speicherkapazität für Li-Ionen in Lithium-Ionen-Akkumulatoren, allerdings geht diese hohe Kapazität mit einer Volumenzunahme einher, die mechanisches Versagen und ein Nachlassen der Kapazität nach wenigen Ladezyklen zur Folge hat. Kristallines Silizium wird während der ersten Lithiumaufnahme in amorphes Silizium umgewandelt und es gibt Hinweise darauf, dass das mechanische Verhalten von lithiiertem Silizium von der Lade- und Entlade-Historie abhängt. Ziel dieser Arbeit ist es, die mechanischen Eigenschaften und das Verhalten lithiierten Siliziums, speziell die Abhängigkeit seiner Eigenschaften vom Lade- bzw. Entladezustand, besser zu verstehen. Dazu wird sich der atomistischen Simulation, konstitutiver Modellierung und Finite-Elemente-Rechnungen bedient.

Jeder Ladezyklus geht einher mit starkem An- und Abschwellen der Silizium-Anode. Diese großen Verformungen werden durch plastisches Fließen erreicht. Amorphes Li-Si mit hoher Speicherkapazität fließt bei niedrigeren Spannungen als kristallines Material, es gibt jedoch Hinweise darauf, dass die plastische Fließgrenze mit wiederholtem Laden und Entladen abnimmt, was auf wichtige Nichtgleichgewichtseffekte im Fließverhalten hinweist. In dieser Arbeit wird ein auf physikalischen Mechanismen basierendes Konstitutivgesetz zur Beschreibung des dehnratenabhängigen plastischen Fließens amorpher Materialien, wie etwa Li$_x$Si -Legierungen, während des Lade- und Entladevorganges hergeleitet. Es basiert auf zwei physikalischen Konzepten: (i) während der elektrochemischen Ladung und Entladung wird im Material überschüssige Energie gespeichert, weil es dem amorphen Material nicht möglich ist, während des Prozesses vollständig zu relaxieren, und (ii) diese überschüssige Energie reduziert die Schwelle für plastische Fließprozesse und deshalb die Fließspannung. Das Vorhandensein solcherlei überschüssiger Energie in der atomaren Struktur des Siliziums kann, zusammen mit einer möglicherweise langen Relaxationszeit, als Erklärung für jene ausgeprägte Hysterese dienen, die bei der experimentellen Messung des elektrochemischen Potenzials im Verlauf der Ladezyklen beobachtet wird. Die Fließspannung ist in unserem Model ein Ergebnis des Wettstreits zwischen der Zeitskala des Lade- und Entladevorgangs und der Zeitskala der glasartigen Relaxation. Diese beiden Konzepte, sowie andere Aspekte des Models, werden mittels Molekulardynamik-Simulation eines Li-Si-Modellsystems validiert.

Das Model wird dazu genutzt, das Fließverhalten realistischer Geometrien mit der Finite-

Elemente-Methode zu untersuchen. Ich entwickle und implementiere eine Finite-Elemente-Methode, um die gekoppelte chemische und mechanische Entwicklung in diesen amorphen Akkumulator-Materialien, einschließlich des plastischen Fließens, in ihrer gesamten Komplexität zu erfassen.

Bruch ist die Hauptursache für die Zersetzung und das Nachlassen der Kapazität von lithiiertem Silizium während des Zyklisierens. Aktuelle experimentelle Studien zum Bruchverhalten von lithiiertem Silizium kommen zu widersprüchlichen Ergebnissen, deshalb ist es äußert wichtig, mechanistische Modelle des Bruchverhaltens von $\mathrm{Li}_x\mathrm{Si}$ zu entwickeln, welche die Interpretation der Experimente gestatten und die Entwicklung vereinfachen.

In dieser Arbeit simuliere ich mit atomistischen Methoden systematisch die Rissausbreitung für drei verschiedene Li-Mischungen ($x = 0.5, 1.0, 1.5$ in $\mathrm{Li}_x\mathrm{Si}$) und drei Entladezustände ($x = 0.5$ entladen von $x_\infty = 1.0, 1.5$ und $x = 1.0$ entladen von $x_\infty = 1.5$ in $\mathrm{Li}_x\mathrm{Si}$). Ich messe bei allen abgeschreckten Proben ähnliche Bruchenergien und stelle fest, dass Bildung und Zusammenwachsen von Poren der wichtigste Mechanismus des Rissfortschritts ist. Mit zunehmendem Li-Anteil nimmt die Fließgrenze ab, jedoch wird das Material anfälliger für Porenbildung und -wachstum.

Aufgrund der Ähnlichkeit zwischen dem Bruchmechanismus von $\mathrm{Li}_x\mathrm{Si}$ und Verformungsbruch wird Gursons Model zur Interpretation der Simulationsergebnisse herangezogen. Es wird gezeigt, dass eine qualitative Übereinkunft besteht zwischen dem Trend, den auf Gursons Model basierende Risssimulationen voraussagen und jenem, den MD-Risssimulationen in $\mathrm{Li}_x\mathrm{Si}$ voraussagen. Gurson-Modelle sagen voraus, dass die Bruchenergie mit der Fließspannung und dem Porenabstand D skaliert ($J_I = \alpha\sigma_y D$, $\alpha \simeq 1$). In allen überprüften Fällen nukleierten Poren wenige Nanometer von der Rissspitze entfernt. Da die Bruchenergie mit dem Porenabstand skaliert erklärt dies die geringe Bruchenergie von $\mathrm{Li}_x\mathrm{Si}$. Deshalb bricht $\mathrm{Li}_x\mathrm{Si}$ trotz seiner Fähigkeit zum plastischen Fließen spröde. Ebene, äquibiaxiale Ausdehnung rissfreier Proben wird simuliert, um ergänzende Daten zu Porenbildung und -wachstum zu gewinnen.

Als nächstes untersuchen wir die Folgen der Entladung auf das Bruchverhalten und zeigen, dass die durch das Entladen zunehmende strukturelle Unordnung die Fließspannung senkt, aber auch Porenbildung und -wachstum erleichtert. Allerdings nehmen bei allen Proben die Bruchzähigkeit und die Bruchenergie mit dem Entladen zu, was darauf hindeutet, dass Fließen und Bruch von lithiiertem Silizium von der Lade/Entlade-Historie abhängen.

Die vorliegende Arbeit leistet zwei Beiträge zur Forschung. Erstens wird ein neues, auf physikalischen Mechanismen basierendes, Konstitutivgesetz für lithiiertes Silizium hergeleitet, welches den Einfluss von Ladung und Entladung auf die Plastizität berücksichtigt. Zweitens zeige ich den Nutzen von Gursons Model des Verformungsbruchs zur qualitativen Beschreibung des Bruchverhaltens von lithiiertem Silizium.

Stichwörter: Lithium-Ionen-Akkumulator, Plastizität, Bruch, Laden/Entladen, Überschussenergie

Contents

Abstract (English/Français/Deutsch) **i**

List of figures **vii**

List of tables **xiii**

1. Background and motivation **1**
- 1.1. Introduction . . . 1
- 1.2. Lithiation of Si in electrochemical processes . . . 2
  - 1.2.1. Stress growth and fracture during electrochemical process . . . 7
  - 1.2.2. Modeling of stress evolution and fracture in Li_xSi . . . 9
- 1.3. Outline of the thesis . . . 12

2. Effect of charging/discharging on the plastic flow of Li-Si alloys **13**
- 2.1. Introduction . . . 13
- 2.2. Plastic Softening in Amorphous Li_xSi due to Charging/Discharging . . . 15
  - 2.2.1. Mechanistic Concept and Formalism . . . 15
  - 2.2.2. Validation of the Mechanistic Concepts . . . 17
- 2.3. Constitutive Behavior . . . 21
  - 2.3.1. Rate-dependent Plastic Flow . . . 22
  - 2.3.2. Creation and Annihilation of Excess Energy . . . 24
  - 2.3.3. Chemical Potential and Stress . . . 25
  - 2.3.4. Implementation and Material Parameters . . . 26
- 2.4. Results . . . 27
  - 2.4.1. Tension Test on a Discharged Nanowire . . . 27
  - 2.4.2. Mechanical Response of a Constrained Thin Film during Discharging . . . 30
  - 2.4.3. Cyclic Discharging/Charging of a Constrained Thin Film . . . 32
  - 2.4.4. Discharging of a Thin Film: Composition-dependent Material Parameters 33
- 2.5. Conclusion . . . 34

3. Fracture in amorphous Li-Si alloys **37**
- 3.1. Experimental studies of fracture in Lithiated Silicon . . . 38
- 3.2. Theoretical background on crack growth in ductile fracture . . . 40
- 3.3. Atomistic simulations of fracture in Li_xSi . . . 43

3.3.1. Atomistic simulation of fracture: sample preparation and methods . . . 43
3.3.2. Clustering phenomenon for high lithium concentration 45
3.3.3. Fracture toughness atomistic simulations results of as prepared samples 46
3.3.4. Fracture mechanism in Li_xSi 48
3.4. Ductile fracture model for Li_xSi 50
3.4.1. Fundamental length scale in the fracture of Li_xSi 50
3.4.2. Cell model for fracture analysis of Li_xSi 52
3.4.3. Work of fractureLi_xSi 53
3.5. Effect of discharging on the fracture of Li_xSi 55
3.6. Discussion 58
3.7. Conclusion 61

4. Finite element model of elasto-plastic chemo-mechanics 63
4.1. Continuum thermodynamics of chemo-mechanical system 64
4.1.1. Governing equations 65
4.1.2. Dissipation principle and material law forms 65
4.2. Constitutive modeling of irreversible chemo-mechanics 66
4.2.1. Kinematics assumptions 66
4.2.2. Free energy form 67
4.2.3. Plastic strain and excess energy evolution 68
4.3. Finite element formulation for nolinear chemo-mechanics 68
4.3.1. A space-time discrete finite element formulation 68
4.3.2. Material state update algorithm 69
4.4. Testing and validating the formulation 72
4.4.1. Thin film charging 72
4.5. Conclusion 73

5. Conclusion 75

A. Amorphous samples preparation and characterization 79
A.1. Bulk properties of Li_xSi 79

Bibliography 93

Curriculum Vitae 95

List of Figures

1. Specific capacity of different active elements for anode material in lithium-ion batteries. Because of high energy storage capacity, Silicon and Tin has attracted researchers to make anode material based on them. [Obrovac et al.(2007)Obrovac, Christensen, Le, and Dahn] 1
2. SEM images of cracking and disintegration of a 300 nm amourphous Si electrode after one cycle at (a) 10 000 × magnification and (b)50 000 × magnification. [Pharr et al.(2013)Pharr, Suo, and Vlassak] 2
3. a,b) SEM images of crystalline Si particles before (a) and after (b) first lithiation. Cracks on the particle surface were observed after lithiation. c) Schematic showing the setup of the acoustic emission experiment: elastic waves produced by fracture events propagate through the electrode until reaching the acoustic emission sensor, which sends a signal to a computer for recording and processing. Acoustic emission signal, measured during galvanostatic cycling of a crystalline Si particle electrodes, are shown. Cumulative hits is the red line is an indicator of formed cracks. The voltage vs time is shown in green. The first lithiation shows the greatest number of fracture events. [Rhodes et al.(2010)Rhodes, Dudney, Lara-Curzio, and Daniel] . . . 3
4. Coulometric titration curve for the Li-Si system at 415 °C (dotted line) and galvanostatic charge/discharge of a Si powder electrode at room temperature (solid line). The high temperature data is taken from Wen et. al. [Wen and Huggins(1981)] . . . 4
5. Time-lapse images showing migration of the {112} ACI during lithiation. The ACI is ∼ 1 nm thick and did not change in thickness, but became smoother during progressive migration. [Liu et al.(2012)Liu, Liu, Kushima, Zhang, Zhu, Li, and Huang] 4
6. Illustration of mechanisms by which silicon is lithiated and delithiated. I to IV corresponds to lithiation of crystalline silicon discharged down to 0 mV. Red arrows denote discharge steps, while blue and green arrows denote charge steps. V to VIII correspond to the delithiation of fully lithiated silicon, and VIII to XI correspond to the relithiation of amorphous silicon to form fully lithiated silicon for subsequent cycles. The first proposed process seen on the second discharge is associated with the lithiation of the amorphous Si and forming small clusters. These clusters are broken in the second process to form isolated silicon anions. This makes the a-Si lithiation a two-phase process controlled by two competent diffusion and reaction instead of just simple diffusion [Key et al.(2011)Key, Morcrette, Tarascon, and Grey]. 6

7. (a) Cell potential vs. capacity curve corresponding to lithiation and delithiation of magnetron-sputtered amorphous Si thin-film electrode cycled at C/4 rate between 1.2 and 0.01 V vs. Li/Li$^+$, (b) the corresponding stress calculated from the substrate curvature data. The curves labeled X and Y correspond to the stresses calculated from the averaged horizontal and the vertical displacement of the spots on the sensor, respectively. The arrows in both figures indicate cycling direction. (c) Schematic illustration of the electrochemical-cell assembly; and the setup to measure substrate curvature. [Sethuraman et al.(2010b)Sethuraman, Chon, Shimshak, Srinivasan, and Guduru]. 7

8. Thickness effects during the second cycle of lithiation (a) nominal flow stress; (b) Li capacity. [Sethuraman et al.(2010b)Sethuraman, Chon, Shimshak, Srinivasan, and Guduru]. 8

9. Evolution of the biaxial stress in an a-Si thin film electrode during a lithiation and delithiation cycle: The orange line shows the in-situ measurement of the biaxial stress in the first lithiation cycle. The black lines with symbols (filled for lithiation, open for delithiation) show the evolution of the biaxial stress in an a-Si thin film electrode during a lithiation and delithiation cycle based on first-principles calculations. The error bars represent standard deviations obtained from several configurations at each Li concentration. The yield strength of lithiated Si at a given Li concentration, obtained by uniaxial tension simulations, is shown by triangles (the dashed line connecting the triangles is a guide to the eye).[Zhao et al.(2012b)Zhao, Tritsaris, Pharr, Wang, Okeke, Suo, Vlassak, and Kaxiras]. 9

10. The two types of inelastic deformation of Si during lithiation. Change of shape by flow and change of volume by insertion of Li. Flow is induced by the presence of deviatoric stresses. Insertion is driven by the chemical potential μ of Li in the reservoir and the mean stress σ_m. (b) A yield function $\Psi(s_{ij}, \xi)$ is sketched in the space of (s_{ij}, ξ); the condition $\Psi = 0$ defines the yield surface. (s_{ij}, ξ) represents the inelastic deformation driven by both the mechanical deviatoric stresses s_{ij} and the chemo mechanical load ξ.[Zhao et al.(2012b)Zhao, Tritsaris, Pharr, Wang, Okeke, Suo, Vlassak, and Kaxiras]. 11

1. Schematic of a hierarchy of Li$_x$Si alloys of varying composition, coded with color intensity, and excess energy $E^{xc}(x,\zeta)$ or structural disorder, shown with light bubbles inside each box. Starting from high concentration and taking infinitely fast delithiation steps ($\dot{x} \rightarrow \infty$) results in the highest possible excess energy. Long thermally activated relaxation steps relax the sample and lower the excess energy. The lower row shows the fully relaxed amorphous materials that is achieved by very slow delithiation ($\dot{x} \rightarrow 0$). In MS simulation we only reach states by removing atoms (fast delithiation steps), thus very slow delithiations path is a combination of fast delithiation and relaxation steps. 16

2. a) Excess energy per atom (e^{xc}) in Li$_x$Si during unequilibrated delithiation. b) Collapsed excess energy data with respect to x/x_∞ and the fitted curve. c) Stress-strain curve of LiSi alloy delithiated from different starting compositions, x_∞. d)Yield stress (σ_y) of Li$_x$Si alloys with different lithium content as a function of excess energy. Yield stress is a decreasing linear function of excess energy. 20

3. Excess volumetric strain in Li$_x$Si during delithiation. 21

4. Axial stress (σ) versus axial strain(ε) in LiSi nanowires that were previously discharged at different rates as indicated. All tests are done at a strain rate of $\dot{\varepsilon} = 10^{-3}/s$ and start immediately after discharging is complete. 28

5. Evolution of excess energy in LiSi nanowires after discharging is complete, for different rates of discharging under zero applied load. 29

6. Biaxial stress σ versus composition x in a confined Li$_x$Si thin film due to lithium discharge at different rates. 30

7. Accumulated excess energy versus composition x in a confined Li$_x$Si thin film due to lithium discharge at different rates. 31

8. Biaxial stress σ versus composition x in a Li$_x$Si thin film due to lithium charge/discharge cycles at $C/4$ rate. 33

9. Biaxial stress versus composition x in a Li$_x$Si thin film during one cycle with $\dot{x} = C/4$ and using elastic constants and ΔG varying with composition according to values obtained from MD simulations. 34

1. SEM images of residual indents for a lithiated electrode of $Li_{0.87}Si$, showing (a) no cracking, (b) radial cracking and (c) massive cracking subjected to different applied indentation loads. (d–f) SEM images of residual indents for a lithiated Si electrode of $Li_{1.56}Si$ showing no cracking subjected to the same loads (g) The indentation loads (symbols) applied to the lithiated electrodes with different Li contents. The blue solid curve represents the upper load limit above which massive cracking occurred and the black solid curve the lower limit below which no crack was induced. (h) Fracture toughness of radial cracks after indentation in thin film and fracture energy of lithiated Si as a function of Li concentration [Wang et al.(2015)Wang, Fan, Wang, Wang, Tao, Yang, Liu, Chew, Mao, Zhu, et al.]. 41

2. Schematic illustration of within fracture process zone during crack growth. The background plastic dissipation is not drawn in the figure. The length scale D indicates the characteristic distance between voids [Xia and Shih(1995a)]. 42

3. geometry of specimen and important details of simulation method. At each time step all atoms are moved in conformance with Eq 3.10. Atoms in the gray region are relaxed in NVT ensemble at $T = 1^\circ K$. Atoms in the white region are fixed to keep the loading. The thickness of boundary layers in our simulations is $b = 20$Å 44

4. Comparison between model of Eq. 3.6 and MD data for the uniaxial tension test with parameters $\sigma_0 = 0.9\sigma_f$ and $N = 0.1$ 45

5. a) Strain localization during cleavage-like crack propagation in high Li sample. Fracture happens in very low K_I values in the form of rupture as the result of stress concentration around formed clusters. 46

6. R-curve obtained using MD simulations for three different compositions. For each composition, eight samples have been simulated to address the randomness of the structure. 47

7. Snapshots of fracture process in different samples which shows the creation of voids, the growth and coalescence in front of crack tip. The scale is the same for all snapshots and is shown in the left upper picture. The spacing of void in front of the crack is reproducible over multiple samples and with crack growth. 49

8. Quantification of void nucleation and growth in $\mathrm{Li}_x\mathrm{Si}$ by coordination analysis. a) The logarithmic histogram of number of atoms with a specific strain normalized number of neighbours in a shell with cut-off radius $r_c = 6$Å b)A snapshot of specimen under equally uni-axial strain with $x = 0.5$ at $\varepsilon = 0.2$ 50

9. Stress-strain curves for generalized equi-biaxial plane strain expansion tests. Each line shows the average stress value for 8 randomly generated samples. 52

10. a-c)Fitting of GTN model stress-strain curve to the atomistic simulation of equi-biaxial expansion tests for three different as-quenched samples. For each composition the suitable f_0 in GTN model is shown in the figure. d) Ratio of maximum stress of equi-biaxial expansion tests to the yield stress for MD simulation and GTN model with different initial f_0 versus the composition. 54

11. Comparison of work of fracture for equi-biaxial generalized plane strain samples with initiation fracture energies for as-quenched material. 55

12. Stress-strain response of MD discharged amorphous $\mathrm{Li}_x\mathrm{Si}$ compared with model of Eq. 3.6. The parameters used in the model are: $N = 0.1$, $\sigma_0 = 0.9\sigma_f$ 55

13. R-curve obtained using MD simulations for three different discharged samples. For each composition 2 samples have been simulated and compared with non-discharged samples at the same composition of lithium. 57

14. a,c) Fitting of GTN model stress-strain curve to the atomistic simulation of equi-biaxial expansion tests for discharged samples with a)$x = 0.5$ and c)$x = 1.0$. b,d) Ratio of maximum stress of equi-biaxial expansion tests to the yield stress for MD simulation and GTN model with different initial f_0 versus the x_∞ for b)$x = 0.5$ and d)$x = 1.0$ in $\mathrm{Li}_x\mathrm{Si}$ 59

15. Comparison of work of fracture for equi-biaxial generalized plane strain samples with initiation fracture energies for as-quenched and discharged material. 60

1. Chemo-mechanics boundary value problem for displacement and concentration fields. The boundary is decomposed into Dirichlet and Neuman boundary types for each sub problem. 64

2. Shear stress (σ_{12}) versus shear strain(γ) in LiSi nanowires with different initial excess energies. All tests are done at a strain rate of $\dot{\varepsilon} = 10^{-3}/s$ and start immediately after discharging is complete. This test is performed to check the the developed finite element code. 71
3. a,b) FEM simulation of stress and excess energy development in a thin film during charging at point "A"shown in sub-figure (c). c) Geometry of simulated thin film and vertical expansion $\delta h/h$ of the thin film after fully charged. The lower boundary is fully clamped. 73

1. The Radial distribution functions of $\mathrm{Li}_x\mathrm{Si}$ amorphous alloys created by quenching. The variable x is the stoichiometric value in $\mathrm{Li}_x\mathrm{Si}$ alloy. Radial distribution function are obtained at 0 °K. All these simulations have been done using LAMMPS package [lam(1995)] 80
2. (a) Biaxial moduli of lithiated silicon. Experimental results are taken from Sethuraman et al. [Sethuraman et al.(2010a)Sethuraman, Chon, Shimshak, Van Winkle, and Guduru] and Ab-initio has been reported by Shenoy et al. [Shenoy et al.(2010)Shenoy, Johari, and Qi]. (b) Poisson's ratio calculated by three methods. Ab-inition results are again from the same reference. (c) Elastic moduli experimental and numerical values. Experimental values are obtained from Searle [Searle(1998)]. (d) Shear modulus experimental and calculated values. Two values has been reported experimentally for amorphous silicon. 81

List of Tables

1. Parameters of the model which are used in the simulations 27

1. Calculated range of fracture energies corresponding to a range of Li concentration using in-situ measurement methods by Pharr. et. al. [Pharr et al.(2013)Pharr, Suo, and Vlassak]. 39
2. Plane strain plastic zone size for Li_xSi with different compositions. 45
3. K_{IC} and K_I values for fracture tests in Li_xSi with different as-quenched compositions. 48
4. Measured values of the spacing of the voids, D, and calculated scaling factor α in MD simulation for different as-quenched samples. 51
5. K_{IC} and K_I values for fracture tests in Li_xSi with different compositions for discharged and as-quenched samples. 56
6. Measured values of D parameter in MD simulation along with J_{IC} and α for different compositions after discharging. 58
7. Predicted experimental fracture energy of Li_xSi based on MD simulations. 60

1 Background and motivation

1.1 Introduction

Lithium-ion batteries are characterized by high specific energy capacity, high operating voltage, low self-discharge and long life[Scrosati and Garche(2010)]. A lithium-ion battery contains an electrolyte and two electrodes. During charging of the battery, lithium ions are extracted from cathode (positive electrode), migrate through the electrolyte, and are then inserted into the anode (negative electrode). Meanwhile, electrons flow from the anode to the cathode through an external circuit.

For higher capacity Li-ion batteries, silicon (Si) has the highest known theoretical specific charge capacity $\left(\sim 4000\,\frac{mAh}{g}\right)$ [Kang et al.(2010)Kang, Lee, Han, Kim, Lee, Lee, Kang, and Jo] which is around ten times higher than common carbon based anode materials[Obrovac et al.(2007)Obrovac, Christensen, Le, and Dahn]. Due to the big difference in capacity between silicon and other materials, tremendous attention in the scientific literature is being given to the design of anode materials based on Si. Figure 1 graphically compares the specific capacities of various active elements in the lithium-ion electrochemical cell.

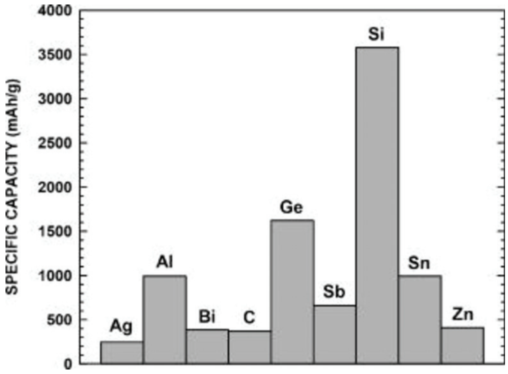

Figure 1 – Specific capacity of different active elements for anode material in lithium-ion batteries. Because of high energy storage capacity, Silicon and Tin has attracted researchers to make anode material based on them. [Obrovac et al.(2007)Obrovac, Christensen, Le, and Dahn]

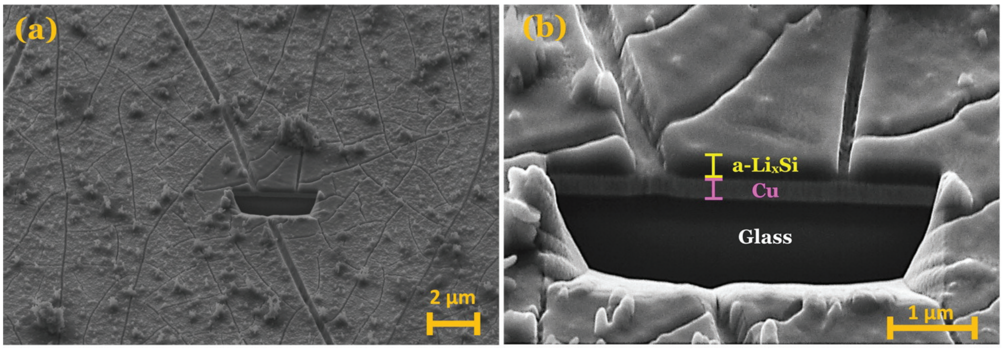

Figure 2 – SEM images of cracking and disintegration of a 300 nm amourphous Si electrode after one cycle at (a) 10 000 × magnification and (b)50 000 × magnification. [Pharr et al.(2013)Pharr, Suo, and Vlassak]

In spite of the promising electrochemical properties of Si-based lithium alloys, they cannot be easily used in lithium cells. The main issue is that there is a large volume expansion–contraction, of up to 400% after fully charged [Cui et al.(2009)Cui, Ruffo, Chan, Peng, and Cui, Chan et al.(2008)Chan, Peng, Liu, McIlwrath, Zhang, Huggins, and Cui], which occurs during the charge/discharge processes. These volume changes induce mechanical stresses, resulting in disintegration of the electrode with consequent failure after a modest number of charge/discharge cycles [Scrosati and Garche(2010), Winter and Besenhard(1999)]. Figure 2 shows the failure process in Si-Li film which consists of crack formation, and disintegration of anode material. Lithiation-induced mechanical failure has been one of the major bottlenecks in developing batteries of high energy density for large scale commercialization of Si-based anode Li-ion batteries.

Figure 3 shows another experiment on crack formation in Li-Si systems [Rhodes et al.(2010)Rhodes, Dudney, Lara-Curzio, and Daniel]. It depicts SEM images of crystalline Si particles before and after the first lithiation. Initiation of cracks in crystalline silicon is observed on particle surfaces. The formation of surface cracks on the surface of particles is also measured using acoustic emission. These initial cracks cause pulverization in the immediate next cycles of lithiation.

In the following, first, a review of important aspects of utilizing silicon as anode material for Li-ion batteries will be presented. Specifically, we will discuss the phases existent chemical phases of Li_xSi which need to be analyzed in any modeling effort. This will be followed by a review of important endeavors on the modeling of lithiated silicon.

1.2 Lithiation of Si in electrochemical processes

Silicon has been utilized as active anode material in different forms such as pure Si micro and nano-scale powder anodes [Weydanz et al.(1999)Weydanz, Wohlfahrt-Mehrens, and Huggins, Lee and Lee(2002), Hwang et al.(2001)Hwang, Lee, Jang, Lee, Lee, Baik, and Lee],

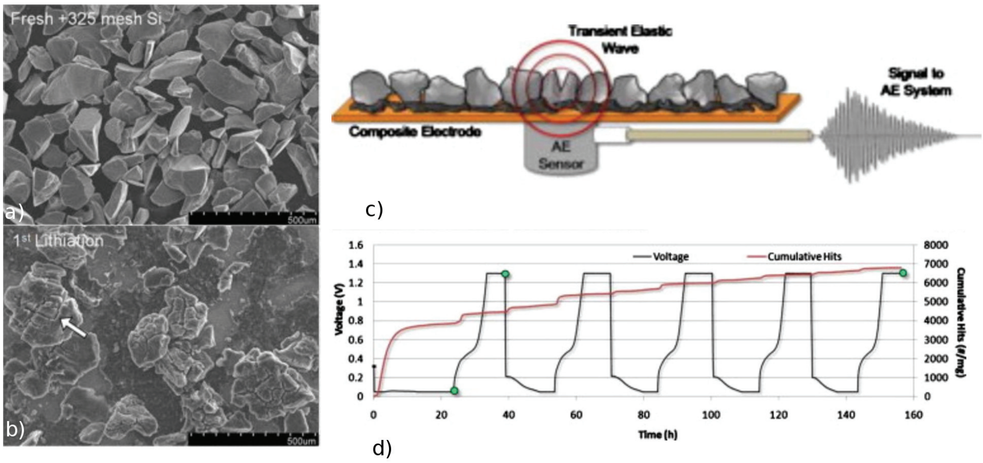

Figure 3 – a,b) SEM images of crystalline Si particles before (a) and after (b) first lithiation. Cracks on the particle surface were observed after lithiation. c) Schematic showing the setup of the acoustic emission experiment: elastic waves produced by fracture events propagate through the electrode until reaching the acoustic emission sensor, which sends a signal to a computer for recording and processing. Acoustic emission signal, measured during galvanostatic cycling of a crystalline Si particle electrodes, are shown. Cumulative hits is the red line is an indicator of formed cracks. The voltage vs time is shown in green. The first lithiation shows the greatest number of fracture events. [Rhodes et al.(2010)Rhodes, Dudney, Lara-Curzio, and Daniel]

Si base composite materials [Yang et al.(2003)Yang, Wang, Wang, Liu, Xie, and Wen], Si nano structures [Chan et al.(2008)Chan, Peng, Liu, McIlwrath, Zhang, Huggins, and Cui] and thin films [Graetz et al.(2003)Graetz, Ahn, Yazami, and Fultz].

It is common to start with crystalline Si as the active anode material. Upon few cycles of charging and discharging crystalline silicon undergoes significant irreversible capacity loss [Ji et al.(2011)Ji, Ma, and Lee, Chan et al.(2008)Chan, Peng, Liu, McIlwrath, Zhang, Huggins, and Cui], substantial particle fracture [Rhodes et al.(2010)Rhodes, Dudney, Lara-Curzio, and Daniel] and phase changes [Limthongkul et al.(2003)Limthongkul, Jang, Dudney, and Chiang] from crystalline to amorphous phase or vice versa. To understand these processes, it is necessary to study the structural changes and volume expansion during lithiation of crystalline and amorphous Si structures.

Crystalline Si is electrochemically lithiated via a two-phase mechanism in which the Si forms lithiated amorphous Si. During lithiation, the two phases are separated by a sharp reaction front of nanometer scale thickness. Fundamentally, because of the large activation energy required to break up the crystalline Si matrix, a high concentration of Li atoms near the reaction front is required to weaken these bonds. This leads to the observed two-phase behavior [Chon et al.(2011)Chon, Sethuraman, McCormick, Srinivasan, and Guduru, Key et al.(2011)Key, Morcrette, Tarascon, and Grey, Li et al.(2000)Li, Huang, Chen, Zhou, Zhang, Yu, Jun Mo, and Pei, Liu et al.(2012)Liu, Liu, Kushima, Zhang, Zhu, Li, and Huang]. The formation of highly lithiated Si at the reaction front causes most of the volume expansion to occur right at the front, which leads to enormous gradients in transformation strain and initiating large

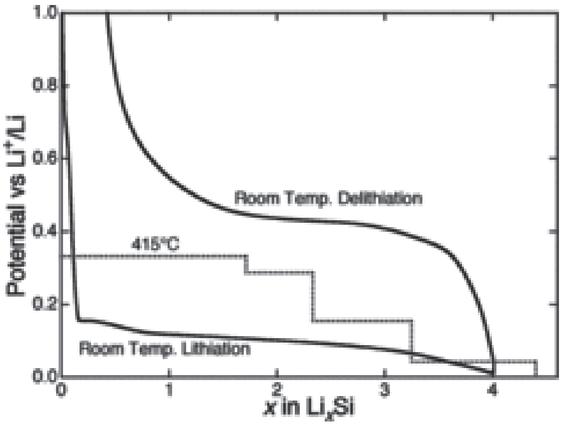

Figure 4 – Coulometric titration curve for the Li-Si system at 415 °C (dotted line) and galvanostatic charge/discharge of a Si powder electrode at room temperature (solid line). The high temperature data is taken from Wen et. al. [Wen and Huggins(1981)]

percentage of cracks in this stage (See Fig. 3).

After the first lithiation, an amorphous phase will be formed. Evidence for this phenomenon can be traced back to simple titration experiments. The equilibrium coulometric titration curve shows four intermediate phases in the Li-Si system at 415°C. The nominal compositions for these phases are $Li_{12}Si_7$, Li_7Si_3, $Li_{13}Si_4$, and $Li_{22}Si_5$, respectively. The compositional variations of the chemical diffusion coefficients within the various intermediate phases are similar to each other. The sequential formation of these compounds results in a stepped galvanostatic voltage profile during high-temperature electrochemical experiments [Wen and Huggins(1981)]. At room temperature, however, the galvanostatic (constant electrical current) voltage profile of typical crystalline Si electrodes during lithiation shows first a big drop continued by a relatively flat voltage plateau around $0.1V$ that suggests a two-phase field over most of the lithiation process [Limthongkul et al.(2003)Limthongkul, Jang, Dudney, and Chiang]. There is also a large hysteresis between lithiation and delithiation. Figure 4 shows

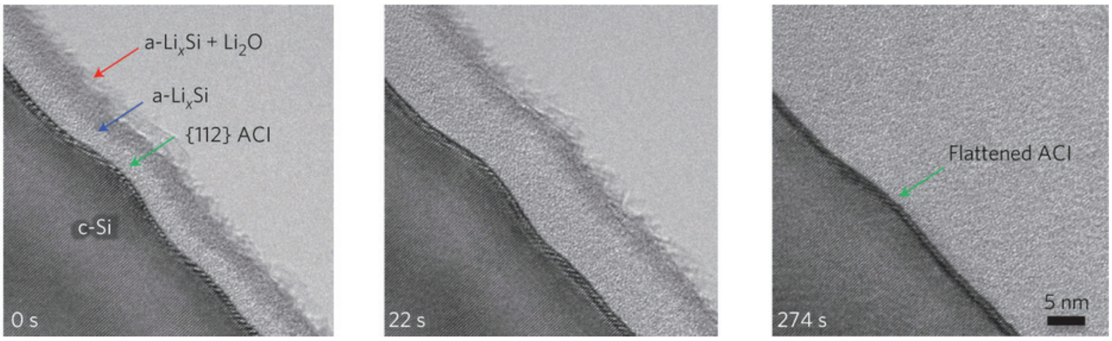

Figure 5 – Time-lapse images showing migration of the {112} ACI during lithiation. The ACI is ~ $1\,nm$ thick and did not change in thickness, but became smoother during progressive migration. [Liu et al.(2012)Liu, Liu, Kushima, Zhang, Zhu, Li, and Huang]

the above-mentioned phenomena and compares them. Recently, the two-phase structure of the amorphous/crystalline interface in Li-Si system was imaged with scanning electron microscopy and high-resolution transmission electron microscopy [Chon et al.(2011)Chon, Sethuraman, McCormick, Srinivasan, and Guduru, Liu et al.(2012)Liu, Liu, Kushima, Zhang, Zhu, Li, and Huang]. Figure 5 shows amorphous crystalline interface (ACI) movement.

The two important and interrelated aspects of the first cycle lithiation of crystalline Si are anisotropic lithiation and volume expansion and reaction front dominated nature of lithiation process. Several studies [Lee et al.(2011)Lee, McDowell, Choi, and Cui, Goldman et al.(2011)Goldman, Long, Gewirth, and Nuzzo, Liu et al.(2011)Liu, Zheng, Zhong, Huang, Karki, Zhang, Liu, Kushima, Liang, Wang, et al.]investigated the anisotropic nature of volume changes in crystalline Si. These experiments have established that anisotropic lithiation and expansion is primarily a result of differing interfacial mobilities of different crystallographic planes. Diffusion of Li in crystalline Si does not play a role since the symmetry elements of a cubic crystal mathematically result in isotropic diffusivity. Furthermore, by assigning different reaction front velocities to different crystallographic surfaces in finite element simulations of volume expansion and plastic deformation during the lithiation of Si, a few studies have reproduced the experimentally observed lithiated crystalline silicon [Zhao et al.(2012a)Zhao, Pharr, Wan, Wang, Kaxiras, Vlassak, and Suo, Yang et al.(2012)Yang, Huang, Huang, Fan, Liang, Liu, Chen, Huang, Li, Zhu, and Zhang].

The reaction of amorphous Si with Li is different from the crystalline case. Key et al. [Key et al.(2011)Key, Morcrette, Tarascon, and Grey]applied a combination of local structure probes, ex-situ nuclear magnetic resonance (NMR) studies, and pair distribution function (PDF) analysis of X-ray data to analyze the changes in short-range order which occurs during the initial charge/discharge cycles. The sloping voltage profile during lithiation of amorphous Si [Beaulieu et al.(2003)Beaulieu, Hatchard, Bonakdarpour, Fleischauer, and Dahn] has led most researchers to conclude that lithiation is a single-phase reaction that does not feature a reaction front. However, this study as well as recent in-situ TEM experiments [Wang et al.(2013)Wang, He, Fan, Liu, Xia, Liu, Harris, Li, Huang, Mao, and Zhu] have revealed more complex two-phase lithiation behavior. Although still there is not yet a commonly accepted mechanism, Wang et al., from their in-situ experiment, reported that the lithiation occurs by the movement of a sharp phase boundary between the amorphous Si and an amorphous Li_xSi (a-Li_xSi , $x \sim 2.5$). Such amorphous-amorphous interface exists until the remaining a-Si is consumed. Then a second step of lithiation starts without a visible interface which results in the final product of a-Li_xSi ($x \sim 3.75$). The distinction between single-phase and two-phase lithiation behavior is important since the two different reaction mechanisms theoretically cause different stress evolution and fracture mechanisms. Figure 6 shows an abstract view of c-Si and a-Si lithiation proposed in ref. [Key et al.(2011)Key, Morcrette, Tarascon, and Grey].

According to several studies, highly lithiated amorphous silicon suddenly crystallizes to form the $Li_{15}Si_4$ at room temperature. Chevrier and Dahn [Chevrier and Dahn(2009)] have noted that the $Li_{15}Si_4$ phase is the only crystalline Li-Si phase in which all the Si atoms have equiv-

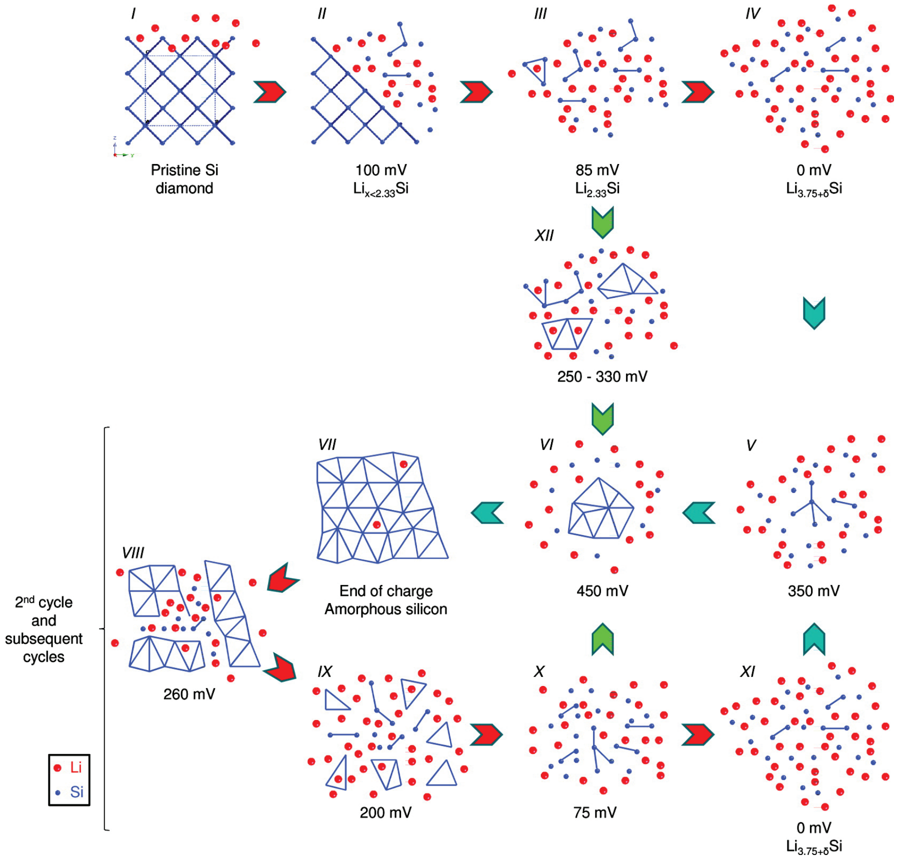

Figure 6 – Illustration of mechanisms by which silicon is lithiated and delithiated. I to IV corresponds to lithiation of crystalline silicon discharged down to 0 mV. Red arrows denote discharge steps, while blue and green arrows denote charge steps. V to VIII correspond to the delithiation of fully lithiated silicon, and VIII to XI correspond to the relithiation of amorphous silicon to form fully lithiated silicon for subsequent cycles. The first proposed process seen on the second discharge is associated with the lithiation of the amorphous Si and forming small clusters. These clusters are broken in the second process to form isolated silicon anions. This makes the a-Si lithiation a two-phase process controlled by two competent diffusion and reaction instead of just simple diffusion [Key et al.(2011)Key, Morcrette, Tarascon, and Grey].

alent crystallographic sites; each Si atom has 12 Li neighbors. If Si atoms are well dispersed and surrounded by Li atoms, the similarities in the local atomic environments in the lithiated amorphous phase and the crystalline $Li_{15}Si_4$ phase might lead to kinetically-favored crystallization of the metastable phase instead of the formation of a thermodynamically stable phase at stoichiometry $x > 4$; i.e. $Li_{22}Si_5$ [Key et al.(2009)Key, Bhattacharyya, Morcrette, Seznec, Tarascon, and Grey, Chevrier and Dahn(2009)]. The crystalline $Li_{15}Si_4$phase can only accommodate a small excess of Li. This excess lithium phase is extremely reactive in the electrolyte and the Li–Si cell self discharges, leading to the loss of Li from this phase[Key et al.(2009)Key, Bhattacharyya, Morcrette, Seznec, Tarascon, and Grey]. Upon delithiation of the crystalline $Li_{15}Si_4$ phase, the material transforms back to amorphous Si. This can be an important mechanism of capacity fading especially on the solid electrolyte interface for highly

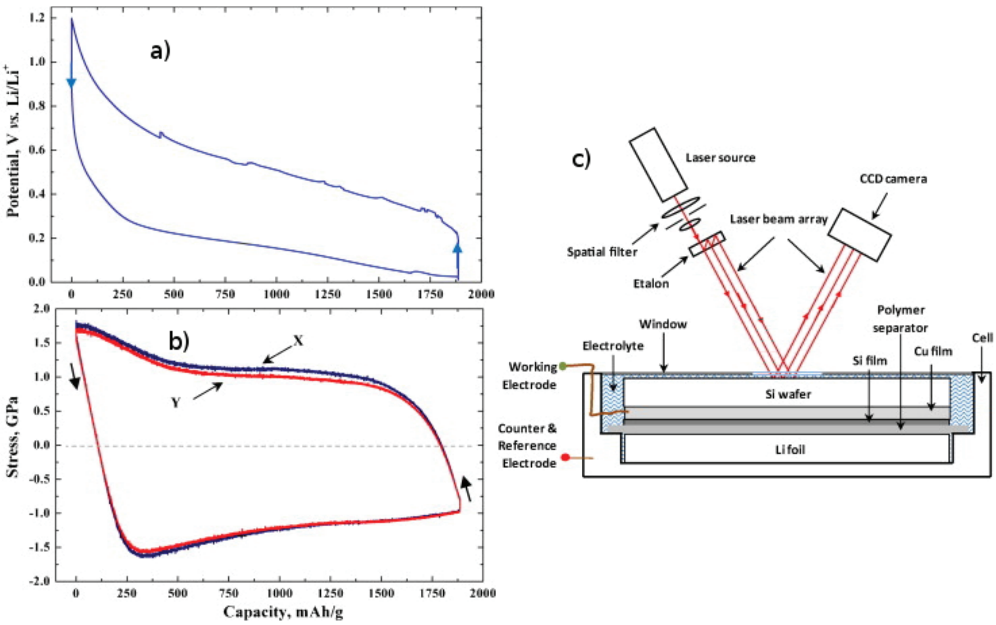

Figure 7 – (a) Cell potential vs. capacity curve corresponding to lithiation and delithiation of magnetron-sputtered amorphous Si thin-film electrode cycled at C/4 rate between 1.2 and 0.01 V vs. Li/Li$^+$, (b) the corresponding stress calculated from the substrate curvature data. The curves labeled X and Y correspond to the stresses calculated from the averaged horizontal and the vertical displacement of the spots on the sensor, respectively. The arrows in both figures indicate cycling direction. (c) Schematic illustration of the electrochemical-cell assembly; and the setup to measure substrate curvature. [Sethuraman et al.(2010b)Sethuraman, Chon, Shimshak, Srinivasan, and Guduru].

lithiated silicon.

1.2.1 Stress growth and fracture during electrochemical process

Since the stress causes fracture and failure, it is important to understand the mechanical stresses that develop due to volume changes in lithiation process. Lithiation induced stresses arise from inhomogeneous volume changes resulting from Li concentration gradients within Si. Some work has been done to experimentally study the stress evolution in silicon using wafer-curvature techniques and monitor the stress in a thin Si film during lithiation. An early study was performed by Lee et al. [Lee et al.(2001)Lee, Lee, Chung, Lee, Lee, and Baik], though they reported just beam deflection without relating it to stress.

More recently, Sethuraman et al. performed similar measurements with more comprehensive analysis of the data [Sethuraman et al.(2010b)Sethuraman, Chon, Shimshak, Srinivasan, and Guduru]. Figure 7 depicts the stress-capacity and voltage-capacity curves in few subsequent galvanostatic lithiation/delithiation cycles. In this study silicon thin films were prepared by RF-magnetron sputtering and an amorphous thin film from the beginning has been created. Thus, amorphization due to initial lithiation does not occur, and the data corresponding to first cycle is similar to those obtained in subsequent cycles. Upon lithiation, the substrate

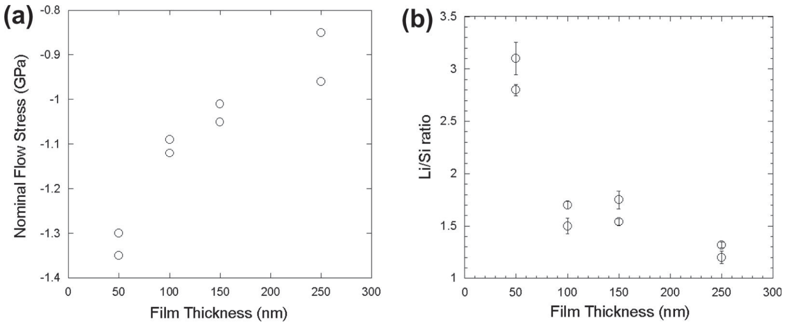

Figure 8 – Thickness effects during the second cycle of lithiation (a) nominal flow stress; (b) Li capacity. [Sethuraman et al.(2010b)Sethuraman, Chon, Shimshak, Srinivasan, and Guduru].

prevents the in-plane expansion of the film. Thus compressive stress in the film builds up, and it increases linearly with time (or capacity). The characteristic time for diffusion through the film is measured and reported to be only a fraction of a second which is fast enough for the experiments conducted with a rate of $C/4$. Thus they assumed that the Li concentration, and hence the in-plane stress are uniform through the film thickness. Moreover, assuming that the strain induced by Li in Si is proportional to its concentration, then the linear increase in the compressive stress indicates an elastic response. At a compressive stress of about 1.7 GPa, the film reaches the elastic limit, and begins to flow. The flow stress is seen to decrease with lithiation, reaching a value of about 1 GPa, at highest reachable lithium concentration. Hence, the flow stress of lithiated Si decreases as the Li concentration increases during lithiation [Sethuraman et al.(2010b)Sethuraman, Chon, Shimshak, Srinivasan, and Guduru].

In the delithiation part, the unloading is initially elastic; the stress reverses elastically until it becomes about 1 GPa in tension, where the film begins to flow in tension to accommodate the reduction in volume. The flow stress increases to about 1.75 GPa when the upper potential limit is reached. Note that the stress response is similar in compression and tension, thus at any state of charge, the flow stress in compression and tension are approximately the same. The film undergoes repeated compressive and tensile-plastic flow during successive lithiation–delithiation processes, respectively. The measurements shown in Fig. 7 correspond to the third charge/discharge cycle; subsequent cycles show very similar behavior. Since the state of stress during lithiation and delithiation is different even in an identical state of charge, all material properties that depend on stress will be different during lithiation and delithiation.

In a related work Soni et al. [Soni et al.(2011)Soni, Sheldon, Xiao, and Tokranov] used the same experimental setting and showed that the nominal flow stress is greater for thinner films(See Fig. 8). These observations suggest that the Li chemical diffusivity is slower than that reported in the literature and the constant lithium concentration in the film might not be a valid assumption in thin experiments.

Zhao et al. [Zhao et al.(2012b)Zhao, Tritsaris, Pharr, Wang, Okeke, Suo, Vlassak, and Kaxiras] utilized first principle calculations and the wafer-curvature technique to demonstrate that the flow stress of lithiated Si at a given Li concentration, obtained by uniaxial tension simulations, are much higher than those obtained in the electrochemical cell (9). In other words, the stress developed in the thin film depends on the electrochemical process in the cell. We will further analyze this result in Chapter 2 and build a mechanistic model to describe the effect of structural change during charging/discharging on the plastic strength of Li_xSi . Moreover, the experimental yield stress reported is $2\,GPa$ for $Li_{0.25}Si$ (elastic limit) which is higher than that the value in other experimental studies. They noted that this may be due to neglecting the effect of the refractive index difference between the electrolyte and air in the previous studies [Zhao et al.(2012b)Zhao, Tritsaris, Pharr, Wang, Okeke, Suo, Vlassak, and Kaxiras].

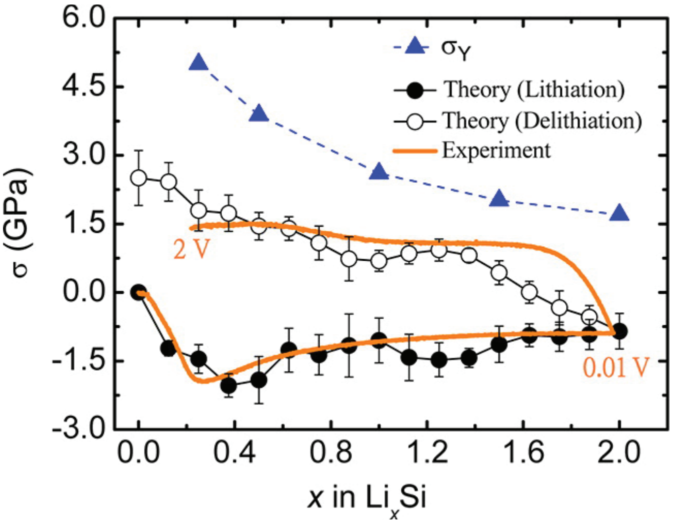

Figure 9 – Evolution of the biaxial stress in an a-Si thin film electrode during a lithiation and delithiation cycle: The orange line shows the in-situ measurement of the biaxial stress in the first lithiation cycle. The black lines with symbols (filled for lithiation, open for delithiation) show the evolution of the biaxial stress in an a-Si thin film electrode during a lithiation and delithiation cycle based on first-principles calculations. The error bars represent standard deviations obtained from several configurations at each Li concentration. The yield strength of lithiated Si at a given Li concentration, obtained by uniaxial tension simulations, is shown by triangles (the dashed line connecting the triangles is a guide to the eye).[Zhao et al.(2012b)Zhao, Tritsaris, Pharr, Wang, Okeke, Suo, Vlassak, and Kaxiras].

1.2.2 Modeling of stress evolution and fracture in Li_xSi

The ability to model damage evolution in battery materials would aid the design process significantly. This has motivated some recent models of stress evolution, diffusion and fracture in Li-Si alloys as well as other electrode materials. Stress evolution in a single particle by assuming small mechanical deformation characterized by linear isotropic elasticity and a dilute solution for diffusion within the solid state has been analyzed analytically by Verbrugge and Cheng. They also used the same analytical method to analyze crack propagation and fatigue as well as different electrochemical conditions [Verbrugge and Cheng(2008), Verbrugge and Cheng(2009), Cheng and Verbrugge(2010), Cheng and Verbrugge(2009)].

Using similar set of assumptions, Zhang et al. investigated intercalation induced stresses in Li cells. They specifically worked on $LiMn_2O_4$ system and solved spherical one-dimensional and fully three-dimensional problems to quantify the results [Zhang et al.(2007)Zhang, Shyy, and Sastry]. In a subsequent publication, Hun et al. used atomic force microscopy (AFM) to reconstruct particle real geometries and simulated the $LiMn_2O_4$ system under galvanostatic (constant current) and potentiodynamic control [Hun et al.(2011)Hun, Chung, Park, Woo, Zhang, and Marie]. The next step was to incorporate realistic geometries with measured diffusion coefficients [Chung et al.(2011)Chung, Seo, Zhang, and Sastry] and also phase transitions [Park et al.(2011)Park, Lu, and Sastry] for the above mentioned system.

Few research efforts on modeling of the collective behavior of an entire electrochemical cell or half cell also exist. Garcia et al. [Garcia et al.(2005)Garcia, Chiang, Carter, Limthongkul, and Bishop] developed a method that uses microscopic information and constitutive material properties to calculate the response of rechargeable batteries. The method is implemented to be applied to arbitrary two-dimensional microstructures with crystallographic anisotropy and they applied it to improve electrode utilization, power density, and reliability of the $Li_yC_6/Li_xMn_2O_4$ battery systems by focusing on the positive electrode. Christensen and Newman [Christensen and Newman(2006)] also derived a model to determined maximum stress in the particle as a function of dimensionless current, which includes the charge rate, particle size, and diffusion coefficient. Also, a finite element model of a three-dimensional, porous cathode was constructed and analyzed by Wang and Sastry [Wang and Sastry(2007)]. Other research endeavors in this line include work done by Zhang et al. [Zhang et al.(2007)Zhang, Shyy, and Sastry] and Golmon et al. [Golmon et al.(2009)Golmon, Maute, and Dunn]. Notably, Bower et al. in a recent work developed a thermodynamically based model of the collective behavior of an entire electrochemical half cell, which extended previous analyses by considering the effects of finite strains and plastic flow in the electrodes. They also explored in detail the role of stress in the electrochemical reactions at the electrode–electrolyte interfaces [Bower et al.(2011)Bower, Guduru, and Sethuraman].

A full analysis of a complex battery electrode microstructure can only be accomplished by solving the coupled field equations of mechanical equilibrium and Li diffusion, accounting for the effects of stress on diffusion. Because of the large volume changes that occur during lithiation, the field equations may be nonlinear even if the material deforms reversibly. Some electrode materials also deform plastically. Bower and Guduru recently described a simple and robust finite element implementation that meets these requirements [Bower and Guduru(2012a)]. They used viscoplastic models to describe plasticity and cohesive zone models for fracture modeling. This model still does not consider the effect oc charging and discharging on mechanical properties as shown in Fig. 9. The first research which tries to relate mechanical properties of Li_xSi to the charging/discharging history is presented in a series of paper by Suo et al. [Zhao et al.(2011b)Zhao, Wang, Gregoire, Pharr, Suo, Vlassak, and Kaxiras, Zhao et al.(2011a)Zhao, Pharr, Cai, Vlassak, and Suo, Zhao et al.(2012a)Zhao, Pharr, Wan, Wang, Kaxiras, Vlassak, and Suo, Brassart and Suo(2012), Zhao et al.(2012b)Zhao, Tritsaris, Pharr, Wang, Okeke, Suo, Vlassak, and Kaxiras]. They developed the concept of reactive flow in solids

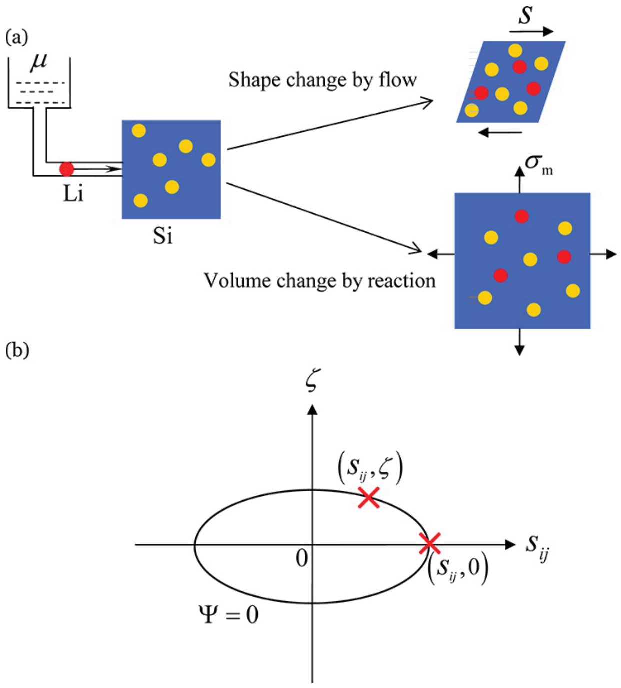

Figure 10 – The two types of inelastic deformation of Si during lithiation. Change of shape by flow and change of volume by insertion of Li. Flow is induced by the presence of deviatoric stresses. Insertion is driven by the chemical potential μ of Li in the reservoir and the mean stress σ_m. (b) A yield function $\Psi(s_{ij},\xi)$ is sketched in the space of (s_{ij},ξ); the condition $\Psi = 0$ defines the yield surface. (s_{ij},ξ) represents the inelastic deformation driven by both the mechanical deviatoric stresses s_{ij} and the chemo mechanical load ξ.[Zhao et al.(2012b)Zhao, Tritsaris, Pharr, Wang, Okeke, Suo, Vlassak, and Kaxiras].

for Li-ion battery electrodes. In their view, an electrode in a lithium-ion battery may undergo inelastic processes of two types: flow and reaction. Flow changes the shape of the electrode, preserves its composition and volume, and is driven by the deviatoric stress, a process similar to the plastic flow of metal. By contrast, reaction changes the composition and volume of the electrode, and is driven by a combination of the mean stress σ_m and the chemical potential of lithium in the environment $\mu - \mu_0$ with force $\xi = \sigma_m + \frac{\mu-\mu_0}{\Omega}$ (Ω is the volume of adding an atom). Within this theory, the driving force for reaction, i.e. the mean stress and the chemical potential can stimulate flow in an electrode too brittle to flow under a mechanical load alone. Figure 10 schematically describes this theory. As a result of the theory, the yield surface is assumed to be dependent on ξ as well as deviatoric stresses s_{ij}. Although this theory considers the effect of charging/discharging on the mechanical behavior of lithiated silicon inside the electrochemical cell, it is a purely phenomenological theory and all its parameters should be fitted to experiment.

Recently, Levitas and Attariani [Levitas and Attariani(2013)] developed another phenomenological model of Li-Si materials. This model suggested a stress relaxation mechanism which is due to anisotropic (tensorial) compositional straining that occurs during insertion-extraction at any deviatoric stresses. As a result, chemical potential has an additional contribution due to deviatoric stresses, which leads to increases in the driving force both for insertion and extraction. Thus this theory is also incorporating the effect of chemical potential in the flow stress in a phenomenological fashion. Lastly, among efforts to model different aspects of Si lithiation, and specifically modeling the effect of charging/discharging on the mechanical behavior of lithiated silicon, Cui et al. [Cui et al.(2012b)Cui, Gao, and Qu] reported a new stress-dependent chemical potential for solid state diffusion under driving forces such as mechanical stresses. They introduced new stress-dependent (total stress) chemical potential accounts for nonlinear, inelastic, and finite deformation. This is similar to the Levitas and Attariani [Levitas and Attariani(2013)] approach in the sense that they are claiming inter-relation between chemical potential and deviatoric part of the stress.

1.3 Outline of the thesis

The goal of this thesis is to acquire a better understanding of mechanical behavior of lithiated silicon in Li-ion batteries. In Chapter 2, we are going to propose a mechanistically, physics-based model for plasticity of lithiated silicon which considers the effect of charging/discharging on the flow stress. There are no purely phenomenological aspects in our model, and we have used MD simulation to validate the basic premises of the model. In chapter 4 we have developed a finite element method which used the developed constitutive relation in Chapter 2 to simulate complicated geometries numerically. Chapter 3 is devoted to better understanding of fracture in lithiated silicon. We have shown that the ductile fracture models are good candidates to describe complicated trends in the fracture of lithiated silicon. We used MD simulation to model fracture and analyzed the nano-mechanisms of fracture in lithiated silicon in detail.

2 Effect of charging/discharging on the plastic flow of Li-Si alloys

Plastic flow is an important mechanism for relaxing stresses that develop due to swelling/shrinkage during charging/discharging of battery materials. Amorphous high-storage-capacity Li-Si has lower flow stresses than crystalline materials but there is evidence that the plastic flow stress depends on the conditions of charging and discharging, indicating important non-equilibrium aspects to the flow behavior. Here, a mechanistically-based constitutive model for rate-dependent plastic flow in amorphous materials, such as $\mathrm{Li}_x\mathrm{Si}$ alloys, during charging and discharging is developed based on two physical concepts: (i) excess energy is stored in the material during electrochemical charging and discharging due to the inability of the amorphous material to fully relax during the charging/discharging process and (ii) this excess energy reduces the barriers for plastic flow processes and thus reduces the applied stresses necessary to cause plastic flow. The plastic flow stress is thus a competition between the time scales of charging/discharging and the time scales of glassy relaxation. The two concepts, as well as other aspects of the model, are validated using molecular simulations on a model Li-Si system. The model is applied to examine the plastic flow behavior of typical specimen geometries due to combined charging/discharging and stress history, and the results generally rationalize experimental observations.

2.1 Introduction

Lithium-ion batteries are characterized by high specific energy capacity, high operating voltage, low self-discharge energy storage, and long life [Scrosati and Garche(2010)]. However, the expansion/contraction during Li injection/extraction into anodes and cathodes introduces stresses that can drive early failure of the system. The design of materials and structures to optimize capacity and lifetime is thus a major goal in the field. Silicon has the highest known theoretical specific charge capacity for lithium-ion battery anodes [Kang et al.(2010)Kang, Lee, Han, Kim, Lee, Lee, Kang, and Jo] and has been studied in different forms such as micro and nano-scale powders [Weydanz et al.(1999)Weydanz, Wohlfahrt-Mehrens, and Huggins, Hwang et al.(2001)Hwang, Lee, Jang, Lee, Lee, Baik, and Lee], silicon-based composite materials [Yang et al.(2003)Yang, Wang, Wang, Liu, Xie, and Wen], silicon nanostructures

[Chan et al.(2008)Chan, Peng, Liu, McIlwrath, Zhang, Huggins, and Cui] and thin films [Graetz et al.(2003)Graetz, Ahn, Yazami, and Fultz]. In spite of its promising electrochemical properties, the mechanical stresses arising due to the large volume expansion during charging results in disintegration of the electrode and failure after a modest number of electrical loading cycles [Scrosati and Garche(2010)]. Crystalline silicon undergoes a phase change from crystalline to amorphous [Limthongkul et al.(2003)Limthongkul, Jang, Dudney, and Chiang, Chon et al.(2011)Chon, Sethuraman, McCormick, Srinivasan, and Guduru, Liu et al.(2012)Liu, Liu, Kushima, Zhang, Zhu, Li, and Huang] upon first lithiation, so that stress development and failure process in subsequent charging/discharging cycles are occurring in amorphous Li_xSi alloys, and lead to irreversible capacity loss and fracture [Chan et al.(2008)Chan, Peng, Liu, McIlwrath, Zhang, Huggins, and Cui, Ji et al.(2011)Ji, Ma, and Lee]. Germanium has been also tested as an anode material for lithium ion batteries, due to its high lithiation capacity and diffusion coefficient, and shows the same behavior of amorphization and high plastic strains upon lithiation [Lim et al.(2014)Lim, Liu, Cui, and Toney, Liang et al.(2013)Liang, Yang, Fan, Liu, Liu, Huang, Zhu, and Zhang]. A physically-based understanding of the mechanical behavior, and particularly plastic flow, of amorphous battery materials, and in particular the Li_xSi system, is essential for guiding design of damage-resistant microstructures in which physical length scales, Li diffusion rates, elastic and plastic flow behavior, and interface failure, all combine to control the anode lifetime under specific charging and discharging conditions.

Zhao et al. [Zhao et al.(2012b)Zhao, Tritsaris, Pharr, Wang, Okeke, Suo, Vlassak, and Kaxiras], using first principle calculations on small samples, demonstrated that the yield stresses in amorphous Li_xSi samples differ between samples measured in the as-prepared state and after removing Li atoms, respectively, at the same Li concentration. The flow stresses estimated during charging/discharging agreed reasonably with experimental measurements. These results suggest some relationship between the process of Li injection into the alloy and the yield stress of the material. Brassart and Suo [Brassart and Suo(2012)] thus developed a “reactive flow” concept where the plastic yield surface depends on both stress and chemical potential. Other models also relate the flow stress to the chemical potential for amorphous silicon anodes [Levitas and Attariani(2013), Cui et al.(2012b)Cui, Gao, and Qu]. These models have a well-structured mathematical framework but their physical bases remain unclear while the proposed yield surfaces in stress/chemical-potential space remain phenomenological and also independent of charging rate.

In this paper, we develop a mechanistically-based rate-dependent constitutive model for amorphous battery materials that accounts for the effects of charging/discharging on the rate-dependent plastic flow. The basic concept of the model is that during charging or discharging, i.e. when Li atoms are added or removed from a unit volume of material, the material is unable to instantaneously relax to a fully-relaxed state at the new Li concentration. Rather, there is excess energy stored in the material that is only relaxed by thermally-activated structural relaxation processes in the amorphous material. Most importantly, this excess energy is available to facilitate the stress-driven thermal activation processes that cause plastic flow, thus lowering the applied stresses needed to drive plastic flow. The total excess energy at any time reflects an on-going competition between decreases due to energy relaxation processes and increases due to charging/discharging. The flow stress then depends on the current composition, the temperature, and the current excess energy, which has evolved during the charging/discharging/loading history of the material. We use Li$_x$Si as the test material, and molecular simulations in a model Li$_x$Si material explicitly demonstrate the development of excess energy and associated reduction in plastic yield stress during discharging, and thus validate key concepts of our model. This physical mechanism is introduced into both a thermally-activated flow model and a thermally-activated relaxation model for relaxation of the amorphous structure, creating a closed material model that captures both the intertwined energetic and kinetic responses of the material. We then exercise the model in various experimentally-achievable geometries and demonstrate how the yield stress of Li$_x$Si depends on the rate of charging/discharging, on the mechanical constraints imposed on the system, and on the overall history of the material including cyclic charging/discharging.

The remainder of this paper is organized as follows. In Sec. 2.2, we discuss the key concepts of the model and the general form of the constitutive model. We also validate the concept of excess energy and its effect on plastic flow using MD simulations. In Sec. 2.3 we present a framework for plasticity in the Li$_x$Si amorphous system. We then propose evolution equations for excess energy based on established metal glass models. We also discuss material parameter extraction from MD simulations. Based on the model developed, we perform few experimentally relevant tests and present the material model response in Sec. 4.4. Finally, we summarize and conclude in Sec. 2.5.

2.2 Plastic Softening in Amorphous Li$_x$Si due to Charging/Discharging

2.2.1 Mechanistic Concept and Formalism

The mechanical properties, in particular the plastic flow stress and underlying relaxation kinetics, of an amorphous material depend on the degree of structural disorder in the material. In well-studied systems such as metallic glasses, the degree of structural disorder depends on the initial relaxation as well as applied stress [Rodney et al.(2011)Rodney, Tanguy, and Vandembroucq]. Increases in structural disorder reduce activation barriers for material deformation and thus lower the flow stress of the material. In contrast, decreases in structural disorder occur during annealing and make amorphous materials more brittle [Rodney et al.(2011)Rodney, Tanguy, and Vandembroucq]. The structure of an amorphous battery material can be altered by material injection or extraction during lithiation/delithiation in lithium-ion batteries. Our model here simply assumes that structural disorder increases during lithiation/delithiation in parallel with on-going glassy relaxation mechanisms that reduce the structural disorder. We formally represent structural disorder by an internal variable ζ. However, rather than focus on structural disorder, which is vague and difficult to measure, we concentrate on the excess energy stored in the material that is associated with the structural disorder, $E^{xc}(x,\zeta)$, at a

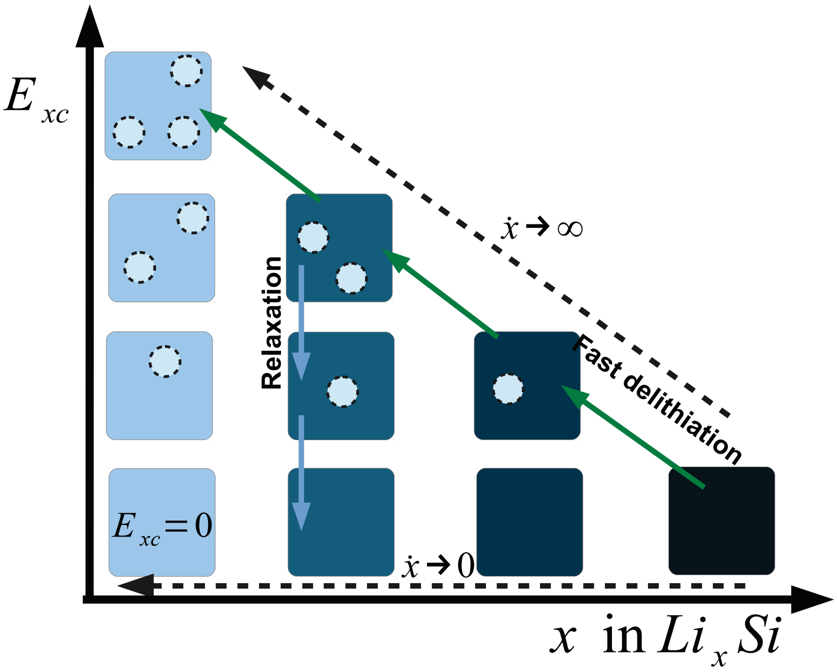

Figure 1 – Schematic of a hierarchy of $\mathrm{Li}_x\mathrm{Si}$ alloys of varying composition, coded with color intensity, and excess energy $E^{xc}(x,\zeta)$ or structural disorder, shown with light bubbles inside each box. Starting from high concentration and taking infinitely fast delithiation steps ($\dot{x} \to \infty$) results in the highest possible excess energy. Long thermally activated relaxation steps relax the sample and lower the excess energy. The lower row shows the fully relaxed amorphous materials that is achieved by very slow delithiation ($\dot{x} \to 0$). In MS simulation we only reach states by removing atoms (fast delithiation steps), thus very slow delithiations path is a combination of fast delithiation and relaxation steps.

given Li concentration x. Changes in structural disorder are associated with changes in excess energy, and we build a model for the kinetic evolution of the excess energy rather than the structural disorder.

The schematic of Fig. 1 illustrates the evolution of excess energy due to discharging and relaxation processes. Fig. 1 shows a hierarchy of $\mathrm{Li}_x\mathrm{Si}$ alloys of varying composition and varying amounts of excess energy $E^{xc}(x,\zeta)$. Here, "excess energy" refers to excess energy in the material relative to a reference material of the same composition but having relaxed to a state with structural disorder variable $\zeta_{ref}(x)$ at which further structural relaxation does not occur over experimental/simulation time scales. We imagine starting from a relaxed state having $\zeta_{ref}(x)$ at concentration x and discharging the material in $n = 1,2,...$ increments of concentration Δx. When lithium is removed from the material, there is rapid relaxation of the structure due to atomic rearrangements that relax any unstable mechanical state to a locally-stable mechanical state. However, the system is unable to relax immediately to $\zeta_{ref}(x - n\Delta x)$ at the new concentration because this would require atomic structural reconfiguration that cannot occur rapidly. There is thus increased structural disorder, and higher excess energy E^{xc} in the discharged material. If the discharging rate is infinitely fast, then the system evolves through a set of states as indicated in Fig. 1. If discharging is halted, e.g. at $x - 3\Delta x$, and the material is left to relax, then the excess energy will be reduced by relaxation processes at fixed alloy composition. The system will evolve toward ζ_{ref} at the current composition, as shown schematically in Fig. 1. If the same process is considered but starting from another initial concentration, e.g. $x-2\Delta x$, and discharged to the same final state, e.g. $x-3\Delta x$, we postulate that the structural disorder and excess energy of the system are the same as for a system that started at x, discharged to $x-3\Delta x$, and then relaxed for some time. In other words, the material state is uniquely characterized by the composition x and the structural disorder variable ζ, or equivalently by the excess energy density $E^{xc}(x,\zeta)$. The excess energy will then appear in the plastic flow model, lowering the applied stress needed for plastic flow at any specified strain rate and temperature.

To place the above schematic within a standard formal context, we define the Helmholtz free energy density ψ of the system in terms of the Li concentration x, the mechanical elastic strain tensor ε^e, and internal variable ζ, $\psi=\psi(x,\varepsilon^e,\zeta)$. We then decompose ψ into the sum of an energy density of the reference state, a mechanical (elastic) strain energy density, and an excess structural disorder energy density as

$$\psi(x,\varepsilon^e,\zeta) = \psi_{ref}(x,\zeta_{ref})+\frac{1}{2}C_{ijkl}(x,\zeta)\varepsilon^e_{ij}\varepsilon^e_{kl}+E^{xc}(x,\zeta) \tag{2.1}$$

From this free energy, the work-conjugate quantities of chemical potential for lithium μ_{Li} and the stress σ can be obtained in the standard manner(see Sec. 2.3). The free energy must be supplemented by evolution equations for the internal variables and by specification of the functions ψ_{ref}, C_{ijkl}, and E^{xc}; this constitutes the key physics of the problem. In this paper, we are not directly interested in the diffusion processes or the reference chemical potential and so specification of ψ_{ref} and ζ_{ref} is not necessary. We envision representative volumes of material wherein diffusion of lithium in the volume is fast relative to relaxation processes, with uniform concentration throughout the representative volume at all times, with the rate of charging/discharging $\dot{x}$ being imposed. For simplicity, we neglect the dependence of the elastic constants on the structural disorder, i.e. $C_{ijkl}=C_{ijkl}(x,\zeta_{ref})$. The important features in this work are thus the specification of the excess energy E^{xc} and the evolution equations for the structural disorder ζ. However, as the structural disorder ζ only appears in the specification of excess energy, we can choose to use an evolution equation for E^{xc} instead. In the following sections, we specify and validate $E^{xc}(x,\zeta)$, introduce a rate-dependent plastic flow theory that depends on E^{xc}, and then present an evolution equation for the excess energy based on models of glassy relaxation.

2.2.2 Validation of the Mechanistic Concepts

To support both the concept shown schematically in Fig. 1 and the relation between the material flow stress and discharging history, we have performed molecular statics simulations (zero temperature) to measure the excess energy and the flow stress of the amorphous Li-Si materials at a composition x after having discharged the system starting from some higher initial concentration by removing Li atoms. We focus on discharging because this process is far cleaner to simulate than charging, which involves insertion of atoms, but our conclusions are general. We used a recently developed second-nearest-neighbor modified embedded atom (2NN MEAM) potential [Cui et al.(2012a)Cui, Gao, Cui, and Qu] for lithium $\mathrm{Li}_x\mathrm{Si}$ alloys; this potential is sufficient for demonstration purposes. We fabricate various compositions of $\mathrm{Li}_x\mathrm{Si}$ by quenching from the melt to $T = 0.1^\circ K$ at a rate $3000(K/ns)$ and zero pressure. This is relatively high quenching rate, but the mechanical properties of the sample in uniaxial test does not change by reducing the quench rate to $500(K/ns)$ as shown in the results of Section 3.3.1. These samples are the reference $\mathrm{Li}_x\mathrm{Si}$ materials at each composition corresponding to the bottom row of materials indicated in Fig. 1. We measure the total potential energy of these as-fabricated samples. We then select a reference sample with concentration x_∞ and successively remove Li atoms in concentration increments of $\Delta x = 0.1$ by extracting Li atoms at random from the structure. After each increment of discharging, the material is relaxed at $T = 0^\circ K$ and $\sigma = 0$ to the local mechanically stable structure; this system has some volume V containing N total atoms $(Li + Si)$ and a total potential energy $V\psi(x, \sigma = 0, \zeta)$. The excess energy *per atom* is then obtained as $e^{xc} = VE^{xc}(x,\zeta)/N = V(\psi(x,\zeta) - \psi_{ref}(x,\zeta_{ref}))/N$ at the new composition x. Note that the internal variable ζ is unknown and irrelevant, but is indicated for completeness. In these simulations, the only relaxation in the atomic systems is athermal $(T = 0.1^\circ K)$ relaxation, and so the simulated process corresponds to an infinitely-fast discharging rate, and the label x_∞ is used to indicate the starting composition from which the infinite-rate discharging was performed. The procedure just described is executed for a range of starting compositions x_∞. We keep the temperature higher than absolute zero to use MD algorithms instead of molecular statics configurational optimization. For our simulations we use Nose-Hover thermostat in the LAMMPS molecular dynamics package.

Thermal energy can drive structural relaxation, and so the "excess energy" defined here might change if measured at finite temperature. This would thus seem to suggest that finite temperature simulation should be executed rather than molecular statics. However, there are a number of difficulties, operational and conceptual, that arise in executing MD. In addition to the fact that the excess energies are fairly small (see below) and thus comparable to $\frac{3}{2}kT$, executing MD raises the possibly of additional structural relaxation that is not directly connected with the excess energy. The MD glasses have been quenched, and thus are subject to possible further relaxation much faster than in a real material, making the relaxation problem more likely in such specimens. Thus, measuring the desired quantity becomes uncertain. Second, finite temperature studies are always defined by the time scale of the simulation. The system can overcome barriers that are accessible at temperature T over the time scale of the simulation; thus, the measured quantities depend on the simulation time and temperature. Third, correlating the excess energy with the associated flow stress at finite T and finite strain rate then also becomes far more difficult, and is not as well-defined (Eq. 2.9 and 2.10). By studying the relaxation, excess energy, and flow stress at $T = 0$, all quantities are clearly measured, are independent of any artificial time scales, and can be related to one another with high certainty.

The resulting excess energy per atom $e^{xc}(x,\zeta)$ as a function of the final Li concentration x is shown in Fig. 2a. As postulated, and shown schematically in Fig. 1, the excess energy per atom is, within numerical noise, a $single-valued$ function of the concentration x and the history of discharging which, in our procedure, is uniquely related to the starting concentration x_∞. In other words, a given $e^{xc}(x,\zeta)$ can only be achieved by following one specific infinitely-fast discharging path - it is not possible to reach the same $e^{xc}(x,\zeta)$ starting from two different initial x_∞. Thus, $e^{xc}(x,\zeta)$ is a unique energy associated with concentration x and internal structural disorder variable ζ, even though ζ remains implicit. At any concentration x, the excess energy is larger for samples that experienced a larger amount of discharging, equivalent to a higher initial composition x_∞, to achieve concentration x. Due to their inability to relax by thermal processes, the materials with higher excess energy presumably have higher structural disorder. Furthermore, the convergence of e^{xc} at low x independent of the amounts of discharging (independent of x_∞ for larger x_∞) is expected because when the material has been highly depleted of Li, it is very unstable and the resulting relaxation of the structure is more like a structural collapse from a very porous structure to a denser instantaneously-quenched amorphous structure that is largely independent of the starting structure. These simulations directly validate the first main mechanistic concept of this paper: discharging creates excess (stored) energy in the material with a unique relationship between the excess energy and the (implicit) structural disorder.

The quantity x_∞ refers to the initial state of a given simulation subjected to infinitely fast discharging. Our results show that the excess energy at (x,ζ) depends only on x and x_∞ and so it is accurate, convenient, and precise to express the excess energy in terms of x and x_∞ rather than x and ζ, $e^{xc} = e^{xc}(x, x_\infty)$. Furthermore, we find that all of the results in Fig. 2a can be reasonably collapsed onto a single universal curve, as shown in Fig. 2b, accurately represented as

$$e^{xc}(x, x_\infty) = e^{xc}(\frac{x}{x_\infty}) = e_0^{xc}(1-(\frac{x}{x_\infty})^2) \tag{2.2}$$

where $e_0^{xc} \approx 0.1eV$ is the maximum possible excess energy. This collapsed representation facilitates numerical results presented in Sec. 4.4.

Turning to the influence of the excess energy on the plastic flow, we have performed additional simulations. For each mechanically-stable MD system reached by discharging, i.e. for each state characterized by x and x_∞ with measured excess energy $e^{xc}(x, x_\infty)$, we have performed a simple tension test in MD at $T = 0°K$ and measured the stress-strain response of the material. Fig. 2c shows the stress-strain behavior for one specific composition, $x = 1$, reached from different starting compositions $x_\infty \geq 1$. The stress-strain curves show an initial elastic response and then a non-linear regime culminating in a plateau stress that corresponds to the plastic yield/flow stress. The elastic modulus E decreases slightly with the amount of discharging or, equivalently, increasing excess energy; as noted earlier, we neglect this effect in subsequent analyses, for simplicity. Most importantly, the plastic yield stress *decreases* with *increasing* e^{xc}: at the same composition x, materials with higher excess energy have lower plastic yield stress. The generality of this result is shown in Fig. 2d, which shows the plastic yield stress versus

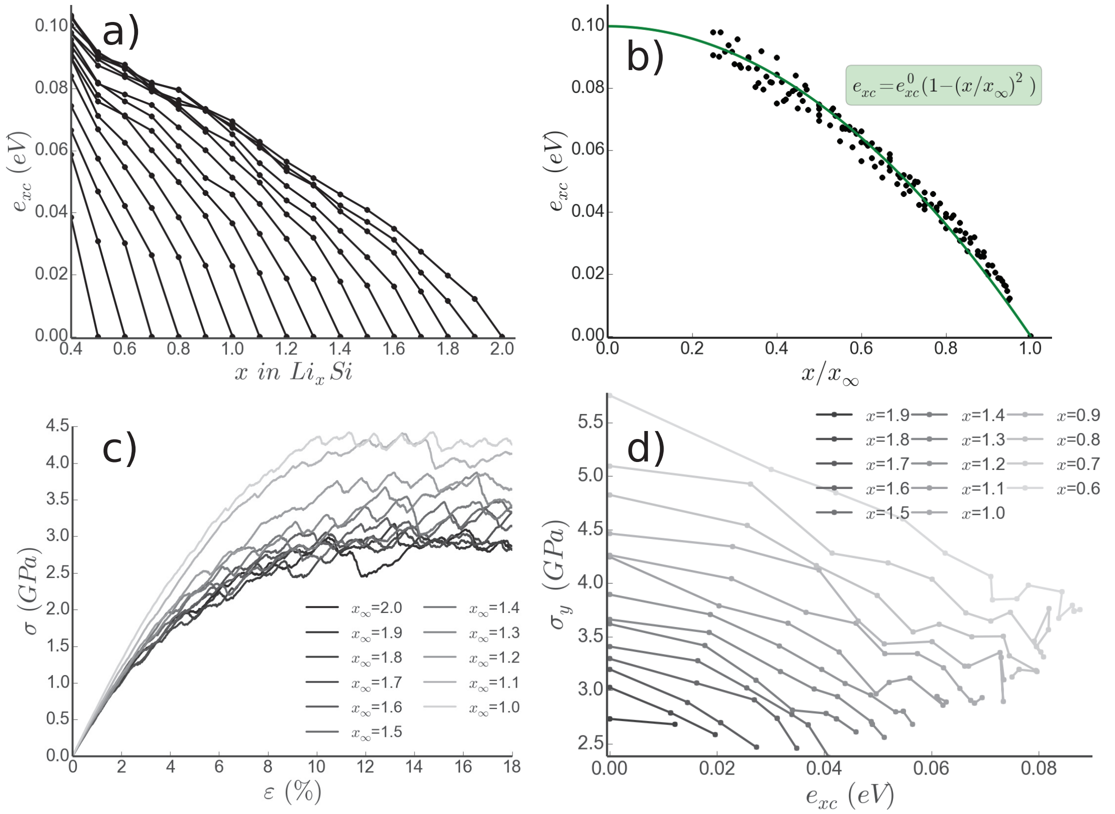

Figure 2 – a) Excess energy per atom (e^{xc}) in Li$_x$Si during unequilibrated delithiation. b) Collapsed excess energy data with respect to x/x_∞ and the fitted curve. c) Stress-strain curve of LiSi alloy delithiated from different starting compositions, x_∞. d)Yield stress (σ_y) of Li$_x$Si alloys with different lithium content as a function of excess energy. Yield stress is a decreasing linear function of excess energy.

excess energy as measured by MD simulations across the entire range of compositions and discharging studied here. For every concentration x, the yield stress is a decreasing function of the excess energy e^{xc}. These simulations validate the second mechanistic concept of this paper: higher excess energy (due to discharging) leads to easier plastic flow (lower yield stress) of the material.

During the delithiation process we also measured the excess volume created in the system. Excess volume per atom $v^{xc} = (V(x,\zeta) - V_{ref}(x,\zeta_{ref}))/N$ is defined in a similar way to excess energy as the volume of the discharged system subtracted by the volume of equilibriated structure per atom in the system and the volumetric excess strain is defined as $\varepsilon_v^{xc} = v^{xc}/v^*$. Figure 3 shows the excess volumetric strain as a function of composition and discharging state. The excess volume created in the first discharching step can not be annihilated in the material but by further depletion of atoms the excess volume is annihilated to a good extent. Comparing the excess volume and excess energy shows that the excess energy, and change in the yield stress which is associated with the excess energy, are independent of the change in excess volume. Excess energy variations correlates much better with the change in the yield

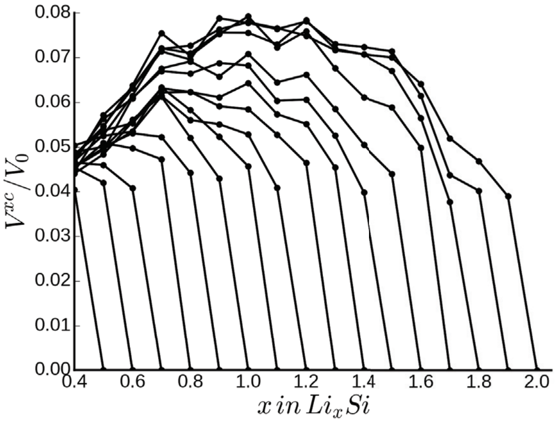

Figure 3 – Excess volumetric strain in $\mathrm{Li}_x\mathrm{Si}$ during delithiation.

stress than the excess volume.

2.3 Constitutive Behavior

In the previous sections, we presented and validated the overall concept that discharging/charging injects excess energy into the amorphous material and that this excess energy facilitates plastic flow. We introduced the excess (Helmholtz free) energy and expressed the problem in terms of the three variables concentration x, strain ε^e and the implicit structural disorder variable ζ which is related to the excess energy. To complete the model, here we develop the constitutive models for plastic flow and for structural evolution, which is framed in terms of evolution of the excess energy.

The mechanics of plastic flow follows the standard formulation. We consider one particular composition as a reference system for the mechanical strain. The total strain ε of any system is then composed of elastic, plastic, and “chemical" contributions,

$$\varepsilon = \varepsilon^c + \varepsilon^p + \varepsilon^e + \varepsilon^{xc}_v. \tag{2.3}$$

Here, ε^{xc}_v is the volumetric excess strain (shown in Fig. 3) which we ignore for our analysis here. The chemical strain arises from the swelling/shrinkage during charging/discharging measured relative to the reference system. The associated chemical strain rate can be written in terms of the concentration x and the charging/discharging rate $\dot{x}$ as

$$\dot{\varepsilon}^c_{ij} = \frac{\beta}{3}\frac{\dot{N}_{Li}}{N}\delta_{ij} = \frac{\beta}{3}\frac{\dot{x}}{x+1}\delta_{ij} \tag{2.4}$$

where β is the linear expansion coefficient due to charging, i.e the change in volume due to adding one lithium atom divided by the average atomic volume v^*. The plastic strain rate is related to the effective isotropic plastic shear rate $\dot{\gamma}^p$ via the standard isotropic flow theory as

$$\dot{\varepsilon}^p_{ij} = \dot{\gamma}_p(\tau^e)\frac{s_{ij}}{2\tau^e} \tag{2.5}$$

where $s_{ij} = \sigma_{ij} - \sigma_m \delta_{ij}$ is the deviatoric stress with $\sigma_m = \frac{1}{3}\sigma_{kk}$ as the mean stress and $\tau^e = \sqrt{s_{ij}s_{ij}/2}$ is the so-called effective stress. The key aspect is the specification of the plastic flow law $\dot{\gamma}_p(\tau^e)$ as discussed in the next Section.

2.3.1 Rate-dependent Plastic Flow

Generally, material plastic flow is controlled by thermally-activated processes that are driven by an applied shear stress. The applied shear stress couples to an activation strain tensor for the relevant process, and this driving force reduces the energy barrier of the flow process, accelerating the flow rate. We assumed a J_2 plasticity model for the amorphous material here. This assumption can be validated using MD simulation by calculating the yield surface, which we did not perform in this work. For an amorphous material, the mechanical response is isotropic and hence the flow response is written in terms of the effective shear stress τ^e. In the simplest kinetic model, the additional driving force reduces the energy barrier linearly, and the effective plastic shear strain rate $\dot{\gamma_p}$ is then obtained using transition state theory [Kocks et al.(1975)Kocks, Argon, and Ashby] as

$$\dot{\gamma_p} = \dot{\gamma}_0\, exp\left(-\frac{\Delta G}{kT}\right) 2\, sinh\left(\frac{\tau^e \Omega}{kT}\right) \tag{2.6}$$

where Ω is the activation volume for the shear event. The hyperbolic sine function arises from inclusion of both forward and reverse processes and leads to the limits of (i) zero strain rate at zero stress and (ii) a linear (viscous/creep) behavior at small stresses. The quantity $\dot{\gamma}_0$ is a characteristic material strain rate parameter that depends on the transition attempt frequency ν (for more details see [Argon(1979)] and [Kocks et al.(1975)Kocks, Argon, and Ashby]). At high applied stresses, the $sinh$ term is a simple exponential, and the plastic strain rate equation is of the form

$$\dot{\gamma_p} = \dot{\gamma}_0\, exp\left(-\frac{(\Delta G - \tau^e \Omega)}{kT}\right) \tag{2.7}$$

Rate-dependent flow in bulk metallic glasses has been well-represented by similar relationships, with the linear decrease in energy barrier with stress emerging as an expansion of other functional forms [Pan et al.(2008)Pan, Inoue, Sakurai, and Chen]. Consistent with the "shear transformation zone" (STZ) concept for glassy flow, the measured strain rate sensitivity $m = \partial\, ln(\tau^e)/\partial\, ln(\dot{\gamma_p})$ is quite small, $m \approx 0.01 - 0.02$, corresponding to a large activation volume $\Omega >> v^*$, and a large free energy barrier $\Delta G \approx 3 - 5eV$ [Pan et al.(2008)Pan, Inoue, Sakurai, and Chen]. Li-Si glasses are expected to follow a similar flow law with similar trends related to STZ behavior.

In the present model, the excess energy generated by charging or discharging, and not yet relaxed by other processes, reduces the energy barrier for thermally-activated processes. Physically, the excess energy corresponds to higher-energy atomic configurations in the overall energy landscape and thus thermally-activated processes are more easily overcome when starting from these higher-energy atomic configurations, independent of the applied stress. The thermally activated processes in glasses involve many atoms in the STZ and so the available excess energy is the excess energy stored in an STZ, which is the excess energy per atom e^{xc} multiplied by the number of atoms in the STZ, which in turn is some multiple of the STZ activation volume Ω. Based on these considerations of glassy flow, we incorporate the excess energy into the constitutive model for the plastic strain rate as

$$\dot{\gamma}_p = \dot{\gamma}_0\, exp\left(-\frac{\Delta G_{ref} - (\alpha\Omega/v^*)e^{xc}}{kT}\right) 2\,sinh\left(\frac{\tau^e\Omega}{kT}\right) \tag{2.8}$$

where α is the ratio of the volume of atoms in the STZ relative to the STZ activation volume. Here, we are interested in (i) the flow stress at a given loading rate and (ii) high stresses (so that $\tau^e\Omega \gg kT$), and so we invert equation 2.8 to obtain

$$\tau^e = \frac{kT}{\Omega}\, ln\left(\frac{\dot{\gamma}_p}{\dot{\gamma}_0}\right) + \left(\frac{\Delta G_{ref}}{\Omega} - \frac{\alpha e^{xc}}{v^*}\right) \tag{2.9}$$

where we have suppressed dependencies on x and ζ. However, we note that $\Delta G_{ref} = \Delta G(x, \zeta_{ref})$ is the activation barrier for plastic flow in the reference state associated with the free energy $\psi(x, \sigma = 0, \zeta_{ref})$ and, as before, $e^{xc} = e^{xc}(x, \zeta)$. We validate this model using the previous MD results. At $T = 0°K$, Eq. 2.9 gives the zero-temperature flow, or yield, stress as

$$\tau^e_{y0} = \frac{\Delta G_{ref}}{\Omega} - \frac{\alpha e^{xc}}{v^*} \qquad \text{for} \quad T = 0°K \tag{2.10}$$

At $T = 0°K$, the flow stress should thus decrease linearly with e^{xc}, independent of γ_0 and $\dot{\gamma}$, and at a rate dependent only on v^*/α. Fig. 2d shows the measured flow stress vs. the measured excess energy, and indeed a linear scaling with a composition-independent slope is measured across the entire spectrum of systems. This supports an important tenet of the flow model.

From the measured scaling in Fig. 2d, we can extract values for $\Delta G_{ref}/\Omega$ and v^*/α corresponding to the as-quenched MD amorphous materials. We assume a single v^*/α for all materials and obtain $v^*/\alpha = 12.5\text{Å}^3$. With an atomic volume of $v^* = 17.2\text{Å}^3$, this yields $\alpha \approx 1.38$. The intercept corresponds to the $T = 0°K$ yield stress at zero excess energy for any concentration x, $\tau^e(x, \zeta_{ref}) = \Delta G_{ref}/\Omega$. We cannot obtain ΔG and Ω independently. However, assuming that the rate sensitivity for the relaxed Li-Si alloys is comparable to that for bulk metallic glasses, $m = 0.015$, we can compute the activation volume as $\Omega = kT/(m\tau^e_{y0}) \approx 100\text{Å}^3$, and then further obtain $\Delta G_{ref}(x) = (2.81 - 1.58x + 0.34x^2\, eV)$ over the range $0.5 < x < 2.0$. For the MD-simulated materials, which are not a precise model for real Li-Si, the estimated activation volume is then approximately 6 atomic volumes, the STZ volume $\alpha\Omega/v^*$ is approximately 8 atomic volumes, and the average energy barrier is $\sim 1.42eV$; these are somewhat smaller than values estimated for bulk metallic glasses, but are obtained from the quenched MD material, which likely has more structural disorder than experimentally-prepared materials. Thus, these estimates for the material parameters remain reasonable but are not meant to be precise.

The reference plastic strain rate $\dot{\gamma}_0$ should be approximately the fundamental rate of atomistic vibration $\approx 10^{12}/s$ divided by number of atoms in the STZ and multiplied by the increment of strain associated with an individual transition. We use a value of $5 \times 10^8/s$; since $\dot{\gamma}_0$ appears only in an logarithm term when calculating the stress(Eq. 2.9), the precise value around this value has negligible effect on the stresses.

2.3.2 Creation and Annihilation of Excess Energy

The final component of the model is the evolution of the structural disorder ζ or, equivalently, of the excess energy e^{xc}. In the absence of charging or discharging, the evolution of either ζ or e^{xc} is analogous to the general problem of relaxation kinetics in glassy systems, which is an active area of current research that we do not wish to attempt to resolve here. The various theories (free volume [Spaepen(1977)], STZs [Argon(1979), Falk and Langer(1998)], effective temperature models [Ono et al.(2002)Ono, O'Hern, Durian, Langer, Liu, and Nagel]) all aim to quantify the concept of structural disorder and its evolution by making assumptions about the underlying microscopic mechanisms. The common feature of all the models is the existence of two distinct mechanisms for evolution of structural disorder: (i) time-dependent thermally activated relaxation/annihilation of structural disorder and (ii) stress-assisted creation of structural disorder. In the present model, we include the additional evolution of structural disorder associated with charging/discharging. Moving from the structural disorder (ζ) to the more-explicit excess energy $e^{xc}(x,\zeta)$, we have three contributions to the evolution of the excess energy,

$$\dot{e}_{xc} = \left|\frac{\partial e_{xc}}{\partial x}\dot{x}\right| + \dot{e}^{a}_{xc} + \dot{e}^{s}_{xc} \tag{2.11}$$

Above, $|\partial e_{xc}/\partial x\, \dot{x}|$ captures the effect of charging/discharging where the absolute value ensures that both charging and discharging create excess energy, while $\dot{e}^{a}_{xc}$ and $\dot{e}^{s}_{xc}$ capture the effects of relaxation/annihilation and stress-assisted creation of excess energy, respectively.

The creation and annihilation processes are thermally activated microscopic processes of atomic re-arrangement and are thus associated with the same energy barriers that control plastic flow, which depend on the excess energy itself as $\left[\Delta G_{ref}(x,\zeta_{ref}) - \alpha\Omega e^{xc}/v^*\right]$. Both annihilation and creation processes are also modified by an applied stress, but relaxation can occur even in the absence of applied stress. The annihilation process also presumably slows down as the excess energy is reduced, reflecting the fewer microscopic paths available to relax the remaining excess energy; this is responsible for the typical slow relaxation of glassy materials. Finally, under stress, a steady-state behavior should emerge where e^{xc} and the plastic strain rate attain some constant limiting values. These features are generally captured via the two evolution equations

$$\begin{aligned}\dot{e}^{a}_{xc} &= -\nu \exp\left(-\frac{\Delta G_{ref} - (\alpha\Omega/v^{*})e^{xc}}{kT}\right)\cosh\left(\frac{\tau^{e}\Omega}{kT}\right)e_{xc}\\ \dot{e}^{s}_{xc} &= \nu C_{s} \exp\left(-\frac{\Delta G_{ref} - (\alpha\Omega/v^{*})e^{xc}}{kT}\right)\left[\cosh\left(\frac{\tau^{e}\Omega}{kT}\right)-1\right]e^{0}_{xc} \qquad (2.12)\end{aligned}$$

Here, ν is a microscopic attempt frequency for the thermally-activated processes that is expected to be an atomic frequency ($\approx 10^{12}/s$) divided by the number of atoms involved in the STZ process. In the stress-driven creation term, the energy is scaled by the maximum excess energy e^{xc}_{0} and an additional constant C_s is then introduced to capture the relative rates of annihilation and creation. At large stress, the excess energy evolution is

$$\dot{e}_{xc} = \nu \exp\left(-\frac{\Delta G_{ref} - (\alpha\Omega/v^{*})e^{xc} - \tau^{e}\Omega}{kT}\right)\left(C_{c}e^{xc}_{0} - e_{xc}\right) \qquad (2.13)$$

so that, independent of the initial excess energy (structural disorder), a steady state will be achieved due to a balance of excess energy creation and annihilation. The flow stress will show a similar steady state behavior independent of the initial structure. This long-time behavior is consistent with molecular dynamics simulations of amourphous metals with different initial conditions, i.e., different quenching rates and thus different initial structural disorder [Rodney and Schroder(2011)], as well as previous free volume [Steif et al.(1982)Steif, Spaepen, and Hutchinson] and STZ [Langer and Pechenik(2003)] models. The condition for the steady-state is $C_{c}e^{xc}_{0} - e^{steady}_{xc} = 0$. Since the maximum possible steady state excess energy in our MD simulations is e^{0}_{xc}, we have the constraint of creation constant $C_s < 1$.

2.3.3 Chemical Potential and Stress

Using free energy as given in Eq. 2.1 and the strain decomposition, the work-conjugate quantities of chemical potential for lithium μ_{Li} and the stress σ can be obtained using thermodynamic definitions. Specifically,

$$\sigma_{ij} = \frac{\partial\psi}{\partial\varepsilon^{e}_{ij}} = C_{ijkl}(x,\zeta)\varepsilon^{e}_{kl}\,, \qquad \mu_{Li} = \frac{\partial(V\psi)}{\partial N_{Li}}|_{\varepsilon^{e},\zeta} - \beta v^{*}\sigma_{m} \qquad (2.14)$$

The elastic strain follows Hooke's law. The glassy structures are isotropic due to their randomness, and the two elastic constants G and E as measured in our MD-simulated materials are presented in Table 1. For the chemical potential we obtain:

$$\mu_{Li} = v^{*}\left[\psi_{ref} + E^{xc}\right] + v^{*}(x+1)\left[\frac{\partial\psi_{ref}}{\partial x} + \frac{\partial E^{xc}(x,\zeta)}{\partial x}|_{\zeta}\right] - \beta v^{*}\sigma_{m} \qquad (2.15)$$

The chemical potential consists of several parts. The term $v^{*}\psi_{ref}$ is the energy of atoms added to the reference material. The derivative of ψ_{ref} with respect to x reflects the change in the energy of the reference state due to the composition change. These two terms constitute the usual equilibrium chemical potential in a stress-free system. The term $v^* E^{xc}$ is the excess energy upon adding atoms and thus shows that the excess energy is directly reflected in the measured chemical potential. The derivative of E^{xc} at constant structural disorder ζ also exists but is not computable in our theory since ζ is implicit; we envision this term makes a minor contribution to the chemical potential. Finally, the term $\beta v^* \sigma_m$ term is the standard term reflecting the work done by any applied stress on the system by insertion of volume βv^*.

2.3.4 Implementation and Material Parameters

The combination of Eqs. 2.1, 4.16 and 2.11 provides a complete description for the evolution of plastic and chemically-induced strain rates and excess energy for a unit of material undergoing charging or discharging. To exercise the material model and demonstrate major features of the effects of charging/discharging on plastic flow, we consider geometries having a uniform state of stress and dimensions (nanoscale) where diffusion is fast so that the chemical composition is uniform throughout the sample at any instant of time. Under these conditions, mechanical equilibrium is satisfied trivially. All other governing equations are then reduced to the following system of coupled ordinary differential equations:

$$\begin{aligned}
\dot{x} &= \dot{x}_{ext} \\
\dot{\sigma}_{ij} &= C_{ijkl}\dot{\varepsilon}^e_{kl} \\
\dot{\varepsilon}^e_{ij} &= \dot{\varepsilon}_{ij,ext} - \dot{\varepsilon}^c_{ij} - \dot{\varepsilon}^p_{ij} \\
\dot{e}_{xc} &= \dot{e}^c_{xc} + \dot{e}^a_{xc} + \dot{e}^a_{xc}
\end{aligned} \tag{2.16}$$

Here σ_{ij}, C_{ijkl}, and ϵ_{kl} are the components of the general stress, elastic constant, and strain tensors, with pertinent values depending on the loading condition. The system of equations is solved using the backward Euler method. Boundary/initial conditions are the rate of charging/discharging $\dot{x}_{ext}$ and either the externally applied strain rate $\dot{\varepsilon}_{ext}$ or the applied stress $\dot{\sigma}_{ext}$.

The model has a number of material parameters. Our MD simulations provide approximate but not chemically-accurate values for some of these parameters, and we have invoked associated results for bulk metallic glasses to estimate other key parameters. Specifically, MD- simulated silicon rich compounds are somewhat stiffer than the real material [Cui et al.(2012a)Cui, Gao, Cui, and Qu], and higher ΔG values obtained for these compounds can alter the results significantly. Moreover, to clearly show the effects of fundamental features of the model due to competition of charging/discharging and plasticity effects, we use mean values for the concentration dependent properties ΔG and elastic constants. For comparison we include one test using composition-dependent properties in Sec. 2.4.4. All material parameters used in our example studies are summarized in Table 1.

Table 1 – Parameters of the model which are used in the simulations

Parameter	Description	Values
Parameters obtained from MD or calculated using them		
v^* (Å^3)	Average atomic volume	17.2
E^{xc} (eV)	Excess energy	$0.1\left(1-\left(\frac{x}{x_\infty}\right)^2\right)$
E $(eV/\text{Å}^3)$	Elastic modulus (mean value)	$0.836-0.211\,x$ (0.572)
G $(eV/\text{Å}^3)$	Shear modulus(mean value)	$0.337-0.087\,x$ (0.227)
ΔG_{ref} (eV)	Sliding energy barrier(mean value)	$2.81-1.58\,x+0.34\,x^2$ (1.42)
α	Geometrical constant (Eq. 2.8)	1.38
ν $(1/s)$	Attempt frequency	1.25×10^{11}
Ω (Å^3)	Activation volume	100
Assumed parameters		
C_s	e^{xc} creation rate factor modifier	0.5
m	Strain rate sensitivity	0.015
$\dot{\gamma}_0$ $(1/s)$	Reference plastic strain rate	5×10^8
β	Chemical strain coefficient	0.9

2.4 Results

Here, we apply the entire model to study the stress-strain evolution of Li-Si battery materials under several common experimental configurations. We first study the mechanical response under tension of a freely-suspended nanowire immediately after Li discharging. We also look at relaxation response of the nanowire after Li discharging. We then examine the response of a thin film constrained on a substrate, where the stress develops due to the discharging, leading to simultaneous coupled mechanical and chemical phenomena. We then study the cyclic response of the constrained thin film under discharging followed by charging and then discharging a second time. Finally, we show results of the model when using composition dependent properties.

Rates of charge/discharge are expressed in terms of the experimentally-relevant rates, i.e. C-rates. A discharge of $1C$ draws a current under which the battery would deliver its nominal capacity in one hour. A rate of $1C$ for Li$_x$Si corresponds to $\dot{x}=1.164\times10^{-3}\ /s$. All studies are performed at $T=300^\circ K$.

2.4.1 Tension Test on a Discharged Nanowire

In a nanowire, diffusion through the cylindrical surface is sufficiently fast that we can neglect concentration gradients in the wire. During discharging, we imagine that the nanowire is free-standing, i.e. not attached to any substrate, so that it can contract freely during the discharging. Immediately after discharging, the nanowire is then subjected to a uniaxial tension test at

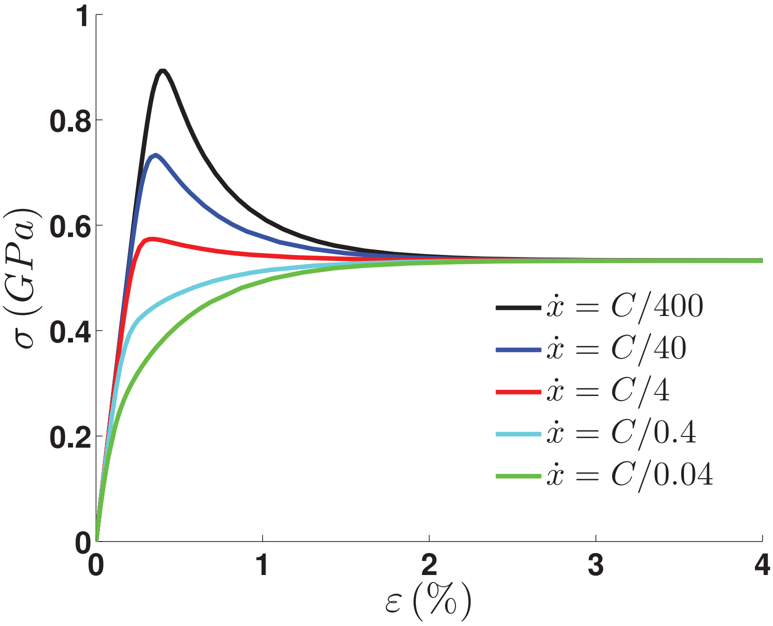

Figure 4 – Axial stress (σ) versus axial strain(ε) in LiSi nanowires that were previously discharged at different rates as indicated. All tests are done at a strain rate of $\dot{\varepsilon} = 10^{-3}/s$ and start immediately after discharging is complete.

a specified loading rate. The amount of excess energy at the end of the discharging step depends on the discharging rate $\dot{x}$ and then, during the mechanical test, this excess energy is relaxed by annihilation processes but, as the stress increases, excess energy is also created by stress. The overall mechanical response thus depends on the previous discharging rate and the subsequent applied strain rate.

The details of the specific numerical example are as follows. We start with an initially charged Li_xSi alloy at $x = 2$ with an assumed initial excess energy of $e^{xc} = 0.01\, eV$. This sample is then discharged uniformly at different rates $\dot{x}$ until the alloy composition corresponds to $x = 1$. Discharging is then halted ($\dot{x} = 0$) and the samples are immediately subjected to a uniaxial tension test along the axis of the nanowire at an imposed tensile strain rate of $\dot{\gamma} = 10^{-3}\ 1/s$.

Fig. 4 shows the predicted stress-strain curves for nanowires discharged at different rates. The nanowire discharged at the highest rate starts to flow plastically at the lowest stress, reflecting that the high-rate discharging injects more excess energy into the nanowire and over a shorter time which lowers the amount of annihilation. At low rates of discharging, the excess energy creation is negligible, the structure is more stable, and thus higher stresses are needed to drive plastic flow. Eventually, all systems reach the same dynamic steady-state in which the excess energy creation and annihilation processes balance, and there is no memory of the original discharging.

We also study the relaxation of the excess energy in the nanowire specimens after discharging

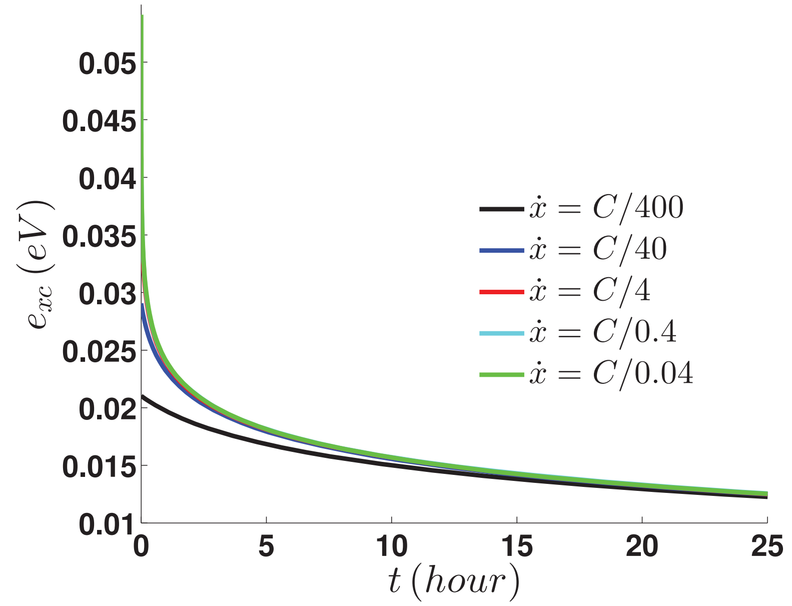

Figure 5 – Evolution of excess energy in LiSi nanowires after discharging is complete, for different rates of discharging under zero applied load.

under no applied loading. The relaxation of the excess energy versus time is associated with the relaxation of the chemical potential. This chemical potential change should be directly measurable as a change in electric potential U of the material relative to a reference system, with $\mu = qU$ where q is the Li charge. Of interest is the change in chemical potential $\Delta\mu = \mu(t) - \mu(0)$ and among four terms in Eq. 2.15, ψ_{ref} and its derivative do not change during the relaxation process at fixed composition x and the stress is also zero. Thus, the change in chemical potential is

$$\Delta\mu = \left[e^{xc},_t - e^{xc},_0\right] + (x+1)\left[\frac{\partial e^{xc}}{\partial x}|_{\zeta,t} - \frac{\partial e^{xc}}{\partial x}|_{\zeta,0}\right] \tag{2.17}$$

We are not able to calculate the derivative of excess energy with respect to x at constant ζ constant but we expect that the change in excess energy due to structural disorder as the concentration varies is minor. We thus assume that e^{xc} is the main part of the voltage drop during relaxation. Fig. 5 shows the excess energy versus time during relaxation after the discharging is complete, for the different discharging rates. The excess energy, and thus voltage, is initially higher for higher rates of discharge but with faster relaxation than observed at lower discharge rates. Eventually, all systems relax toward the same limit. As the material relaxes more and the excess energy decreases, there are fewer transitions that can decrease the energy further and so the relaxation rate decreases steadily.

2.4.2 Mechanical Response of a Constrained Thin Film during Discharging

Mechanical testing of a thin film silicon on a substrate in an electrochemical cell has been performed experimentally by Sethuraman et al. [Sethuraman et al.(2012)Sethuraman, Van Winkle, Abraham, Bower, and Guduru]. In this test an amorphous silicon thin film on a thick substrate is subjected to charging/discharging, the sample deflection is measured, and the thin film stress calculated from the deflection. Here, we examine the same problem of delithiation of a thin film electrode. Diffusion from the free surface of the film throughout the thickness is assumed to occur fast enough so that the Li concentration is uniform through the thickness at any instant of time. The stiff substrate constraints the in-plane displacement so that a uniform biaxial stress develops throughout the film. We consider the film to have some initial excess energy, due to some prior history, discharge the film at different rates, and measure the biaxial stress induced in the film. In this problem, the elastic stress develops due to the volume change upon discharging, the excess energy evolves due to the discharging and loading, and plastic flow occurs when the stress reaches the yield stress associated with the current excess energy. This simple problem thus involves the full chemical-mechanical coupling inherent in the model. We start with an initially-charged Li$_x$Si alloy at $x = 2$ with two values for the initial excess energy ($e^{xc} = 0.02, 0.04\, eV$). The sample is then discharged uniformly at different rates $\dot{x}$ until the alloy composition reaches $x = 0.5$. The biaxial stress and excess energy of the thin film are measured and reported as a function of the lithium concentration x.

Fig. 6 shows the biaxial stress that develops in the Li$_x$Si thin film during the delithiation.

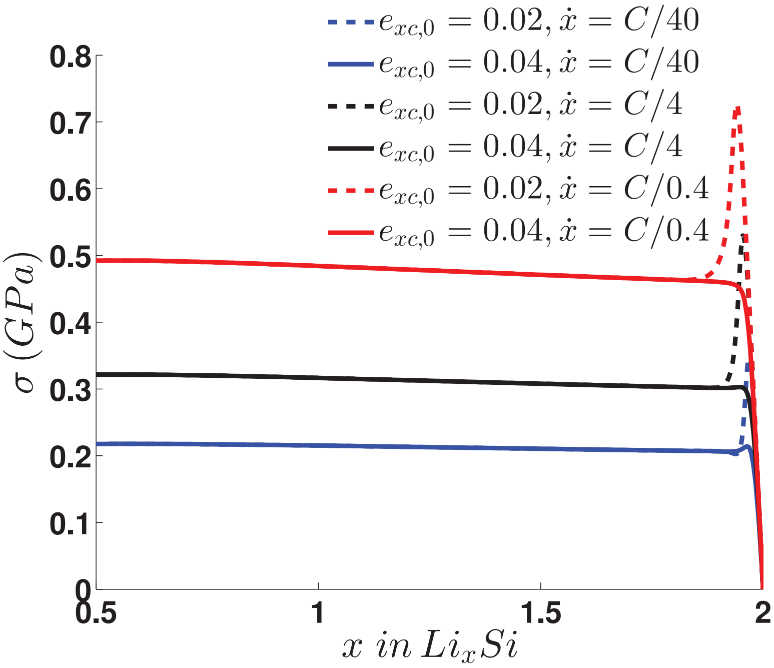

Figure 6 – Biaxial stress σ versus composition x in a confined Li$_x$Si thin film due to lithium discharge at different rates.

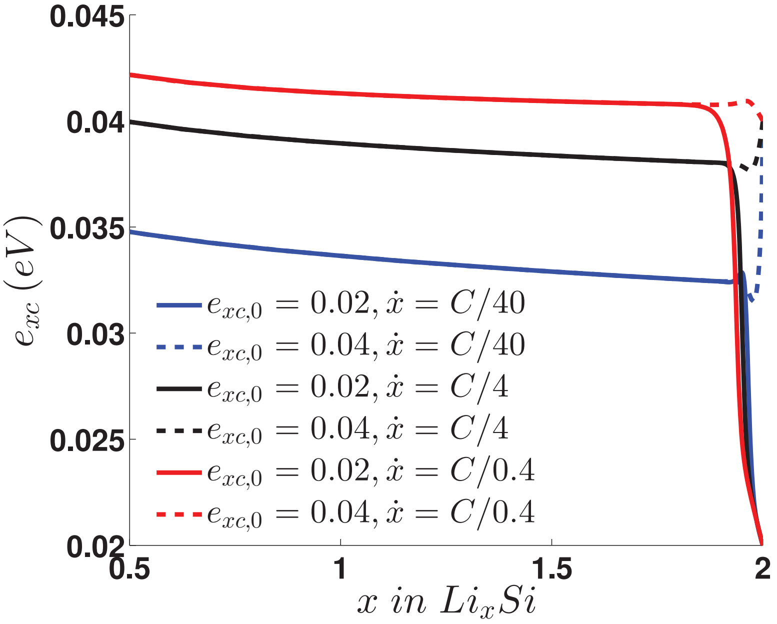

Figure 7 – Accumulated excess energy versus composition x in a confined Li_xSi thin film due to lithium discharge at different rates.

The (arbitrary) initial excess energy has only a transient effect - the material quickly attains a dynamic equilibrium determined by the competition between excess energy creation and annihilation terms in the evolution Eq. 2.11. The flow stress shows a substantial sensitivity to the rate of discharging, and the rate sensitivity is quite different than the intrinsic rate sensitivity of the reference material(s) in the absence of any discharging. The sensitivity of the stress to $\dot{x}$ is opposite to that seen in the previous test: lower rates of discharging result in lower flow stresses. However, while Fig. 7 shows that the excess energy increases with increasing discharge rate, the imposed strain rate also depends on the rate of discharge $\dot{x}$. The two mechanisms of (i) a rate of stress development due to the charging rate and (ii) a rate of stress softening due to increasing excess energy at higher discharging rates compete in the establishment of the plastic flow stress. The effect of excess energy in softening the material is qualitatively similar to the “reactive flow” model [Brassart and Suo(2012)], but here achieved within an explicit physical model based on the origins of rate-dependent flow in glassy materials.

Fig. 7 shows the accumulated excess energy in the thin film delithiation tests. Higher rates of discharge pump more excess energy into the material both because of linear dependence of chemical excess energy creation and also the higher stress. Higher excess energy tends to soften the material as seen in Fig. 6. Here, we observe a transient effect of the initial structural disorder in the material but after some time there exist a dynamical equilibrium for excess energy that is independent of the initial state of the material.

As before, the chemical potential of Li can be measured via electrical voltage. Here, the changes in chemical potential (overpotential) relative to systems without excess energy (i.e. relative to the reference materials) are due mainly to two contributions, e^{xc} and $\beta v^{*}\sigma_{m}$, with the derivative of the excess energy making a minor contribution. The two main contributions are of comparable magnitude. For instance, at a $C/4$ discharging rate, the pressure term at a biaxial steady state stress of $\sigma = 0.32GPa$ is $\approx 0.021eV$ while the contribution due to the steady state excess energy is $\approx 0.04eV$. The pressure term is well-known, and the overpotential is usually attributed solely to this term whereas our analysis suggests that the overpotential has an additional comparable contribution due to excess energy. This may be the origin of differences between the measured and expected stress-dependent voltage measured experimentally.

2.4.3 Cyclic Discharging/Charging of a Constrained Thin Film

Batteries are used in a cyclic mode of charging and discharging. Therefore, we investigate cyclic behavior of the thin film system under a sequence of charging/discharging cycles. In this paper, only discharging processes have been simulated in MD simulation. Charging simulations cannot be used to reveal the excess energy since the locations for atom insertion are uncertain and generate fictitious excess energies. However, we have postulated, and showed during discharging, that the material has two state variables, the concentration and the excess energy (or structural disorder ζ). Therefore, during charging, the system will have the same state variables. We assume that the value of excess energy of a system with specified composition x and structural disorder ζ is the same during charging and discharging, i.e. we use the same functional form and values for the excess energy for charging and discharging, $e^{xc}(x, x_{\infty})^{charge} = e^{xc}(x, x_{\infty})^{discharge}$. Here, we do not change the meaning of the x_{∞} for convenience: it is the concentration of the "equilibrium state" (x_{∞} , $e^{xc} = 0$) that leads to the current state (x, e^{xc}) upon infinitely fast *discharging*.

We model two subsequent cycles of discharging/charging between $x = 2.0$ and $x = 0.5$ at a rate of $\dot{x} = \mathrm{C}/4$, close to typical experimental rates of charging. Fig. 8 shows the stress versus composition during cyclic discharging/charging of a thin film, as predicted by the model using the above assumptions. The flow stress during the first discharging cycle is different than in subsequent cycles, reflecting that the flow stress depends on the history of the material. After the initial transient regime of the first cycle, however, the first and second cycles are essentially identical and the system attains a near-steady state cyclic behavior. The charging and discharging cycles are not mirror images of one another. For instance, once yielding starts, the stress during dischargning increases slowly with decreasing composition whereas the stress during charging decreases slowly with increasing composition. Also the slopes of the stress vs. composition upon reversal of the charging are slightly different. Such features also reflect the history dependence of the flow behavior that is contained within the model, even though the effects are modest for the material parameters and test conditions shown here.

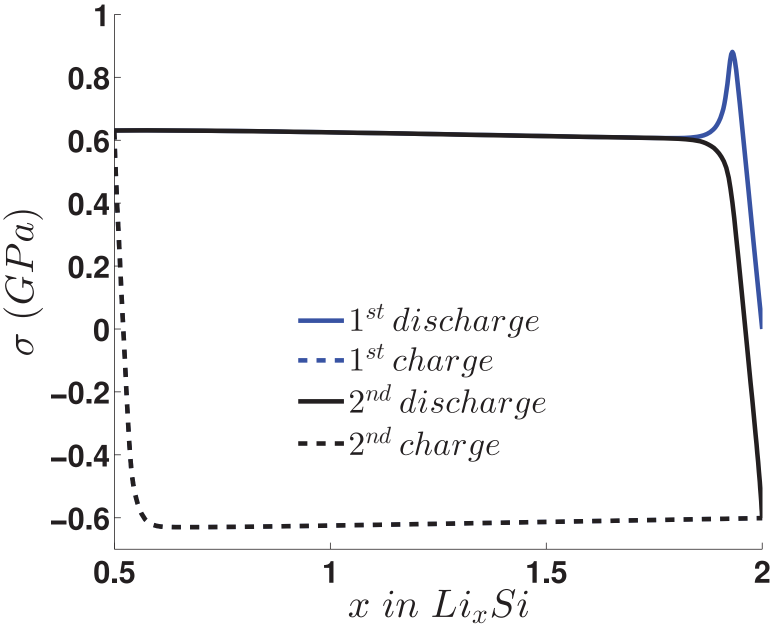

Figure 8 – Biaxial stress σ versus composition x in a $\mathrm{Li}_x\mathrm{Si}$ thin film due to lithium charge/discharge cycles at $C/4$ rate.

2.4.4 Discharging of a Thin Film: Composition-dependent Material Parameters

In all previous tests we used constant concentration-independent values for the energy barrier ΔG and elastic moduli E and G so as to more-clearly reveal the underlying flow behavior. In reality, these values are not constant with Li concentration. Molecular dynamics simulations reveal the composition-dependent variations of the moduli and flow stresses for the model Li-Si interatomic potentials used. Furthermore, the energy barriers as a function of composition have been calculated from Eq. 2.10 and using the data in Fig. 2d, as shown in Table 1. Our framework remains valid including these concentration-dependent material properties, and we provide one example case here for the thin film subjected to charging/discharging.

However, MD samples are not relaxed for long times during the quenching phase. Thus, the initial excess energy stored in the MD materials is larger than would be expected in real materials, and the corresponding energy barriers for flow are lower than expected in real material, leading to smaller values for yield stress. To obtain stresses in the range of recent experiments, we use the energy barriers calculated from MD but shifted by a constant value ΔG_0 to approximately capture the behavior of more-relaxed, more-realistic materials. Fig. 9 shows the biaxial stress evolution for the thin film subjected to one cycle of discharging/charging at a rate $\dot{x} = C/4$ using several choices for the shift ΔG_0. At high Li concentrations, the energy barriers and flow stresses are lower and so the flow stresses are lower. The flow stress increases significantly at lower Li concentrations where the energy barriers are much larger. The MEAM Li-Si potentials over-estimate the silicon network stiffness relative to first-principles results [Cui et al.(2012a)Cui, Gao, Cui, and Qu], resulting in higher energy barriers in the silicon-rich

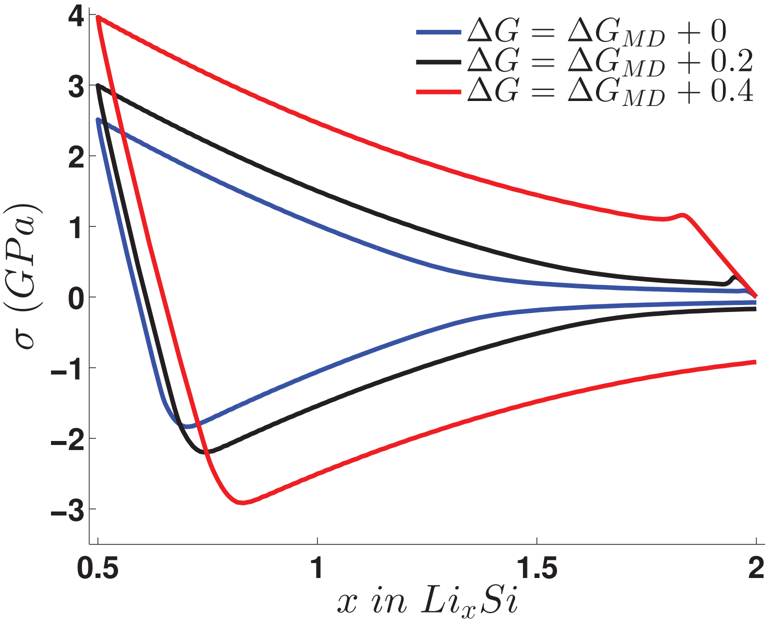

Figure 9 – Biaxial stress versus composition x in a Li$_x$Si thin film during one cycle with $\dot{x} = C/4$ and using elastic constants and ΔG varying with composition according to values obtained from MD simulations.

domain relative to real materials, which in turn corresponds to rather larger increases in yield stress at low Li content. Accurate results for a given material system require precise inputs; our goal here has been to present the physical concept and develop and exercise the model to demonstrate the general phenomena rather than to make quantitative predictions for real Li-Si.

2.5 Conclusion

We have proposed and developed a mechanistically-based constitutive model for amorphous battery materials, such as Li$_x$Si , based on the concept of excess energy stored in the material during charging/discharging. We have used MD simulation to validate the basic premises of the model, specifically the accumulation of excess energy and associated plastic softening of the material. The model is then able to predict the dependence of plastic softening as a function of the chemical and mechanical loading conditions as well as charging/discharging history of the material. The measured plastic flow stress is a result of the competition between excess energy creation and annihilation mechanisms. There are no purely phenomenological aspects in our model and the aspects such as the glassy plastic flow model could be enhanced as new understanding of glassy flow emerges. All parameters in our model could be measured/calibrated or calculated, although this remains challenging. We expect that the general trends predicted by the model, including the relaxation behavior of the excess energy as reflected in the measured chemical potential, may be pertinent for explaining observed phenomena and trends in recent experiments. We will pursue this direction in future work. The present model does not explicitly address the processes of Li diffusion through the material. Diffusion processes could drive either faster relaxation or create further excess energy. The excess energy due to insertion/removal of Li might also affect the driving forces for diffusion. Consideration of the implications of our current model on Li transport remains open for future research. Finally, we envision that the present constitutive model can be employed in realistic geometries/microstructures using the finite element method so as to capture the full complex evolution of coupled chemical-mechanical evolution including plastic flow that arises in these amorphous battery materials.

3 Fracture in amorphous Li-Si alloys

Silicon is among the highest Li-storing anode materials in Li-ion batteries, but the large capacity is accompanied by significant volume expansion that causes mechanical failure. Recent experimental studies have been performed on the fracture of lithiated silicon, with conflicting results [Pharr et al.(2013)Pharr, Suo, and Vlassak, Wang et al.(2015)Wang, Fan, Wang, Wang, Tao, Yang, Liu, Chew, Mao, Zhu, et al.]. However, at present, there is no mechanistic model for the fracture of these materials, which motivates our systematic atomistic simulation of fracture in lithiated silicon. We perform atomistic simulations of crack propagation for three different Li compositions ($x = 0.5, 1.0, 1.5$ in $\mathrm{Li}_x\mathrm{Si}$) and three discharged samples ($x = 0.5$ discharged from $x_\infty = 1.0, 1.5$ and $x = 1.0$ discharged from $x_\infty = 1.5$ in $\mathrm{Li}_x\mathrm{Si}$). We measure similar fracture energies for all as quenched samples, with void nucleation and coalescence observed to be the primary mechanism of crack growth. With increasing Li content, the plastic flow stress decreases but the material becomes more susceptible to void nucleation and growth.

Because of the similarities between the fracture mechanism of $\mathrm{Li}_x\mathrm{Si}$ and ductile fracture, Gurson's model is used to help interpret the simulation results. Quantitative agreement between the trends predicted by Gurson's model based fracture simulations and MD simulations of cracks in $\mathrm{Li}_x\mathrm{Si}$ is demonstrated. Gurson-type models predict that the fracture energy scales with the yield stress and void spacing D ($J_I = \alpha\sigma_y D$, $\alpha \simeq 1$). In all tested cases the nucleated voids spaced within few nanometers of the crack tip, which describes the low fracture energy of $\mathrm{Li}_x\mathrm{Si}$ as it scales with spacing of the voids. Thus $\mathrm{Li}_x\mathrm{Si}$ fracture brittle like despite its ability to flow plastically. Generalized plane strain equi-biaxial expansion simulations of uncracked samples are performed to provide complementary information on the void nucleation and growth. We then investigate the effects of discharging on fracture, and show that the increased structural disorder generated by discharging decreases the flow stresses but facilitates void nucleation and growth. However, in all tested samples the fracture toughness and fracture energy is increased by discharging, indicating that the flow and fracture of lithiated silicon depends on the history of charging/discharging.

In this work we first present and analyze experimental data on fracture of lithiated silicon. Next, after reviewing theoretical background on ductile fracture, in Sec. 3.3 we set up and analyze plain strain K_I fracture tests. In the molecular dynamics K_I fracture tests, we observe plastic flow around the crack tip followed by void nucleation and growth, leading to crack extension, with the development of an R-curve over 100s of Angstroms of crack growth. As the mechanism of crack growth is similar to ductile fracture mechanism, we analyze the ability of ductile fracture theories to describe the fracture properties of Li_xSi in Sec. 3.4. Specifically, to complete the generalized plane strain K_I crack propagation simulations, we perform simulations of generalized plane strain expansion in Sec. 3.4.2, which corroborates the evolution of voids observed ahead of the crack tip as a function of alloy composition. We then study materials that have been discharged from higher composition x_∞ to lower x in Section 3.5. Previously, we have proposed a theory for plasticity in amorphous lithiated silicon which accounts for the history of loading and charging/discharging, and leads to a history dependence of the flow stress in terms of excess internal energy relative to the initial relaxed material at the same composition (as-quenched material) [Khosrownejad and Curtin(2016)]. In the plane strain tests of discharged materials, we find decreasing flow stress and increasing of the spacing of the nucleated voids with increasing degree of discharging, indicating not only the yield stress is a function of charging/discharging history, the fracture toughness in lithiated silicon is also a function of the charging/discharging state of the material as well as the loading rates.

3.1 Experimental studies of fracture in Lithiated Silicon

Here, we present two recent semi-quantitative experimental fracture studies performed on lithiated silicon, i.e., work by Pharr et. al [Pharr et al.(2013)Pharr, Suo, and Vlassak] and more recent study by Wang et. al [Wang et al.(2015)Wang, Fan, Wang, Wang, Tao, Yang, Liu, Chew, Mao, Zhu, et al.]. Neither of these studies is a direct measurement of fracture properties, and these works mainly endeavor to relate indirect test results to fracture properties of lithiated silicon in batteries.

In the first study, the fracture energy of lithiated silicon thin-film electrodes has been measured in-situ and reported as a function of lithium concentration [Pharr et al.(2013)Pharr, Suo, and Vlassak]. Many electrodes are put in an electrochemical cell and charged and discharged at the same time. At a set of discrete concentration steps, one of the films is disconnected and analyzed to measure the sizes of any cracks formed at the selected composition. If the length of the crack, Δa, is much longer than the film thickness h_f, the fracture energy should not depend on the size of initial crack and the energy release rate G is computed as [Nakamura and Kamath(1992)]

$$G = \left[\frac{\sigma}{3\tau_0} + g\left(\frac{E_f}{E_s}\right)\right]\frac{\sigma h_f}{E_f}. \tag{3.1}$$

Here, g is a function of the elastic mismatch between the film and the substrate, E_f and E_s are the biaxial modulus of the film and substrate, respectively, σ is the biaxial stress in the film, and τ_0 is the interfacial sliding strength between the film and substrate. As the authors did

Table 1 – Calculated range of fracture energies corresponding to a range of Li concentration using in-situ measurement methods by Pharr. et. al. [Pharr et al.(2013)Pharr, Suo, and Vlassak].

x in Li_xSi Low concentration	$\Gamma (J/m^2)$	x in Li_xSi High Concentration	$\Gamma (J/m^2)$
0.33	14.9	3.0–3.2	7.6–9.4
0.73	6.6	2.8–3.0	2.4–5.6
0.86	7.0	2.4–2.6	6.5–7.5
1.0	5.4	2.4–2.7	5.0–5.2

not have a good estimate of the interfacial sliding strength, they calculated an upper bound for the fracture energy by assuming perfect interface at each concentration. In this analysis the substrate is assumed to be elastic and thus it does not consider the energy dissipation in the substrate due to the plasticity of the Copper substrate, which could be considerable since Copper yields at about 100 MPa, much lower than the measured yield stresses of lithiated silicon of $500 - 1000\,MPa$. The measured fracture energies for in-situ lithiated silicon are reported in Table 1. There are two important observations in this experimental study. First the values of fracture energies are relatively small for a material with the ability of accommodating large plastic strains. Second, the value of fracture energy remains almost constant from low to high lithium contents.

Wang et. al. [Wang et al.(2015)Wang, Fan, Wang, Wang, Tao, Yang, Liu, Chew, Mao, Zhu, et al.] performed an indentation study on the damage tolerance of lithiated silicon. To measure the fracture toughness, amorphous Li_xSi thin-film electrodes were indented with a cube corner indenter tip. After unloading of the indenter, the indentation area was imaged using a scanning electron microscope (SEM). The material exhibited distinct cracking behaviors under different indentation loads, including (i) no cracking for loads less than 93 mN, (ii) indent corner cracking, and (iii) massive cracking. Observing these behaviors strongly depends on the concentration of lithium. Under a small load of 3.92 mN, residual plastic deformation was observed without apparent cracking for all lithium concentrations (Fig. 1a). By increasing the load to 9.8 mN, three radial cracks emanated from the sharp corners of the indent (Fig. 1b) for $Li_{0.87}Si$. Further increase in the indentation load to 29.4 mN resulted in massive cracking around the indent (Fig. 1c) for the same composition, $Li_{0.87}Si$. Similar cracking behaviors were observed for low Li concentrations from $x = 0$ to $x = 1.09$. In Fig. 1g the black line separates the load range bellow which residual plastic deformation is observed and above that indent corner cracking happens. The blue curve shows the boundary between the corner cracking loads and massive cracking. As the lithium concentration was increased to above $x = 1.56$, no cracking was observed from indents for a wide range of indentation loads [Wang et al.(2015)Wang, Fan, Wang, Wang, Tao, Yang, Liu, Chew, Mao, Zhu, et al.]. These results are in contradiction with the experiments performed by Phaar et. al.. Specifically, for high lithium concentration, the indentation method claims a high damage tolerance while the work of Pharr et. al. [Pharr et al.(2013)Pharr, Suo, and Vlassak] reported a finite and concentration-independent fracture energy over the same range of compositions. Apparently, the fracture energy levels for low lithium concentration reported in Wang et. al. is in the same range of the values reported by Pharr et. al. and very low for a material with high ductility. Furthermore, fracture energy and fracture toughness is increasing by concentration for $x < 1.56$ in $\mathrm{Li}_x\mathrm{Si}$, unlike the reported values in Phaar et. al which shows a decrease in the fracture energy as a function of lithium content.

In view of the many studies and observations about the reliability of the indentation technique for fracture toughness testing, one must interpret the indentation fracture toughness tests with extreme care [Quinn and Bradt(2007)]. The main reason is a lack of a definite analytical solution for the stress intensity factor under the indenter. Understanding the toughening mechanisms and assessing the validity of the indentation testing method in ceramics has been a challenge as reported in different scientific studies [Wang et al.(2004)Wang, Padture, and Tanaka, Sheldon and Curtin(2004)]. Furthermore, the experimental study of Wang et. al. [Wang et al.(2015)Wang, Fan, Wang, Wang, Tao, Yang, Liu, Chew, Mao, Zhu, et al.] is done ex-situ, which implies that the possible effects of electrochemical reactions, as well as rate effects, have not been captured.

3.2 Theoretical background on crack growth in ductile fracture

Irwin suggested that the criterion for crack advancing in an elasto-plastic solid is that the energy release rate G equals the crack growth resistance Γ_R

$$G = \Gamma_R(\Delta a) \tag{3.2}$$

Crack resistance is a function of the amount of crack growth Δa. $\Gamma_R(\Delta a)$ usually increases with increasing Δa due to an increase in the size of plastic zone around the crack (see Fig. 2). In mode I plane strain conditions, the relation between energy release rate and stress intensity factor is

$$G = \frac{(1-\nu^2)K^2}{E} \tag{3.3}$$

which let us reformulate relation 3.2 in the form of applied stress intensity factor K and resistance K_R.

$$K = K_R(\Delta a) \qquad \text{with} \qquad K_R = \sqrt{E\Gamma_R/(1-\nu^2)} \tag{3.4}$$

One purpose of our study is to systematically evaluate the applicability of ductile fracture models to Li-Si systems. The nature of these models is outlined in Fig. 2. As the crack grows, the cells near the newly formed crack surface undergo a biaxial stress state which activate instabilities in the nanostructure of amorphous material and form nano-sized voids. Then a significant void growth takes place, while cells further away exhibit little or no void activity. The length of the cell D is interpreted as the mean spacing between the voids nucleated

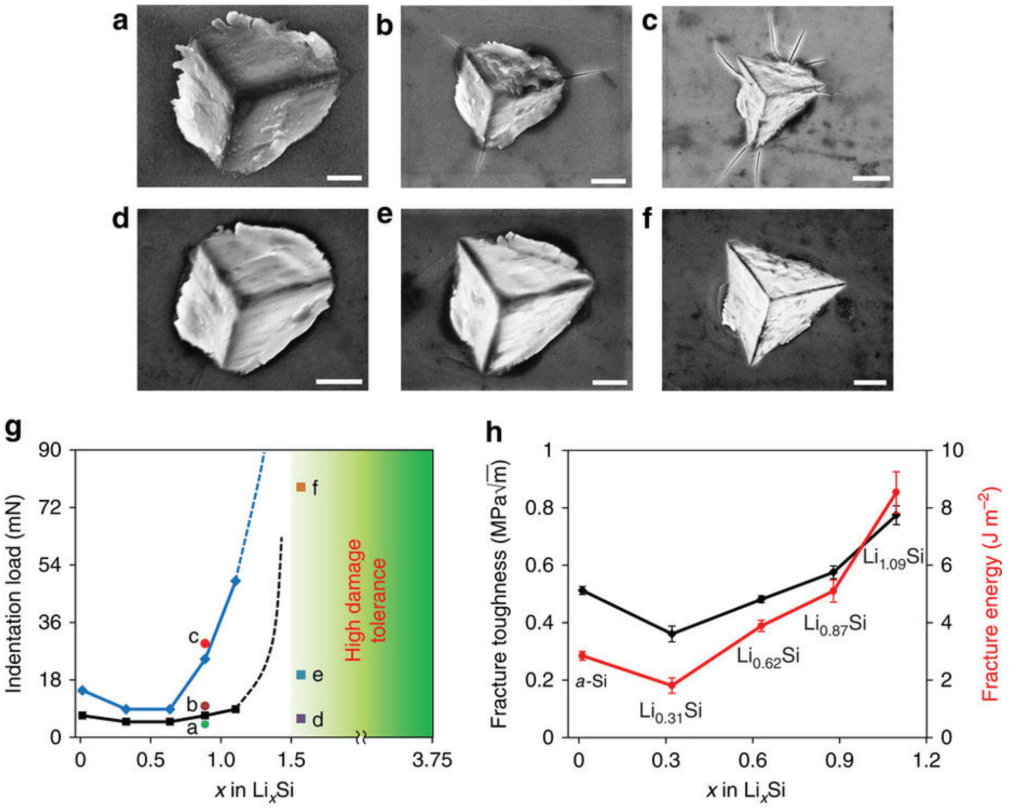

Figure 1 – SEM images of residual indents for a lithiated electrode of $Li_{0.87}Si$, showing (a) no cracking, (b) radial cracking and (c) massive cracking subjected to different applied indentation loads. (d–f) SEM images of residual indents for a lithiated Si electrode of $Li_{1.56}Si$ showing no cracking subjected to the same loads (g) The indentation loads (symbols) applied to the lithiated electrodes with different Li contents. The blue solid curve represents the upper load limit above which massive cracking occurred and the black solid curve the lower limit below which no crack was induced. (h) Fracture toughness of radial cracks after indentation in thin film and fracture energy of lithiated Si as a function of Li concentration [Wang et al.(2015)Wang, Fan, Wang, Wang, Tao, Yang, Liu, Chew, Mao, Zhu, et al.].

from large inclusions in metals. However, in amorphous structures such as Li$_x$Si , there is no inclusion apriori and local instabilities in the amorphous structure act as seed sites for voids. We will discuss the application of such model to the understanding of our MD simulation of fracture in Li$_x$Si systems in the rest of this chapter. For fracture in ductile metals, Tvergaard and Hutchinson [Tvergaard and Hutchinson(1992)] proposed a nondimensional expression for the function $\Gamma_R(\Delta a)$.

$$\Gamma_R = \Gamma_0 F\left[\Delta a/D, N, \sigma_0/E, \nu, \text{Fracture prop.}\right] \tag{3.5}$$

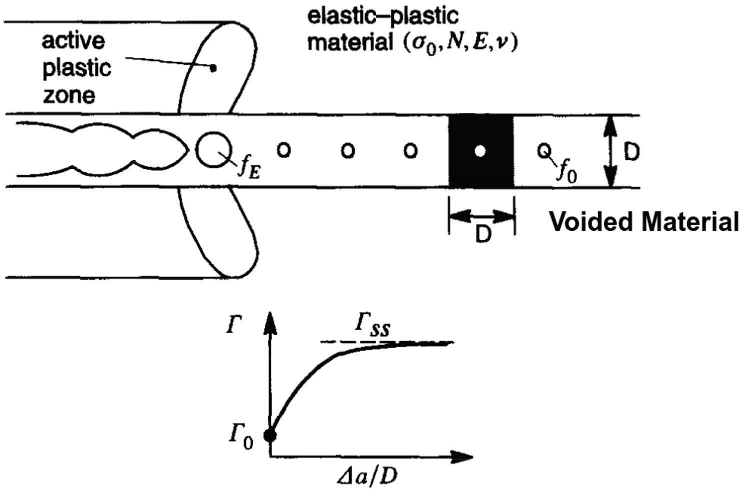

Figure 2 – Schematic illustration of within fracture process zone during crack growth. The background plastic dissipation is not drawn in the figure. The length scale D indicates the characteristic distance between voids [Xia and Shih(1995a)].

Here, D is the width of the fracture process zone (FPZ) around the crack tip. E, N and ν are the material parameters in the power-law elasto-plastic constitutive model

$$\varepsilon = \begin{cases} \dfrac{\sigma}{E} & \text{,if} \quad \sigma < \sigma_0 \\ \dfrac{\sigma_0}{E}\left(\dfrac{\sigma}{\sigma_0}\right)^{1/N} & \text{,if} \quad \sigma \geq \sigma_0 \end{cases} \tag{3.6}$$

that is widely used in fracture models of plastically-deforming materials.

To describe the resistance function F in Eq. 3.5 for the fracture model depicted in Fig. 2, we use the dilatational plasticity model of Gurson, Tvergaard and Needleman (GTN model) [Gurson(1977)]. The GTN model describes the progressive damage, via void expansion, that leads to material softening and then the loss of stress–carrying capacity starting at a specific micromechanical condition. The GTN model has a firm micromechanical basis and has been validated by, and used in, finite element simulations [Needleman et al.(1992)Needleman, Tvergaard, and Hutchinson]. The GTN theory consists of a flow law and an evolution equation for the void volume fraction f, treated as an internal variable. Free volume fraction has been also utilized in amorphous metal theories to describe the plastic behavior [Spaepen(1977)]. The yield surface in the GTN model was derived from approximate plastic solutions for a single cell containing a centered spherical void [Needleman et al.(1992)Needleman, Tvergaard, and Hutchinson] and it has the form

$$\Phi(\sigma_e,\sigma_h,\sigma_0,f) = \left(\frac{\sigma_e}{\sigma_0}\right)^2 + 2q_1 f \cosh\left(\frac{3q_2\sigma_h}{2\sigma_0}\right) - 1 - (q_1 f)^2 = 0 \tag{3.7}$$

with σ_e being the von-Mises equivalent stress and σ_h the volumetric stress. The quantities q_1 and q_2 are material–dependent parameters. The simplest form of evolution equation for the void volume fraction f is a function of volumetric plastic strain rate,

$$\dot{f} = (1-f)\dot{\varepsilon}_{ii}^{p} \tag{3.8}$$

Eq. 3.8 is valid for $f < f_E$ where f_E is a critical void volume fraction at which the material loses stress–carrying capacity due to rapid void growth and void coalescence. Using the Gurson model of fracture, Eq. 3.5 can be stated as

$$\Gamma_R = \Gamma_0 F\left[\Delta a/D, N, \sigma_0/E, \nu, f_0, f_E, q_1, q_2\right] \tag{3.9}$$

In this work, we will use the results of parametric studies performed using the above model [Pardoen and Hutchinson(2003), Xia and Shih(1995a), Xia and Shih(1995b)] to examine the ductile fracture assumption on the fracture bahavior of $\mathrm{Li}_x\mathrm{Si}$.

3.3 Atomistic simulations of fracture in $\mathrm{Li}_x\mathrm{Si}$

Given the difficulty and inconsistency of experimental studies on fracture of lithiated silicon in the literature, the need for a mechanistic understanding of the fracture behavior of $\mathrm{Li}_x\mathrm{Si}$ motivates the application of systematic molecular dynamics simulations to study fracture in lithiated silicon. In this section, we explain the details of, results from, and mechanisms occurring in, such simulations.

3.3.1 Atomistic simulation of fracture: sample preparation and methods

To model fracture in the atomistic simulation, we prepare amorphous samples in MD by melting a sample of the desired $\mathrm{Li}_x\mathrm{Si}$ composition and then quenching it with a rate of $2000°K/ns$ from $2500°K$ to $1500°K$, with rate of $500°K/ns$ to $700°K$ and finally with a rate of $2000°K/ns$ from $1°K$. This procedure is chosen to slow down the quench rate above glass transition temperature that the structure forms while keeping it computationally tractable. We used the second nearest neighbour MEAM inter atomic potential proposed by Cui et. al. [Cui et al.(2012a)Cui, Gao, Cui, and Qu] in all our simulations. In Appendix A we discussed in details the preparation and properties and amorphous material samples.

To model fracture, we use a simulation cell of dimensions $l_x = 960$Å, $l_y = 20$Å, $l_z = 760$Å. The sample is periodic along the line of the crack in the $y-$ direction to model generalized plane strain conditions. To limit the computational time, smaller samples are quenched and then duplicated in a grid of $8 \times 1 \times 7 (x \times y \times z)$ to produce the larger fracture sample. The chosen sample size in the x and z directions is large enough to accommodate the full plastic zone around the crack tip inside the sample and away from the boundaries that occur over loading sufficient for hundreds of Angstroms of crack growth. Thus, small-scale yielding remains valid over the full range of our study, allowing application of stress-intensity-controlled displacement boundary conditions (see below). Table 2 shows the mechanical properties of the sample

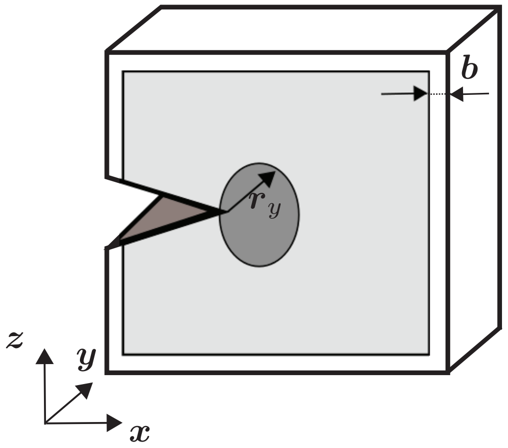

Figure 3 – geometry of specimen and important details of simulation method. At each time step all atoms are moved in conformance with Eq 3.10. Atoms in the gray region are relaxed in NVT ensemble at $T = 1°K$. Atoms in the white region are fixed to keep the loading. The thickness of boundary layers in our simulations is $b = 20Å$

and the estimated size of plastic zone for plane strain $r_y = (K_I/\sigma_0)^2/3\pi$ at $K = 1MPa\sqrt{m}$ for different compositions of lithium. Figure 3 shows the geometry of specimen and important details of simulation cell.

To model fracture, we apply displacement boundary conditions corresponding to the mode-I K field on the boundaries of the MD cell according to equation:

$$\begin{aligned} du_x &= \frac{\Delta K_I}{G}\sqrt{\frac{r}{2\pi}}cos(\theta/2)\left[1-cos^2(\theta/2)\right] \\ du_y &= \frac{\Delta K_I}{G}\sqrt{\frac{r}{2\pi}}sin(\theta/2)\left[1-cos^2(\theta/2)\right] \end{aligned} \tag{3.10}$$

with r being the distance from the crack tip and θ the angle with the x axis in Fig. 3. The initial crack tip is placed at $x = 130Å$, $z = l_z/2$. Loading is accomplished by increasing K_I in increments of $\Delta K = 0.01MPa\sqrt{m}$. For each loading step, all atoms are first moved with an affine transformation conforming to equation 3.10. Then the boundary atoms (white area in Fig. 3) are fixed while all interior atoms are relaxed using molecular dynamics at $T = 1°K$. Relaxation is performed for a sufficient time to achieve near-equilibrium, i.e. convergence of the total energy. Here, convergence is achieved if the change in total sample energy between subsequent time steps is less than $1e-6\,eV/$atom in average. If the crack grows during an increment of loading, the boundary conditions are updated according to the position of the crack as the crack grows. Specifically, we find the new crack tip position using coordination analysis to find newly-created surface in the structure, and find the furthest distance along the crack direction of such new surface. The displacement boundary conditions are then updated corresponding to the current total applied K_I and the new crack tip position. The method of finding the new crack tip is accurate to within $\pm 10Å$, and errors do not accumulate with crack growth; the boundary conditions are thus always sufficiently accurate with respect to the true

Table 2 – Plane strain plastic zone size for Li$_x$Si with different compositions.

x in Li$_x$Si	$E(GPa)$	ν	$\sigma_y(GPa)$	r_y(Å) $(K = 1MPa\sqrt{m})$
0.5	90.38	0.28	6.19	27.9
1.0	66.76	0.33	4.26	58.4
1.5	51.37	0.33	3.21	102.9

crack tip position.

For later analysis, we need the mechanical properties of the as-prepared samples. We perform uniaxial tension test on the samples and fit the material parameters in the constitutive model of Eq. 3.6 to capture the main features. Figure 4 shows the simulated stress-strain curves and the fits to the constitutive model. We aim to use a single set of parameters across all materials, and find acceptable results using $N = 0.1$ and $\sigma_0 = 0.9\sigma_f$, where σ_f is the average value of stress over the strain range $0.15 < \epsilon < 0.2$. The constitutive model does not capture the initial softening of the material for small plastic strains but does capture the steady state plastic behavior of the MD simulations reasonably well.

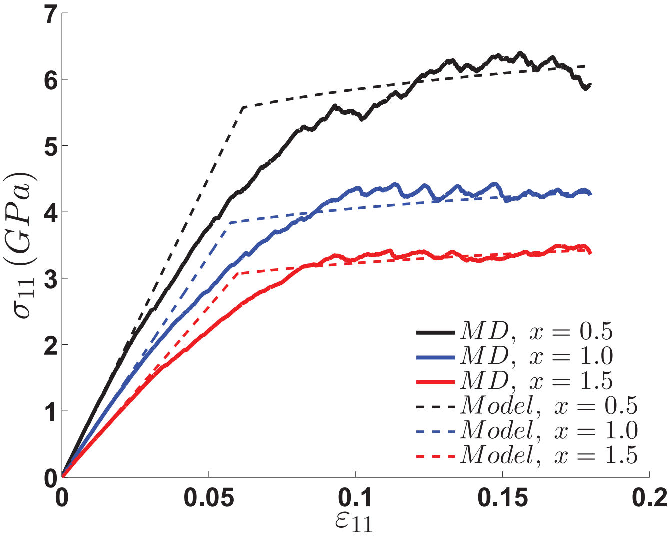

Figure 4 – Comparison between model of Eq. 3.6 and MD data for the uniaxial tension test with parameters $\sigma_0 = 0.9\sigma_f$ and $N = 0.1$

3.3.2 Clustering phenomenon for high lithium concentration

In the process of preparing of samples with high lithium concentrations, i.e $x \geq 2.0$, atoms of the same kind aggregate and form lithium rich and silicon rich structures over few nm size scale. This phenomenon has been observed in samples prepared with the current MEAM potential [Cui et al.(2012a)Cui, Gao, Cui, and Qu] and also with a recently-developed ReaxFF potential [Group of Prof. Adri van Duin, private communication]. Clustering dramatically reduces the fracture toughness at these high concentrations. Figure 5 shows the strain localization in a specimen with $x = 3.5$ after the crack has propagated unstably in a cleavage-like event.

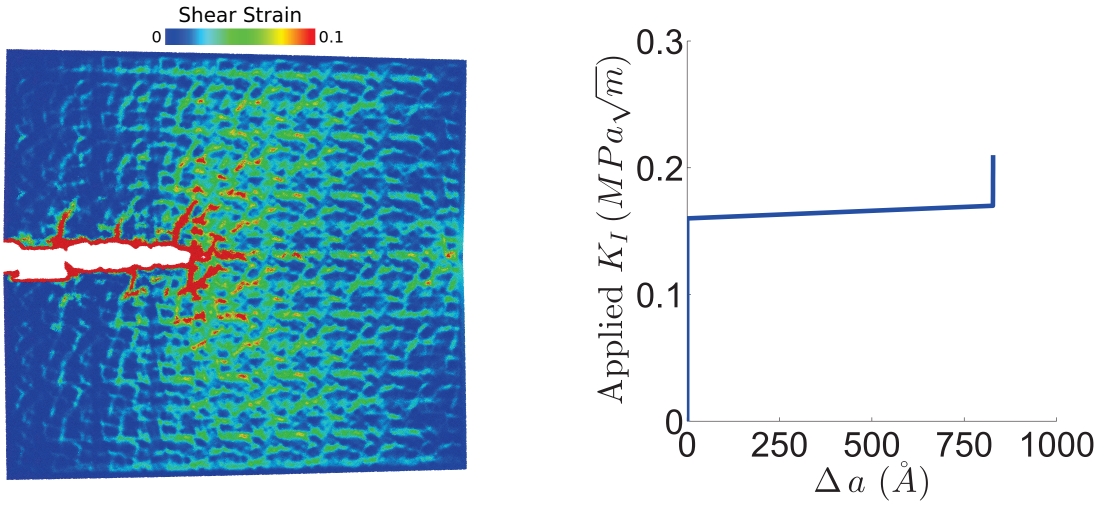

(a) Effective shear strain in the sample

(b) Fracture resistance curve.

Figure 5 – a) Strain localization during cleavage-like crack propagation in high Li sample. Fracture happens in very low K_I values in the form of rupture as the result of stress concentration around formed clusters.

If clustering happens in the real materials, which has not been observed experimentally to our knowledge, the size of the clusters will presumably be a function of temperature and charging/discharging history. Thus fracture toughness and fracture energy would be a function of size and composition of the clusters. Study of cluster formation is beyond the scope of current work, and may be an artifact. Thus we only study concentrations below $x = 2.0$, where no clustering is observed after quenching during the sample preparation process. Specifically, we study three concentrations $x = 0.5, 1.0, 1.5$ in the following fracture simulations.

3.3.3 Fracture toughness atomistic simulations results of as prepared samples

In this section, we present the results of fracture toughness simulations for three different compositions, i.e, $x = 0.5, 1.0, 1.5$ in $\mathrm{Li}_x\mathrm{Si}$. We measure the stress intensity factor K_I versus crack length Δa, which is known as Resistance curve, or R-curve, in fracture mechanics. To address the randomness in the structure of the material, we simulated several samples for each composition.

Figure 6 shows the crack growth versus applied K-field for the three different compositions. A full R-curve provides three important quantities: (i) the initiation stress intensity factor (toughness) K_{IC}; (ii) the R-curve slope dK/da and its evolution with crack length; and (iii) the steady-state stress intensity factor K_{ss} which may or may not be achieved at sufficiently large

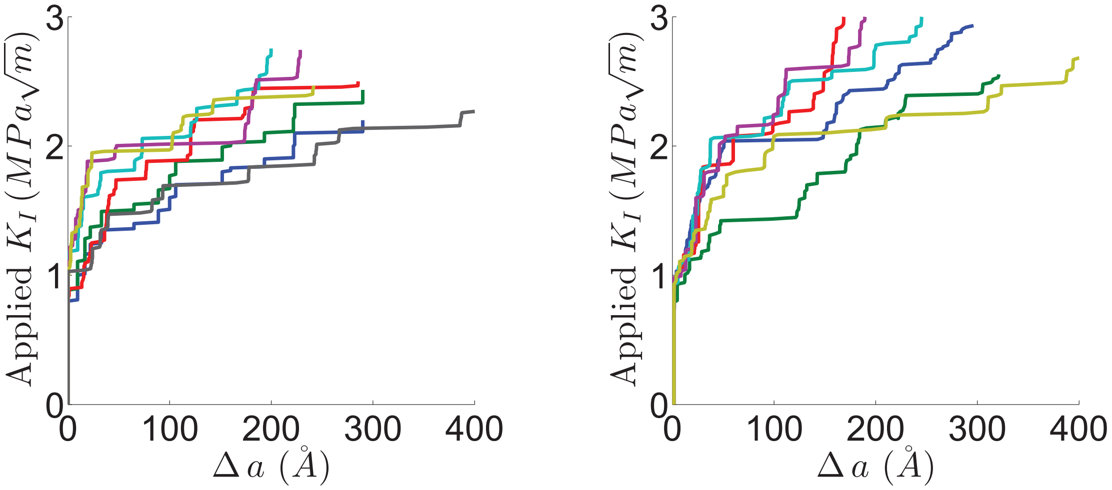

(a) $x = 0.5$ **(b)** $x = 1.0$

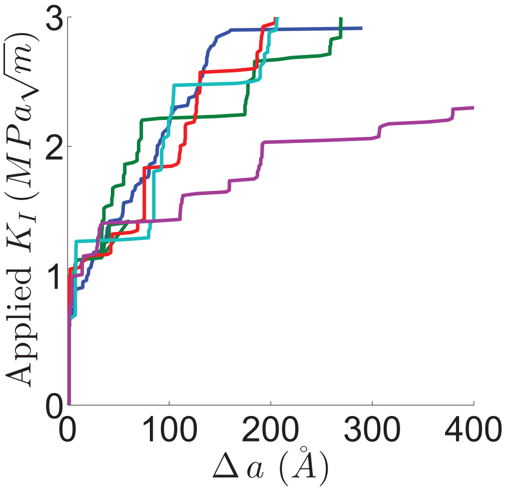

(c) $x = 1.5$

Figure 6 – R-curve obtained using MD simulations for three different compositions. For each composition, eight samples have been simulated to address the randomness of the structure.

crack growth [Hutchinson(1983)]. In the engineering context, K_{ss} is defined at a particular length of crack growth. Here, due to size limitation, we have simulated crack growth out to maximum $\Delta a \simeq 200$Å in all samples. Hence, we compare of K_{IC} and $K(\Delta a = 200\text{Å})$ as a measure of the toughness evolution.

Table 3 presents the initiation fracture toughness and fracture toughness for a grown crack $K_I(\Delta a = 200\text{Å})$. Crack initiation for silicon-rich structures happens at higher stress intensity and initiation fracture toughness decreases with lithium composition. However, silicon rich compositions show lower resistance slope. We observe that the resistance slope dK/da for all compositions is decreasing with increasing crack growth. To quantify the large distance crack growth and dK/da we compare the value of fracture toughness for $\Delta a = 200$Å. The difference

Table 3 – K_{IC} and K_I values for fracture tests in $\mathrm{Li}_x\mathrm{Si}$ with different as-quenched compositions.

x in $\mathrm{Li}_x\mathrm{Si}$	K_{IC}	$K_I(\Delta a = 200\text{Å})$
0.5	1.0086 ± 0.1129	2.3380 ± 0.3073
1.0	0.8869 ± 0.1096	2.5854 ± 0.3969
1.5	0.7839 ± 0.1789	2.7253 ± 0.3200

between the resistance becomes smaller among different compositions as shown in Tab. 3. In other words, for $x = 0.5$ material R-curve starts at high fracture toughness, but the toughness increases slower than $x = 1.5$ and might have smaller or equal steady state toughness.

Rice proved that a steady state plastic zone size and fracture toughness exist with the assumption of small scale yielding, and achievement of a maximum plastic strain in the crack-tip to advance the crack, as criteria for crack growth [Rice(1968)]. In cohesive zone based models the steady-state fracture toughness is attained in relatively smaller $\Delta a/D \simeq 5$ [Tvergaard and Hutchinson(1992)]. However, in the calculation of R-curve using Gurson model, the R-curves seems not to saturate as fast as cohesive zone models[Xia and Shih(1995a)]. Here, due to size limitations of molecular dynamics simulations, we were not able to continue the simulation until we get stable crack growth. We have tracked the crack tip to $\Delta a \simeq 200$Å. Value of D is extracted and presented in Tab. 4, which shows that we have tracked the crack tip up to $\Delta a/D > 20$ and we did not observed saturated R-curves. Thus, Gurson type models are more suitable to rationalize this observation in MD simulation of crack growth.

3.3.4 Fracture mechanism in $\mathrm{Li}_x\mathrm{Si}$

To understand the fracture process, we examined the mechanisms of crack growth occurring in the MD simulations. The continuous advance of the crack tip shown in Fig. 6 occurs due to void nucleation and coalescence. The bigger jumps in the crack length seen in the R-curves of Fig. 6 are associated with void formation, growth, and coalescence. As shown in Figure 7, the failure process ahead of the growing crack involves several interacting processes: nucleation of nanovoids, subsequent growth of the larger nanovoids, localization of plastic flow between the enlarged voids, and tearing of the ligaments between enlarged voids. This overall fracture process occurs in a confined zone – the fracture process zone (FPZ) – ahead of the crack. The same general process occurs for all three compositions. However, void size and spacing increase with increasing Li composition, which is also associated with lower plastic flow stress with increasing Li composition. Thus the characteristic size of the FPZ is determined by the atomic structure and material flow behavior.

To better understand the conditions under which voids are created and grow in these amorphous materials, we performed equi-biaxial plane strain tests for $\mathrm{Li}_x\mathrm{Si}$ samples at different compositions. The strain state ahead of a generalized plane strain mode I crack in an isotropic material is approximately equi-biaxial [Faleskog et al.(1998)Faleskog, Gao, and Shih]. Hence, we performed tests with equally biaxial strain $\varepsilon_x = \varepsilon_z = \varepsilon$ applied in the x and z directions and periodic boundary conditions in y direction (with reference to the same coordinate system of fracture simulation shown in Fig. 3) to simulate the generalized plane strain condition under which voids appear in the full crack simulations. The size of each sample is $40 \times 20 \times 40(\text{Å})(x \times y \times z)$, which is in big enough to accommodate the nanomechanical features has been observed in front of the crack. We applied periodic boundary condition to the cell in all directions. The results of these simulations presented in detail later. Now, we want to focus on measuring void nucleation and its evolution in the material.

To quantify the voids within the structure of the amorphous system, we used a coordination analysis. Selecting one atom at a time, we counted the number of atoms around the chosen atom within a cut-off radius r_c and scaled the number of neighbors with strain. This process is repeated for every atom in the sample. Fig. 8 shows the logarithmic histogram of rescaled number of neighbours $N_{\text{neighbours}}$. Initially, in the amorphous structure, there is a statistical distribution of the number of neighbors within r_c of an atom. During straining of the structure, those atoms near a void will have fewer neighbors, leading to the emergence of a larger tail in the lower portion of the distribution. Our analysis shows that void creation starts at very small strains of about $\varepsilon = 0.03$, comparable to the onset of non-linear deformation in the uniaxial stress-strain curves. Thus, although there are no pre-existing voids in the initial structure, voids start to form early in the deformation. These voids can, for the purposes of fracture processes, be considered as pre-existing in the sense that they exist well prior to the point of extensive void growth and coalescence. In the equi-baixial specimens, the voids grow and new voids nucleate with increasing strain; our analysis cannot separate out these two processes.

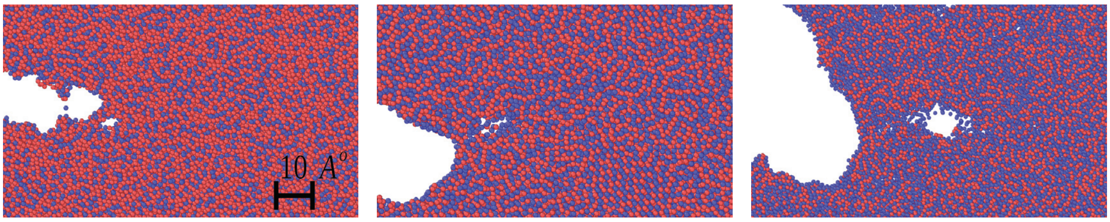

(a) $x = 0.5,\ K = 2.08$ **(b)** $x = 1.0,\ K = 1.94$ **(c)** $x = 1.5,\ K = 2.008$

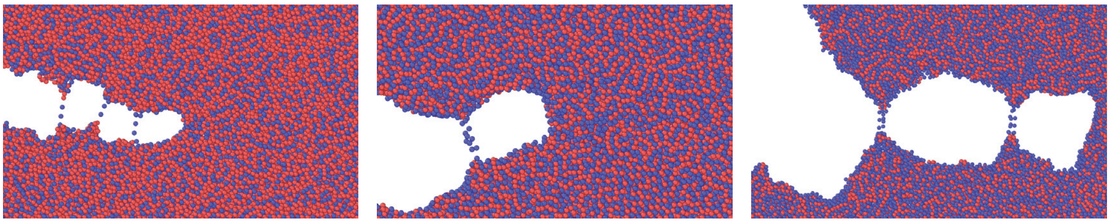

(d) $x = 0.5,\ K = 2.10$ **(e)** $x = 1.0,\ K = 1.98$ **(f)** $x = 1.5,\ K = 2.10$

Figure 7 – Snapshots of fracture process in different samples which shows the creation of voids, the growth and coalescence in front of crack tip. The scale is the same for all snapshots and is shown in the left upper picture. The spacing of void in front of the crack is reproducible over multiple samples and with crack growth.

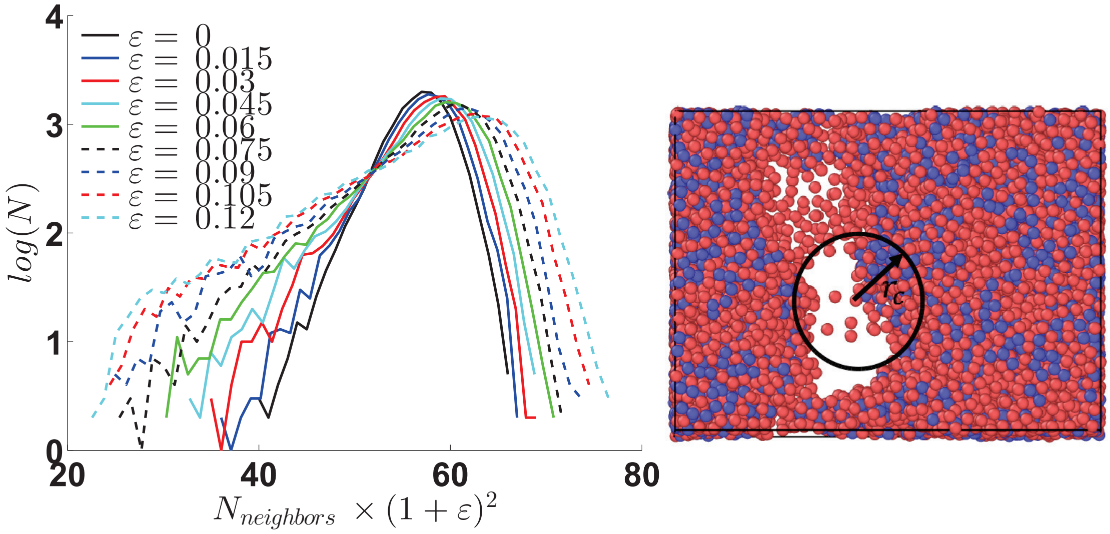

(a)

(b)

Figure 8 – Quantification of void nucleation and growth in $\mathrm{Li}_x\mathrm{Si}$ by coordination analysis. a) The logarithmic histogram of number of atoms with a specific strain normalized number of neighbours in a shell with cut-off radius $r_c = 6$Å b)A snapshot of specimen under equally uni-axial strain with $x = 0.5$ at $\varepsilon = 0.2$

The nano-mechanisms of fracture in simulated samples of $\mathrm{Li}_x\mathrm{Si}$ alloys is similar to the ductile fracture behavior observed in engineering metals at much larger size scales. Void nucleation and growth are the essential micro-mechanism of the Gurson-type models for fracture in ductile materials. We will thus further investigate the application of ductile fracture models to understand the MD fracture simulation of $\mathrm{Li}_x\mathrm{Si}$ in the next section.

3.4 Ductile fracture model for $\mathrm{Li}_x\mathrm{Si}$

As shown in the previous section, the nano-mechanism of fracture in $\mathrm{Li}_x\mathrm{Si}$ suggests a ductile fracture process. Here, we examine the results of MD simulations to assess whether or not $\mathrm{Li}_x\mathrm{Si}$ exhibits other fundamental aspects of ductile fracture. Establishing a relation between the fracture of $\mathrm{Li}_x\mathrm{Si}$ and ductile fracture theories could also permit the wider use of the established ductile fracture theories to fracture in amorphous alloys in general, beyond the $\mathrm{Li}_x\mathrm{Si}$ system studied here.

3.4.1 Fundamental length scale in the fracture of $\mathrm{Li}_x\mathrm{Si}$

In ductile fracture models, the initial fracture energy can be expressed as [Faleskog et al.(1998)Faleskog, Gao, and Shih, Pardoen and Hutchinson(2003)]

$$J_{IC} = \alpha D \sigma_0 \tag{3.11}$$

Table 4 – Measured values of the spacing of the voids, D, and calculated scaling factor α in MD simulation for different as-quenched samples.

x in $\mathrm{Li}_x\mathrm{Si}$	D(Å)	$J_{IC}(J/m^2)$	$\alpha = J_{IC}/\sigma_0 D$
0.5	6.1 ± 1.1 (Å)	$11.214^{+2.65}_{-2.37}$	2.96 ± 1.2
1.0	10.7 ± 1.3 (Å)	$11.895^{+3.14}_{-2.77}$	2.60 ± 0.9
1.5	14.9 ± 1.6 (Å)	$11.888^{+6.06}_{-4.81}$	2.54 ± 1.3

where σ_0 is the yield stress of the material, D is a length of the fracture process zone, and α is a coefficient of the order one that depends on the elasto-plastic parameters of the material as well as some fracture properties. To calculate α, we measure the length scale of the fracture process zone D in the simulations. In calibrating experimental data, D is usually considered as the distance between pre-existing voids. However, $\mathrm{Li}_x\mathrm{Si}$ does not have pre-existing voids in the unloaded state, and the evolving void fraction can be distributed through the system, as shown in Fig. 7. Here, we take D as the distance between any distinguishable nucleated void and the crack tip, as observed during the crack growth simulation. Table 4 shows the mean value and standard deviation of measured value of D for all compositions taken from all samples simulated for that composition.

Using the measured D, Tab. 4 then also shows the value of α computed for different compositions. The value of α remains constant independent of composition. Pardoen and Hutchinson [Pardoen and Hutchinson(2003)] used a Gurson model to perform a parametric study of J_{IC}, which is defined as the energy of fracture for the first coalescence event. They showed that the effect of σ_0/E on α is negligible. If N and f_0 do not change for different compositions, then their results would imply a constant α for our fracture tests. Strain hardening exponent N for these material remain constant as a function of composition as seen in Fig. 4. The observation of constant α suggests that f_0 is weakly dependent on composition, and so in the next section we will attempt to estimate f_0 by applying the Gurson model to the biaxial unit cells.

It worth noting that, calculations done with large scale yielding assumption and Gurson model for crack propagation show that the stress state does not change in front of the crack during crack growth [Xia and Shih(1995a)]. In other words, if the fracture process zone is well-developed, then the radius of the blunted crack remains constant, which implies the existence of a constant stress state in front of the crack. Formation of voids is a function of stress state, thus the value D is not a function of Δa after the process zone is in the steady state form. Looking at the crack opening distance for all MD simulation samples show that the crack opening distance stabilizes in the initial phases of the crack growth. Thus the values for D is measured independent of the state of the crack growth.

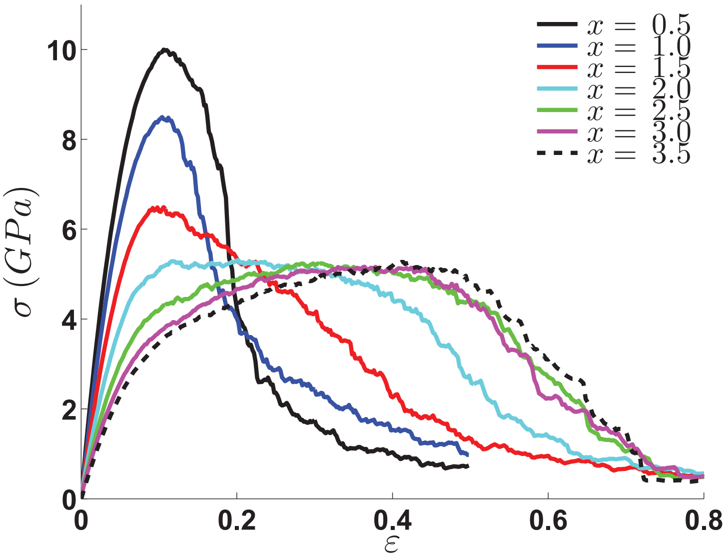

Figure 9 – Stress-strain curves for generalized equi-biaxial plane strain expansion tests. Each line shows the average stress value for 8 randomly generated samples.

3.4.2 Cell model for fracture analysis of Li$_x$Si

Micro-mechanical assumption for the fracture mechanism enables us to use well-established models to make predictions on the fracture of Li$_x$Si . Specifically, Gurson Tvergaard Needleman (GTN) model[Gurson(1977)] has been widely used to model nucleation, growth, and coalescence of voids in materials with pre-existing voids. We are examining whether Gurson can also explain the equi-biaxial MD simulations. Then we find the value of f_0 in the material by fitting the stress-strain curves with proper Gurson model of the same boundary condition.

We set up generalized plane strain expansion simulations, as explained in Sec. 3.3.4, for a complete range of compositions. For as-processed materials studied in Tab 3, the equi-biaxial plane strain stress-strain curves are shown in Figure 9. Each curve shows the average stress of 8 randomly generated samples of the same size. Figure 9 shows the onset of plastic flow and then abrupt failure at a critical strain due to void nucleation and growth. Materials with increasing Li content show decreasing flow stresses, as already established, but also increasing failure strains.

We used equally biaxial boundary condition for the Gurson model. Strains are constrained in all three directions, similar to the atomistic simulated cells. Triaxiality evolves both in atomistic simulations and Gurson model. We took $q_2 = 0.65$ and $q_1 = 1$ in the yield function 3.7. The material is presented with the model 3.6. We did not use any nucleation term for the Gurson model and the void volume fraction growth is governed by Eq. 3.8. The details of solution method have been explained in the literature [Vadillo and Fernández-Sáez(2009)].

Figure 10 shows the results of our fitting of the Gurson model to the biaxial MD simulations at the three compositions, using the initial void volume fraction f_0 as the only parameter. We use two types of fitting procedure to find f_0, namely fitting the curve during the drop from the peak stress as a measure of how the cell destabilizes after reaching a maximum stress and fitting the peak stress itself. In Fig. 10a-c we fit the destabilization of stress after the peak value. The elastoplastic model 3.6 used in this analysis does not perfectly model the softening of the material in the early stage of plasticity $\varepsilon \lesssim 0.1$. So, we do not expect the Gurson model to match this strain range in the unit cell models, and so the fitting is aimed at capturing the stress evolution after the above mentioned strain range. The Gurson model is only valid up to the sharp drop in the stress-strain curve, at which point coalescence takes place (not included in this Gurson model). The obtained values for initial void volume fraction is shown in the figure. f_0 shows a decrease with composition for smaller compositions of lithium. Fig. 10d shows the ratio between the maximum stress and yield stress for molecular dynamics equi-biaxial tests along with the same quantity from GTN model with different initial void volume fraction f_0. This plot helps us to obtain the value of f_0 to have the same peak stress for the GTN model and MD simulations. The trend of change of f_0 obtained from the two method of fitting the GTN model to MD results is the same for two methods, however, the values are higher in the peak stress fitting method.

The small change in the value of f_0, observed for different compositions shown in Fig. 10, does not have a big effect on α [Pardoen and Hutchinson(2003)]. This is consistent with the results obtained here for f_0 with regard to constant α obtained in previous section. Furthermore, the bigger value for f_0 would give smaller resistance rate dK/da in Gurson model based fracture simulations [Xia and Shih(1995a)]. This is also consistent with the crack simulation results (Fig. 6), having smaller crack resistance rates for $x = 0.5$. So, considering the observed void nucleation, growth and coallecence nano-mechanism of fracture and reasonable agreement with GTN based fracture simulation predicted trends, we conclude that the ductile fracture model based on Gurson type mechanism of fracture can describe the fracture in Li$_x$Si during charging/discharging.

3.4.3 Work of fractureLi$_x$Si

In the previous section we used Gurson model to rationalize the fracture test results. In this section we examine whether we can extract more useful information from equi-biaxial generalized plane strain expansion simulations. The total work of fracture per unit area is divided into plastic dissipation in the plastic zone, the elastic energy and the work of fracture process. It is argued elsewhere [Tvergaard and Hutchinson(1992), Xia and Shih(1995a)] that the work of fracture process is dominant at crack growth initiation, Under this assumption the J_{IC} for the first growth increment equals the work of fracture process Γ_0.

$$\Gamma_0 = J_{IC} \quad , \quad F[\Delta a/D = 0, ...] = 1 \quad \text{in Eq. 3.9} \tag{3.12}$$

Extracting Γ_0 is valuable, because having the initiation fracture energy and parameters of Gurson model obtained by fitting a cell model in previous section, there will be no need to perform the full K_I fracture tests. This information could be used in a finite element model to

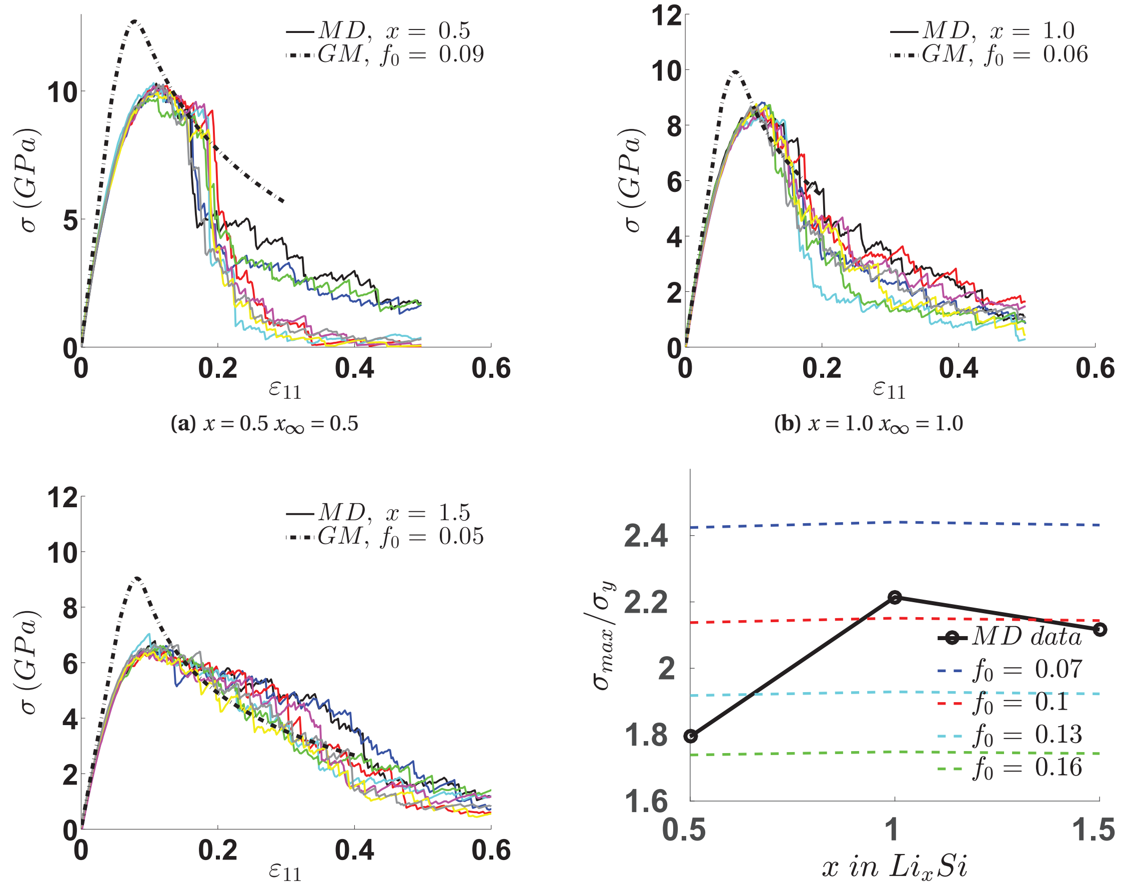

(a) $x = 0.5$ $x_\infty = 0.5$

(b) $x = 1.0$ $x_\infty = 1.0$

(c) $x = 1.5$ $x_\infty = 1.5$

(d) peak stress comparision

Figure 10 – a-c)Fitting of GTN model stress-strain curve to the atomistic simulation of equi-biaxial expansion tests for three different as-quenched samples. For each composition the suitable f_0 in GTN model is shown in the figure. d) Ratio of maximum stress of equi-biaxial expansion tests to the yield stress for MD simulation and GTN model with different initial f_0 versus the composition.

predict fracture of samples with complex geometries.

The work of fracture process depends on the mechanism of the fracture. In most cases of fracture simulation shown in Fig. 6, we only observe activity of one single void in front of the crack. Thus, we use the work per unit area required to rupture one voided cell shown in 9 as an approximate value for the work of fracture. Figure 11 compares the energy of the rupture of equi-biaxial plane strain expansion tests Γ_0 with the initiation fracture toughness. The work of fracture is calculated by integrating the whole area bellow the curves shown in Fig. 9 divided by the fracture area. In all compositions, the work of fracture is higher than J_{IC}. The unit cell simulation is a very simplified model for the fracture process zone and results show up to 50% difference in mean values between Γ_0 and J_{IC}. For the Li composition corresponding to $x = 1$ they are similar within the error of measurement.

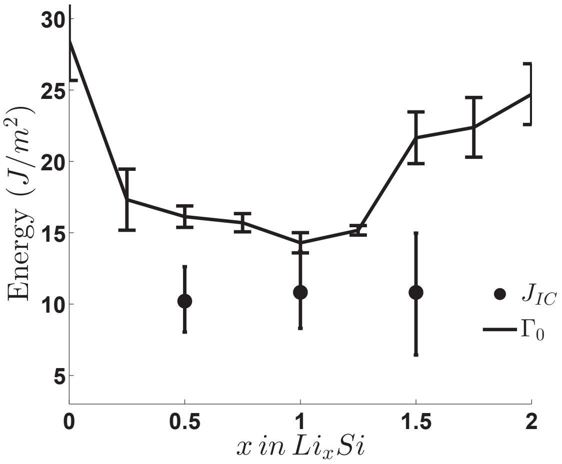

Figure 11 – Comparison of work of fracture for equi-biaxial generalized plane strain samples with initiation fracture energies for as-quenched material.

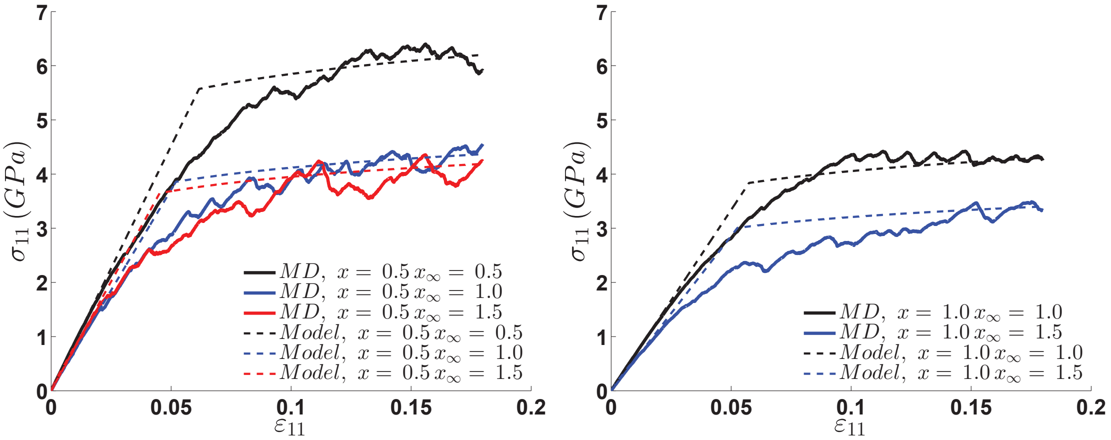

(a) $x = 0.5$

(b) $x = 1.0$

Figure 12 – Stress-strain response of MD discharged amorphous Li$_x$Si compared with model of Eq. 3.6. The parameters used in the model are: $N = 0.1$, $\sigma_0 = 0.9\sigma_f$

3.5 Effect of discharging on the fracture of Li$_x$Si

The major new aspect in the area of Li-Si battery materials in this thesis was presented in Chapter 2. In Chapter 2, on the plasticity of Li$_x$Si alloys, it was demonstrated that the flow behavior of Li-Si is dependent on the (rate-dependent) history of charging and discharging of the material, with faster charging/discharging leading to excess energy that facilitates plastic flow [Khosrownejad and Curtin(2016)]. The question addressed in this section is whether or not charging/discharging processes have any affect on the fracture toughness of Li-Si materials.

We fabricate various Li$_x$Si with different amounts of discharging by selecting a reference sample with concentration x_∞ and successively remove Li in concentration increments of $\Delta x =$

0.1 by extracting Li atoms at random from the structure. After each increment of discharging, the material is relaxed at $T = 1°K$ and $\sigma = 0$ to the local mechanically stable structure. Here, we prepared two materials with initial Li content $x_\infty = 1.0$ and $x_\infty = 1.5$ that have been discharged to a final composition of $x = 0.5$, which can be compared to the as-processed sample at the same compositoin of $x = 0.5$. We have prepared a material with initial Li content $x_\infty = 1.5$ discharged to $x = 1.0$, which can be compared to the as-processed sample at $x = 1.0$.

Figure 12 shows the uniaxial stress-strain curve for the discharged materials and the as-processed materials. Discharging does not greatly change elastic properties but does changes the plastic behavior dramatically. Results in Fig. 12 show that the discharging history decreases the flow stress, and that the yield stress decreases with increasing amount of discharging. The parameters $\sigma_0 = 0.9\sigma_f$ and $N = 0.1$ in the material constitutive model of 3.6 still fit reasonably well for the discharged materials. Similar to as-quenched materials, however, the model is not perfect and can not capture softening in the early stages of plasticity.

Figure 13 shows the R-curves obtained from fracture simulations of the discharged samples, obtained using the same generalized plane strain K_I fracture test as described earlier. Also shown are the previous results for the as-processed materials with the same Li content. In all cases, the initial fracture toughness K_{IC} and also the fracture toughness at $\Delta a = 100\text{Å}$ are higher than the as-prepared samples, with values tabulated in Tab. 5. Thus, crack propagation and fracture toughness in lithiated silicon are both composition and history-dependent processes, in general. There exists a dynamic competition between the relaxation of the glassy material, the rate of charging/discharging, the rate of loading and both the plastic flow behavior [Khosrownejad and Curtin(2016)] and, as now seen here, the fracture behavior. In other words, the fracture properties of Li-Si dynamically change in the course of battery operation (charging and discharging).

The mechanism of fracture in the discharged samples is similar to that found in the as-processed samples. Void nucleation, growth, and coalescence are observed for all discharged samples. However, the void size and spacing (distance from the crack tip) differ from those found in the as-processed materials, as shown in Table 6. The void spacing is increased

Table 5 – K_{IC} and K_I values for fracture tests in Li_xSi with different compositions for discharged and as-quenched samples.

x, x_∞ in Li_xSi	K_{IC}	$K_I(\Delta a = 100\text{Å})$	$K_I(\Delta a = 100\text{Å})/K_{IC}$	f_0
0.5, 0.5	1.0086 ± 0.1129	1.8881 ± 0.1932	1.87	0.09
0.5, 1.0	1.2027 ± 0.2122	3.2000 ± 0.4243	3.76	0.018
0.5, 1.5	1.3233 ± 0.0735	2.6900 ± 0.1697	3.09	0.02
1.0, 1.0	0.8869 ± 0.1096	1.9941 ± 0.2873	2.24	0.06
1.0, 1.5	1.3016 ± 0.0130	3.0925 ± 0.1732	2.99	0.015
1.5, 1.5	0.7839 ± 0.1789	1.8377 ± 0.3684	2.34	0.05

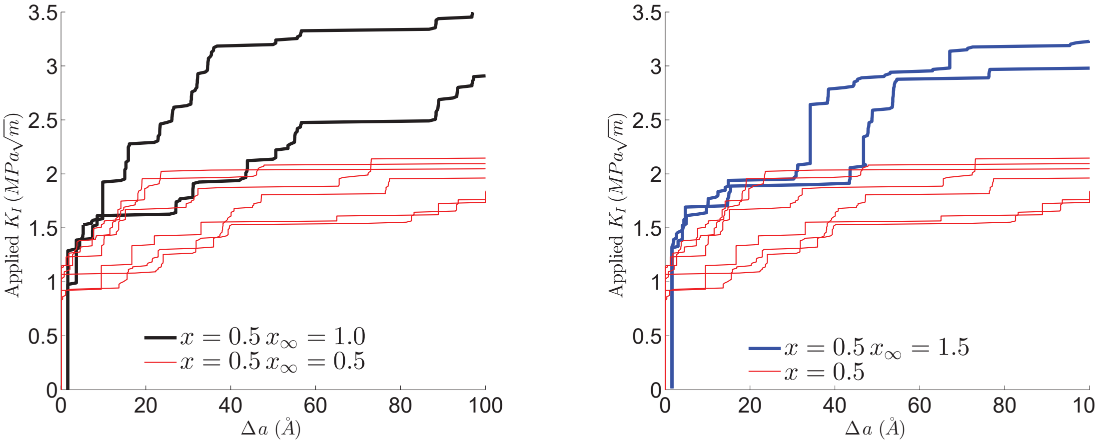

(a) $x = 0.5\ x_\infty = 1.0$ **(b)** $x = 0.5\ x_\infty = 1.5$

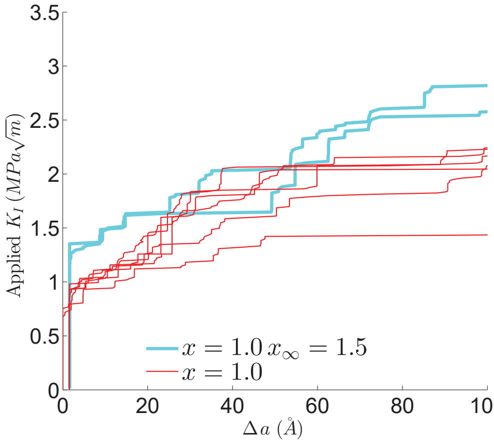

(c) $x = 1.0\ x_\infty = 1.5$

Figure 13 – R-curve obtained using MD simulations for three different discharged samples. For each composition 2 samples have been simulated and compared with non-discharged samples at the same composition of lithium.

with the amount of discharging. Correspondingly, the value of α increases relative to the as-processed materials, but is roughly the same across all the discharged material studeid here.

To further examine the mechanics of the FPZ in the discharged samples, we performed equi-biaxial generalized plane strain expansion simulations for the discharged samples using the sizes and methods discussed for the as-prepared samples. Figure 14 shows the fitting of the GTN model to these equi-biaxial expansion tests on discharged samples. We used slightly higher value of $q_2 = 0.68$ to better fit the MD results for discharged samples. The response of the as-prepared sample at the same composition is also shown in the Fig. 14 for comparison. Similar to Fig. 10, two methods of comparison is used to find f_0. Figure 14-a,c shows the fitting of stress evolution in equi-biaxial tests. The fit is again not ideal because the material model does not capture the softening of the material for low and moderate plastic strains,

Table 6 – Measured values of D parameter in MD simulation along with J_{IC} and α for different compositions after discharging.

x, x_∞ in Li$_x$Si	D(Å)	$J_{IC}(J/m^2)$	$\alpha = J_{IC}/\sigma_0 D$
0.5, 0.5	6.1 ± 1.1 (Å)	$10.204^{+2.65}_{-2.37}$	2.70 ± 1.1
0.5, 1.0	8.3 ± 1.1 (Å)	17.742	4.98
0.5, 1.5	11.0 ± 0.5 (Å)	27.895	5.15
1.0, 1.0	10.7 ± 1.3 (Å)	$10.571^{+3.14}_{-2.77}$	2.31 ± 0.9
1.0, 1.5	14.1 ± 2.5 (Å)	19.113	4.36
1.5, 1.5	14.9 ± 1.6 (Å)	$10.818^{6.06}_{-4.81}$	2.31 ± 1.1

but is comparable to the fit for the as-prepared samples. Comparison of peak stress values for the MD data and GTN model for equi-biaxial tests are shown in Fig. 14-b,d. The obtained values for f_0 in this method of modelling MD with GTN are higher but the trend of change is similar to the first method of fitting the curves. The fitted values of f_0 are smaller for discharged samples than as-prepared samples. This is surprising, since one might envision that discharging increases free volume and thus facilitates void nucleation, which would correspond to a larger f_0. However, the discharging creates excess energy and lower flow stresses, which may suppress growth of voids at the scale necessary to affect f_0. In any case, lower f_0 results in higher value for α or equivalently a higher initiation fracture energy in the GTN model [Pardoen and Hutchinson(2003)]. Table 6 shows that indeed the initiation fracture energy J_{IC} is higher for the discharged samples, in qualitative agreement with the GTN model with lower f_0 for discharged materials.

Lower values of f_0 values are also predicted to increases the slope of the R-curve [Xia and Shih(1995a)]. Table 5 shows the ratio of K at $\Delta a = 100$Å and K_{IC} as an approximate measure for the slope of the resistance curve. In agreement with the GTN model predictions, the discharged samples with lower f_0 have higher slopes than the as-prepared samples with higher f_0. Thus, while the GTN model fit for f_0 is clearly approximate, the changes in initiation fracture energy and R-curve slope for both discharged samples and as-prepared samples follow the predicted trends of GTN based fracture simulations.

Measurement of the work of fracture Γ_0 can predict the trend of change in the initiation fracture energy J_{IC}. The work of fracture for discharged cases is higher than that for as-prepared samples, as is the initiation fracture energy J_{IC} (see Figure 14). The magnitudes of the changes differ, however, so only the trends are similar.

3.6 Discussion

Experimentally measured values for fracture energy of Li$_x$Si obtained from Pharr. et. al. [Pharr et al.(2013)Pharr, Suo, and Vlassak] and Wang et. al. [Wang et al.(2015)Wang, Fan, Wang, Wang, Tao, Yang, Liu, Chew, Mao, Zhu, et al.] is tabulated in Table 7. For $x = 0.5$, we showed the average values of two adjacent reported values. None of the experiments reported the fracture toughness for $x = 1.5$. MD structures have greater yield stresses than the reported values in Pharr. et. al. [Pharr et al.(2013)Pharr, Suo, and Vlassak]. On the other hand, the fracture energy scales with yield stress (See Eq. 3.11), thus by rescaling fracture energies obtained from fracture simulations with the experimental yield stresses, we tabulated J^p_{IC} and $J^p_I(\Delta a = 200\text{Å})$ for as-quenched structures of different compositions in Table 7. J^p_{IC} is thus the predicted value of initiation fracture energy assuming that MD simulations correctly estimates value of D and α. The predicted initiation fracture energy is relatively constant among compositions and the value of fracture energy for extended crack shows an increase with Li composition.

For the range of material parameters and f_0 calculated for MD structures in this work, the

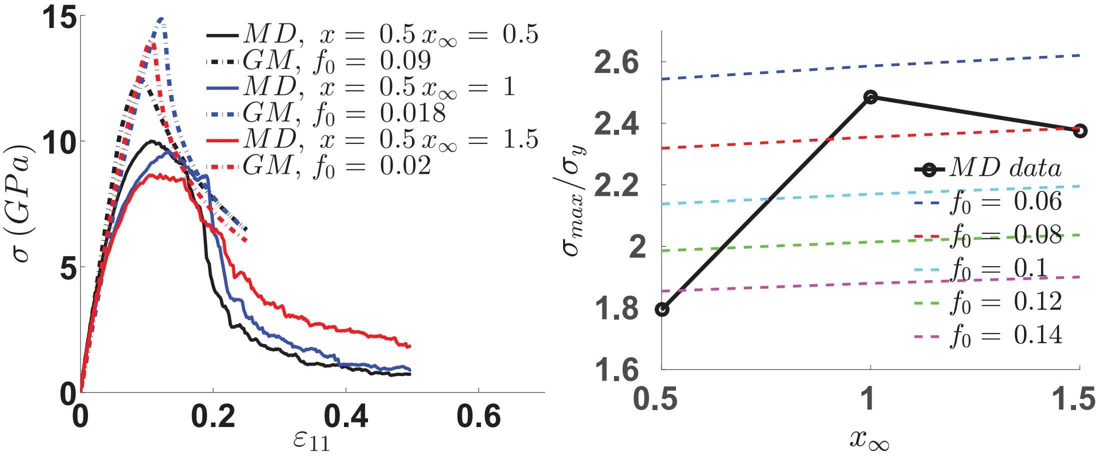

(a) $x = 0.5$ **(b)** $x = 0.5$

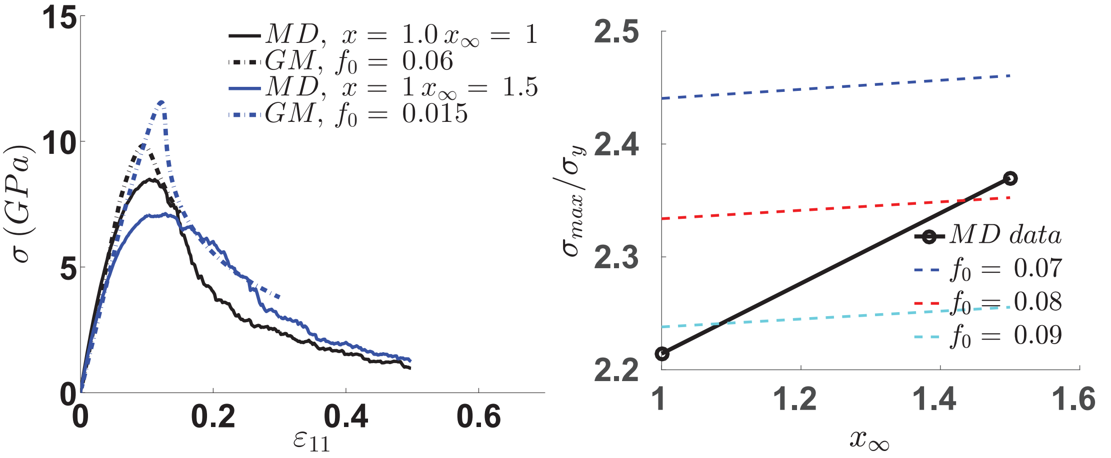

(c) $x = 1.0$ **(d)** $x = 1.0$

Figure 14 – a,c) Fitting of GTN model stress-strain curve to the atomistic simulation of equi-biaxial expansion tests for discharged samples with a)$x = 0.5$ and c)$x = 1.0$. b,d) Ratio of maximum stress of equi-biaxial expansion tests to the yield stress for MD simulation and GTN model with different initial f_0 versus the x_∞ for b)$x = 0.5$ and d)$x = 1.0$ in Li$_x$Si .

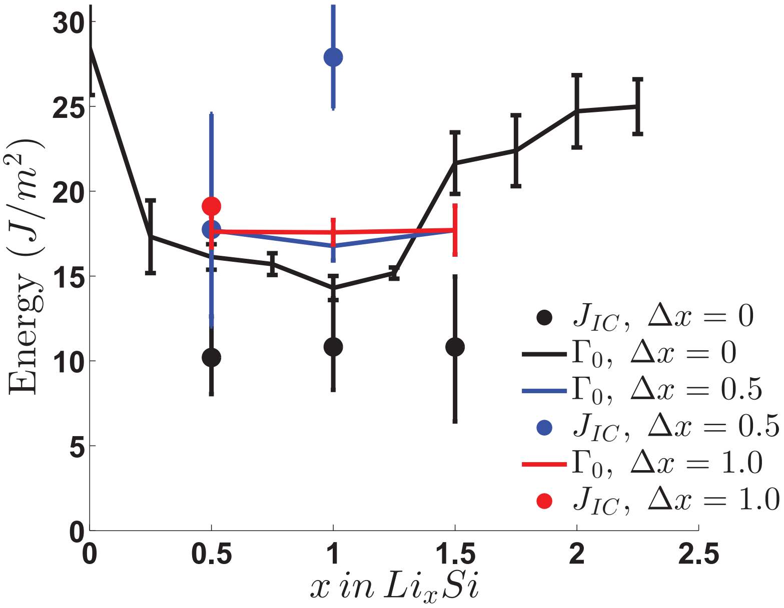

Figure 15 – Comparison of work of fracture for equi-biaxial generalized plane strain samples with initiation fracture energies for as-quenched and discharged material.

Table 7 – Predicted experimental fracture energy of Li$_x$Si based on MD simulations.

x in Li$_x$Si	σ_y^e (GPa) [Pharr et.al.]	J_{IC}^p (J/m^2)	$J_I^p(\Delta a = 200Å)$ (J/m^2)	J_{IC} [Pharr et.al.]	J_{IC} [Wang et.al.]
0.5	0.85	1.40	7.55	11.2	3.2
1.0	0.6	1.48	12.82	5.4	7.8
1.5	0.5	1.58	19.29	–	–

Gurson model based fracture simulations (See [Xia and Shih(1995a)]) show almost flat R-curve after $\Delta a/D > 20$, thus the $J_{IC}^p(\Delta a = 200Å)$ is presumably close to the steady state fracture energy J_{ss}. Despite all complications of MD simulation of amorphous systems, the $J_{IC}^p(\Delta a = 200Å)$ is reasonably close to the experimental values. The exact shape of R-curve in Gurson model based fracture simulation highly depend on the geometry and loading condition of samples. Specifically, the value of T stress has a big effect on the R-curve of the Gurson model R-curves. The T-stress for both experimental studies reported here is positive. Xia & Shin [Xia and Shih(1995a)] showed that $T/\sigma_0 = 0.5$ reduces the fracture energies throughout crack growth by about 35%. The K_I MD fracture tests are done with zero T-stress and thus the obtained fracture energies are a higher bound for the fracture energies of discharging thin film and nano-indentation geometries. To be able to compare the experimental values with predictions of MD we should perform a simulations with realistic geometries that is a route of future research.

3.7 Conclusion

In this research, we have performed systematic atomistic simulation of crack propagation in lithiated silicon for three different compositions of Li$_x$Si and discharged samples. The initiation stress intensity factor K_{IC} is bigger for lower lithium content, but the slope of the resistance curve is smaller for these cases as well, such that $K_I(\Delta a = 200\text{Å})$ are much closer together. To better understand and quantify trends in the fracture behavior, we analyzed the nano-mechanisms of fracture, which was shown to be void nucleation and coalescence for all compositions. The mechanism is thus similar to the ductile fracture mechanism proposed in Gurson-type models for larger-scale fracture, and the GTN model was used to help interpret the simulation results.

Fracture simulations based on GTN suggest that the energy of fracture J_I scales with $\sigma_0 D$ with scaling factor α. We proposed D, as the characteristic length in Gurson fracture models, to be the distance of formed void in front of the crack to the crack tip. The size and spacing of the voids depend on composition, however the initiation fracture energy scales with the same factor α for three as-quenched samples. The scaling factor differs in discharged sample from as-quenched ones but remains similar among discharged samples. Similar to fracture simulation based on Gurson, R-curves does not saturate even for high values of crack growth $\Delta a/D > 15$. Furthermore, we performed series of generalized plane strain equi-biaxial expansion tests on specimen to model the fracture process zone in front of a crack. By fitting the stress-strain curve of equi-biaxially loaded cells with GTN model, we found the initial void volume fraction f_0. The value of f_0 for different compositions rationalize trends in initial fracture energy and the slope of the R-curves. We obtained lower f_0 for discharged cases, which describes the trend of having both higher initiation fracture energy and resistance curve slope, with regards to the GTN based fracture simulations. Considering, the observed void nucleation, growth and coalescence nano-mechanism of fracture and qualitative agreement with the GTN based fracture simulation, we conclude that the ductile fracture model based on Gurson type mechanism of fracture can describe the fracture in Li$_x$Si during charging/discharging.

Despite the fact that the material is ductile, the fracture energies are relatively low. Amorphous Li$_x$Si ahead of the crack tip easily cavitates to form voids which are spaced few nanometers ahead of the crack tip. The toughness of the material scales with $\sigma_0 D$ and the experimental yield stresses are lower than MD. Scaling the fracture energies of MD with experimental yield stresses, we obtained the fracture energies similar to experimental values. Thus, lithiated silicon despite high ductility and ability to flow plastically, fractures in a brittle manner. We further discussed the differences of MD fracture test and experimental conditions.

Finally, in our simulations we see different behavior for discharged samples than for the as-prepared samples. Both the initiation fracture energy and the slope of the R-curves are higher for the discharged samples. The discharged samples can be relaxed in time to give a more relaxed structure with a higher yield stress and thus totally different fracture properties. Thus not only the yield stress is a function of charging/discharging history, the fracture toughness in lithiated silicon is also a function of the charging/discharging state of the material as well as the loading rates and composition of the material.

4 Finite element model of elasto-plastic chemo-mechanics

In this chapter, the continuum-thermodynamics basis for chemo-mechanics with excess energy as an internal variable is established. This derivation includes the typical steps of defining the energy functional for the physical system of interest, decomposing the strain measure and deriving the conjugate thermodynamic variables. The strong form of the boundary value problem equations will be followed up. Next, an appropriate material model for nonlinear chemo-mechanics with excess energy as an internal variable is developed. The solution of the balance equations in combination with the constitutive equations gives us the chemo-mechanical fields within the region under consideration. Followed by above derivations, a finite element model is proposed which allows the computation of approximate numerical solutions to the variational problem of nonlinear small strain chemo-mechanics.

Among finite element formulations for the chemo-mechanics in lithium ion batteries, Dal and Miehe [Dal and Miehe(2015)] developed a finite strain theory for chemo-mechanics in Li-ion batteries. Their focus was developing a general finite strain formulation and they did not incorporate nonlinear mechanics. Bower and Guduru also developed a finite element model of diffusion, finite deformation, plasticity and fracture in lithium ion batteries [Bower and Guduru(2012b)]. Here, we extend these models to formulate a material with excess energy as an internal variable. At present, the proposed constitutive model in Chapter 2 does not explicitly address the processes of Li diffusion through the material. Thus, we do not incorporate diffusion in the material model. We only focus on formulating a system with uniform composition with imposed rate of charge/discharge.

In Sec. 4.1, we present a general continuum mechanics formulation of the chemo-mechanical system. Then, we develop a constitutive model for the chemo-mechanics in Sec.4.2. The Finite element discretization is presented in Sec. 4.3, followed by material state update algorithms. Finally, the results of applying the model to few geometric settings is shown in Sec. 4.4.

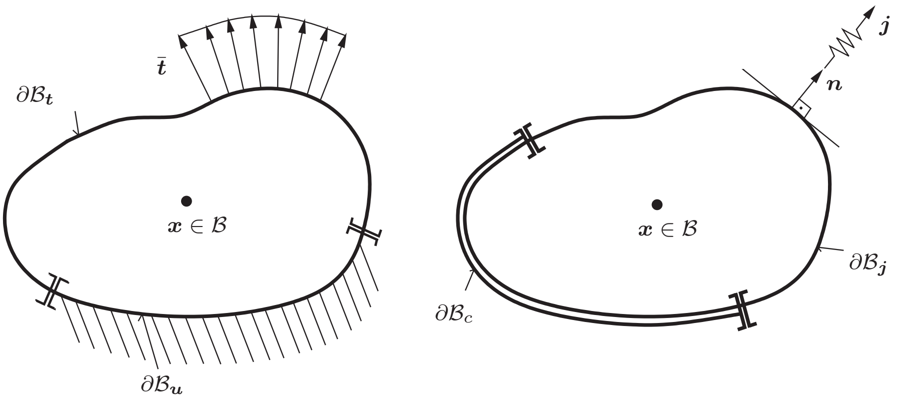

Figure 1 – Chemo-mechanics boundary value problem for displacement and concentration fields. The boundary is decomposed into Dirichlet and Neuman boundary types for each sub problem.

4.1 Continuum thermodynamics of chemo-mechanical system

The boundary value problem for chemo-mechanics is a coupled problem characterized by the deformation field $\boldsymbol{u}$, and concentration field c. A material body B is mathematically defined as the open set of material points P, which can be identified with geometrical points in the three-dimensional Euclidean space $\mathbb{R}^3$ via the one-to-one configuration placement map $\boldsymbol{\chi}$. In the *referential description of motion* one defines the *reference* or *Lagrangian configuration* as the placement of the body at time t_0, i.e. $\mathscr{B} := \boldsymbol{\chi}_{t_0}(B)$, with the *reference coordinates* $\boldsymbol{X} := \boldsymbol{\chi}_{t_0}(P) \in \mathscr{B}$. The *current* or *Eulerian configuration* at time t is defined as $\mathscr{S} := \boldsymbol{\chi}_t(B)$, with the *spatial coordinates* $\boldsymbol{x} := \boldsymbol{\chi}_t(P) \in \mathscr{S}$. Here, we make the small strain assumption. In the small strain setting, we do not distinguish between $\mathscr{B}$ and $\mathscr{S}$ and we formally define the displacement of the body and concentration as time-parametrized functions over $\mathscr{B}$.

$$\boldsymbol{u} := \begin{cases} \mathscr{B} \times \mathbb{R}_+ \to \mathscr{B} \in \mathbb{R}^3 \,, \\ (\boldsymbol{x}, t) \mapsto \boldsymbol{u}(\boldsymbol{x}, t) = \boldsymbol{x} - \boldsymbol{X} \end{cases} \tag{4.1}$$

$$c := \begin{cases} \mathscr{B} \times \mathbb{R}_+ \to \mathbb{R} \,, \\ (\boldsymbol{x}, t) \mapsto c(\boldsymbol{x}, t) = \dfrac{dv_c}{dv} \end{cases} \tag{4.2}$$

The concentration field at each point represents the volume of the species divided by the total volume of the body. Natural boundary conditions for the displacement field and concentration fields are expressed in terms of traction $\boldsymbol{t}$ and flux $\boldsymbol{j}$, respectively, see Figure 1.

4.1.1 Governing equations

The governing equations of the chemo-mechanics can be derived from global balance laws. Specifically, the diffusion of Li-species through the deforming solid is governed by:

$$\frac{d}{dt}\mathcal{M}_{Li} = \int_{\partial\mathcal{B}} \boldsymbol{j}\, da \qquad \rightarrow \qquad \frac{d}{dt}\int_{\mathcal{B}} \rho\, c\, dv = \int_{\partial\mathcal{B}} \boldsymbol{j}\, da \tag{4.3}$$

In which $\mathcal{M}_{Li}$ is the total mass of lithium, ρ is the density of the non-lithiated matter and $\boldsymbol{j}$ represents the flux through the boundary of the domain. The local form of the lithium diffusion is as follows:

$$\rho\dot{c} = -\nabla_{\boldsymbol{x}}\boldsymbol{j} \qquad \text{in} \quad \mathcal{B} \tag{4.4}$$

For small strain mechanics, the local form of linear and angular momentum are as follows:

$$\begin{aligned} \nabla_{\boldsymbol{x}}\boldsymbol{\sigma} + \rho\boldsymbol{\gamma} &= 0 \quad \text{in} \quad \mathcal{B}, \qquad \text{with} \qquad \boldsymbol{\sigma}\boldsymbol{n} = \bar{t} \quad \text{on} \quad \partial\mathcal{B}_t \\ \text{skew}\,[\boldsymbol{\sigma}] &= 0 \quad \text{in} \quad \mathcal{B} \end{aligned} \tag{4.5}$$

Here, $\boldsymbol{\gamma}$ is the body force per unit volume and $\boldsymbol{\sigma}$ is the cauchy stress.

4.1.2 Dissipation principle and material law forms

A constitutive theory is considered to be thermodynamically consistent if it satisfies the fundamental balance equations of continuum mechanics and the laws of thermodynamics at each material point. It is assumed that all thermodynamic properties of the material can be characterized by a (scalar-valued) thermodynamic potential, i.e., free energy ψ. We derive general constitutive relations for the dependent field variables in the form of gradients to this thermodynamic potential, such that thermodynamic consistency is guaranteed a priori. The second law of thermodynamics states that the rate of energy stored in the system should be smaller than the power of chemo-mechanical external action on the body.

$$\frac{d}{dt}\int_{\mathcal{B}} \rho\psi\, dv \leq \int_{\mathcal{B}} \rho\boldsymbol{\gamma}\cdot\boldsymbol{v}\, dv + \int_{\partial\mathcal{B}} \rho\boldsymbol{t}\cdot\boldsymbol{v}\, dv - \int_{\partial\mathcal{B}} \mu\,\boldsymbol{j}\cdot\boldsymbol{n}\, da \tag{4.6}$$

The first two terms on the right hand side of this equations represent the mechanical power due to body forces and tractions, with $\boldsymbol{v}$ being the velocity field. The last term is the flux of the energy due to diffusion of species out of the body with μ being the chemical potential field. Using Gauss's theorem for sufficiently smooth fields yields the following local dissipation postulate:

$$\rho\mathcal{D} = \boldsymbol{\sigma} : \dot{\boldsymbol{\varepsilon}} - \rho\dot{\psi} + \mu\rho\dot{c} - \boldsymbol{j}\cdot\nabla_{\boldsymbol{x}}\mu > 0 \tag{4.7}$$

Here, we assume a free energy of the form

$$\psi = \psi(\boldsymbol{\varepsilon}, c, \xi) \tag{4.8}$$

and formally derive the thermodynamically consistent material model for chemo-mechanics with excess energy as an internal variable. Variable ξ is the internal variable which is the kinematic conjugate to excess energy. As we will discuss in the constitutive behavior formulation, we will not directly work with ξ and its evolution equation but with its thermodynamic conjugate variable instead, namely the excess energy e^{xc}. Putting definition 4.8 in the energy dissipation from 4.7, and using the the time derivative of free energy function we get the following form for material point dissipation $\mathscr{D}$.

$$\rho\mathscr{D} = \boldsymbol{\sigma} : \dot{\boldsymbol{\varepsilon}} + \mu\rho\dot{c} - \rho\left(\partial_{\boldsymbol{\varepsilon}}\psi : \dot{\boldsymbol{\varepsilon}} + \partial_{\xi}\psi\,\dot{\xi} + \partial_{c}\psi\,\dot{c}\right) - \boldsymbol{j}\cdot\nabla_{\boldsymbol{x}}\mu \geq 0 \tag{4.9}$$

Here we can split the dissipation into local action, diffusion and dissipation parts.

$$\rho\mathscr{D}_{loc} = \boldsymbol{\sigma} : \dot{\boldsymbol{\varepsilon}} + \mu\rho\dot{c} - \rho\partial_{\boldsymbol{\varepsilon}}\psi : \dot{\boldsymbol{\varepsilon}} - \rho\partial_{c}\psi\,\dot{c} = 0 \tag{4.10}$$

$$-\rho\partial_{\xi}\psi\,\dot{\xi} \geq 0 \qquad , \qquad -\boldsymbol{j}\cdot\nabla_{\boldsymbol{x}}\mu \geq 0 \tag{4.11}$$

Equation 4.10 gives us the following definitions for thermodynamical conjugate variables, namely stress $\boldsymbol{\sigma}$ and chemical potentialμ:

$$\boldsymbol{\sigma} = \rho\partial_{\boldsymbol{\varepsilon}}\psi : \dot{\boldsymbol{\varepsilon}} \tag{4.12}$$

$$\mu = \partial_{c}\psi\,\dot{c} \tag{4.13}$$

Furthermore, the first part of Eq. 4.11 defines the condition on internal variable evolution equation ξ to have a thermodynamically consistent formulation. As we are working with the e^{xc} instead of the kinematic variable ξ, we cannot directly verify this property, unless there exist a physically meaningful relation between these two variables. However, as discussed in Chapter 2, choosing a kinematic variable to describe the internal state of an amorphous material is not straight forward and a topic of separate research. The second part of Eq. 4.11 defines a constraint on diffusion. Here, we have only formulated a system with a uniform concentration of lithium everywhere, thus the flux is zero. Hence, the second part is automatically satisfied.

4.2 Constitutive modeling of irreversible chemo-mechanics

4.2.1 Kinematics assumptions

We split the strain tensor into three additive components. The swelling strain $\boldsymbol{\varepsilon}^c$ captures the deformation due to changes in the lithium concentration, the elastic strain $\boldsymbol{\varepsilon}^e$ is the reversible strain and $\boldsymbol{\varepsilon}^p$ represents the plastic deformation of the body.

$$\boldsymbol{\varepsilon} = \boldsymbol{\varepsilon}^c + \boldsymbol{\varepsilon}^e + \boldsymbol{\varepsilon}^p \tag{4.14}$$

The form of the swelling part of the deformation is assumed to be isotropic and only changing the volume. The following constitutive function describes the swelling part of the deformation

$$\varepsilon^c_{ij} = \frac{\beta(c)}{3}\delta_{ij} \qquad \rightarrow \qquad \boldsymbol{\varepsilon}^{c\prime} = 0 \tag{4.15}$$

where $\beta(c)$ is the composition dependant linear expansion coefficient due to charging, i.e the change in volume due to adding one lithium atom divided by the average atomic volume. The isochoric part of the swelling deformation $\boldsymbol{\varepsilon}^{c\prime}$ is zero as it is only creating volumetric deformation. Here we use a J_2 type plasticity, i.e., we assume that the material does not have any volumetric plasticity. This assumption should be enhanced, as we observed volumetric plasticity in lithiated silicon as discussed in Chapter 3.

$$\mathrm{tr}\left[\boldsymbol{\varepsilon}^p\right] = \varepsilon^p_{ii} = 0 \tag{4.16}$$

4.2.2 Free energy form

We assume the following additive split of the stored free energy into mechanical (elastic) strain energy density ψ^e, the chemical contribution to the free energy ψ^c and an excess structural disorder energy density following the model described in Chapter 2.

$$\psi(\boldsymbol{\varepsilon}, c, \xi) = \psi^e(\boldsymbol{\varepsilon}^e, c) + \psi^c(c) + e^{xc}(c, \xi) \tag{4.17}$$

Here, for simplicity, and referring to the MD results in Chapter 2, we neglect the dependence of the elastic energy on the internal variable ξ. The important aspect of the energy functional 4.17 is that we do not need to specify the structural disorder parameter ξ and its evolution equation as it only appears in the excess energy part. We can choose to use an evolution equation for e^{xc} instead.

In order to make concrete model examples, we used the following isotropic elastic model for the elastic energy.

$$\psi^e(\boldsymbol{\varepsilon}^e, c) = \frac{k(c)}{2}\mathrm{tr}^2\left[\boldsymbol{\varepsilon}^e\right] + G(c)\,\boldsymbol{\varepsilon}^{e\prime} : \boldsymbol{\varepsilon}^{e\prime} \tag{4.18}$$

In which $k(c)$ and $G(c)$ are the concentration-dependent bulk modulus and shear modulus, respectively. ${\varepsilon^{e\prime}}_{ij} = {\varepsilon^e}_{ij} - {\varepsilon^e}_{ii}/3$ is the isochoric part of strain. The chemical contribution to the free energy is not important as we did not model diffusion here.

4.2.3 Plastic strain and excess energy evolution

In the current formulation of chemo-mechanics, we need to specify evolution equations of two non-conserved variables, i.e., excess energy, and plastic strain. As discussed in the plasticity model in Chapter 2, we use a viscoplastic model modified with excess energy. Here, we present a tensorial formulation for the plastic material presented in Chapter 2. We assume J_2 plasticity here, thus plastic strain evolution can be expressed as:

$$\dot{\boldsymbol{\varepsilon}}^p = \frac{\dot{\gamma}_p}{\sqrt{2}}\frac{\boldsymbol{\sigma}'}{\|\boldsymbol{\sigma}'\|} = \frac{\dot{\gamma}}{2}\frac{\boldsymbol{\sigma}'}{\tau^e} \qquad , \qquad \tau^e = \sqrt{J_{2,\boldsymbol{\sigma}'}} = \sqrt{\frac{1}{2}\boldsymbol{\sigma}':\boldsymbol{\sigma}'} \tag{4.19}$$

We gave a complete description on the flow response and excess energy evolution in Chapter 2 and here we only show the resultant constitutive forms that are being used here.

$$\dot{\gamma}_p = \dot{\gamma}_0 \exp\left(-\frac{\Delta G - N_{stz}e^{xc}}{k_B T}\right) 2\sinh\left(\frac{\tau^e \Omega}{k_B T}\right) \tag{4.20}$$

$$\dot{e}^{xc} = |\frac{\partial e^{xc}}{\partial x}\dot{x}| + \nu \exp\left(-\frac{\Delta G - N_{stz}e^{xc}}{k_B T}\right)\left\{\left[\cosh\left(\frac{\tau^e \Omega}{k_B T}\right) - 1\right] C_s e^{xc}_m - \cosh\left(\frac{\tau^e \Omega}{k_B T}\right) e^{xc}\right\} \tag{4.21}$$

4.3 Finite element formulation for nolinear chemo-mechanics

4.3.1 A space-time discrete finite element formulation

The governing equations derived in this chapter can be solved using the finite element method. We discretize the field variables at a set of M nodes in the solid. We will denote the coordinates of these special points by x_i^x, where the superscript x ranges from 1 to M for number of nodes in the discretization of the domain $\mathscr{B}$ and the subscript i denotes coordinate axis. The unknown displacement vector at each node is denoted by u_i^x. The shape function at each node is denotes as N^x for each node.

$$u_i = \sum_{x=1}^{M} N^x u_i^x \tag{4.22}$$

We assume the discrete independent variables vector $\boldsymbol{u}_n$ are known at time t_n. The objective is to determine their value at time $t_{n+1} = t_n + \Delta t$. For convenience, we do not show the time tag of the current time $\boldsymbol{u} = \boldsymbol{u}_n$. The weak forms of linear momentum balance 4.5 reads

$$\int_{\mathscr{B}} \left(\boldsymbol{\sigma} : \delta\boldsymbol{\varepsilon} + \rho\boldsymbol{\gamma}\delta\boldsymbol{u}\right) dv - \int_{\partial\mathscr{B}} \bar{\boldsymbol{t}} \cdot \delta\boldsymbol{u}\, da = 0 \tag{4.23}$$

Using weak forms, we calculate the discrete residual vector, with the discrete form 4.22 for the displacement vector $\boldsymbol{u}$.

$$R_i^x = \int_{\mathscr{B}} \sigma_{ij}\left[\varepsilon_{kl}(u_i^x)\right]\frac{\partial N^x}{\partial x_j} + \int_{\mathscr{B}} \rho\gamma_i N^x dv - \int_{\partial\mathscr{B}} \bar{t}_i N^x da = 0, \qquad \forall i, x \tag{4.24}$$

In the discrete residual 4.24, the stress is material-dependent and should be calculated for each specific material. The calculation of material-dependent values is presented in the next section. The non-linear system of equations $\boldsymbol{R}(\boldsymbol{u}) = 0$ can be solved using the iterative Newton-Raphson method based on updates of the form

$$\boldsymbol{u}_{n+1}^{j+1} = \boldsymbol{u}_{n+1}^{j} - [D\boldsymbol{R}(\boldsymbol{u}_{n+1}^{j})]^{-1}\boldsymbol{R}(\boldsymbol{u}_{n+1}^{j}), \qquad \text{with} \qquad \boldsymbol{u}_{n+1}^{0} = \boldsymbol{u}_n \tag{4.25}$$

This iterative scheme continues until the convergence of the form $\|\boldsymbol{R}\| < tol$ is achieved. Here, we need a full linearization of the system to calculate $\boldsymbol{K} = D\boldsymbol{R}(\boldsymbol{u})$. Below shows the residual discrete full derivative[Bower(2009)].

$$K_{ik}^{xy} = \int_{\mathscr{B}} \mathbb{C}^{ep}\frac{\partial N^x}{\partial x_j}\frac{\partial N^x}{\partial x_l}dv, \qquad \text{with} \qquad \mathbb{C}^{ep} = \frac{\sigma_{ij}}{\varepsilon_{kl}} \tag{4.26}$$

Just as the residual, the derivative of stress with respect to strain is a material-specific calculation that is presented in the next section.

4.3.2 Material state update algorithm

In this section, we derive the material model for the finite element formulation presented in the previous section. Equation 4.25 shows that for each non-linear iteration having the jth estimate of $\boldsymbol{u}_{n+1}$, we should calculate the residual and the full linearization of it. Thus, in the material state update algorithm, knowing $\boldsymbol{u}_{n+1}$, we calculate stress $\boldsymbol{\sigma}_{n+1}$ and consistent moduli $\mathbb{C}_{n+1}^{ep}$. Here we do not show the indices for the time step where it is evident from the context. Stress can be decomposed into a volumetric and a deviatoric part as follows

$$\boldsymbol{\sigma} = \frac{1}{3}\mathrm{tr}[\boldsymbol{\sigma}]\,\boldsymbol{I} + \boldsymbol{\sigma}' = \frac{1}{3}\boldsymbol{\sigma}^v + \boldsymbol{\sigma}' \tag{4.27}$$

The volumetric part of the stress can be calculated using the definition 4.12.

$$\sigma_{ii} = \frac{\partial\psi}{\partial\varepsilon_{ii}} = \frac{\partial\psi}{\partial e} \tag{4.28}$$

With $e = \mathrm{tr}[\boldsymbol{\varepsilon}]$. Having a specific form for the free energy of the material in Eq. 4.18, we can calculate the volumetric stress.

$$\boldsymbol{\sigma}_{n+1}^v = \frac{\partial\psi}{\partial e_{n+1}}\boldsymbol{I} = k(c)e_{n+1}\boldsymbol{I} \tag{4.29}$$

Using the property of the fourth order deviatoric projector $\frac{\partial \boldsymbol{\varepsilon}'}{\partial \boldsymbol{\varepsilon}} = \mathbb{P}_{ijkl} = \delta_{ik}\delta_{jl} - \frac{1}{3}\delta_{ij}\delta_{kl}$ we can calculate the deviatoric part of the stress.

$$\boldsymbol{\sigma}' = \mathbb{P} : \boldsymbol{\sigma} = \mathbb{P} : \frac{\partial \psi}{\partial \boldsymbol{\varepsilon}} = \frac{\partial \psi}{\partial \boldsymbol{\varepsilon}^{e'}} \tag{4.30}$$

With the specific form of the free energy in Eq. 4.18, the deviatoric part of the stress at time $n+1$ reads

$$\boldsymbol{\sigma}'_{n+1} = 2\,G(c)\,\boldsymbol{\varepsilon}^{e'}_{n+1} = 2\,G(c)\,(\boldsymbol{\varepsilon}'_{n+1} - \boldsymbol{\varepsilon}^{p}_{n+1}) \tag{4.31}$$

At time $n+1$, the total strain is known and we need to find the plastic strain at time $n+1$. Integrating the evolution equation 4.19 by implicit Euler scheme, we get

$$\boldsymbol{\varepsilon}^{p}_{n+1} = \boldsymbol{\varepsilon}^{p}_{n} + \eta_{n+1}\boldsymbol{n}_{n+1}, \qquad \text{with} \quad \eta_{n+1} = \frac{\dot{\gamma}_{n+1}}{\sqrt{2}}\Delta t, \qquad \boldsymbol{n} = \frac{\boldsymbol{\sigma}}{\|\boldsymbol{\sigma}\|} \tag{4.32}$$

$\boldsymbol{n}$ is the direction of stress with $\|\boldsymbol{n}\| = 1$. Putting Eq. 4.32 in Eq. 4.31, we get

$$\begin{aligned} \boldsymbol{\sigma}'_{n+1} &= 2\,G(c)\,(\boldsymbol{\varepsilon}'_{n+1} - \boldsymbol{\varepsilon}^{p}_{n+1}) && (4.33)\\ &= 2\,G(c)\,(\boldsymbol{\varepsilon}'_{n+1} - \boldsymbol{\varepsilon}^{p}_{n}) - 2\,G(c)\,\eta_{n+1}\boldsymbol{n}_{n+1} && (4.34)\\ &= \boldsymbol{\sigma}'^{,tr}_{n+1} \qquad\qquad\quad - 2\,G(c)\,\eta_{n+1}\boldsymbol{n}_{n+1} && (4.35) \end{aligned}$$

The trial deviatoric stress is defined as $\boldsymbol{\sigma}'^{,tr}_{n+1} = G(c)\,(\boldsymbol{\varepsilon}'_{n+1} - \boldsymbol{\varepsilon}^{p}_{n})$. Multiplying the Eq. 4.33 by one, we obtain

$$\begin{aligned} \boldsymbol{\sigma}'_{n+1}\frac{\|\boldsymbol{\sigma}'_{n+1}\|}{\|\boldsymbol{\sigma}'_{n+1}\|} &= \boldsymbol{\sigma}'^{,tr}_{n+1}\frac{\|\boldsymbol{\sigma}'_{n+1}\|}{\|\boldsymbol{\sigma}'_{n+1}\|} - 2\,G(c)\,\eta_{n+1}\boldsymbol{n}_{n+1} && (4.36)\\ \|\boldsymbol{\sigma}'_{n+1}\|\,\boldsymbol{n}_{n+1} &= \|\boldsymbol{\sigma}'^{,tr}_{n+1}\|\,\boldsymbol{n}^{tr}_{n+1} - 2\,G(c)\,\eta_{n+1}\boldsymbol{n}_{n+1} && (4.37) \end{aligned}$$

The Eq. 4.36 yields two important results

$$\begin{aligned} &\boldsymbol{n}_{n+1} = \boldsymbol{n}^{tr}_{n+1} && (4.38)\\ &\tau^{e}_{n+1} = \tau^{e,tr}_{n+1} - G(c)\dot{\gamma}_{p,n+1}\Delta t && (4.39) \end{aligned}$$

Thus, as stated above, the direction of the deviatoric stress is equal to the trial direction. Furthermore, there exists a scalar equation to update the stress to the next time step value. The plastic strain rate $\dot{\gamma}_{p,n+1}$ depends on e^{xc}_{n+1} and τ^{e}_{n+1}. Thus, we also need to integrate the excess energy evolution equation 4.21. Using the implicit Euler scheme, we obtain

$$e^{xc}_{n+1} = e^{xc}_{n} + \dot{e}^{xc}\Delta t \tag{4.40}$$

Equations 4.39 and 4.41 form a nonlinear system of equations with the two unknowns τ^{e}_{n+1} and e^{xc}_{n+1}. It is convenient to represent the the unknowns in a vector $\chi = [\tau^{e}\ e^{xc}]^{T}$, and construct the following residual.

$$\boldsymbol{r}(\chi_{n+1}) = \begin{pmatrix} \tau^{e}_{n+1} - \tau^{e,tr}_{n+1} + G(c)\dot{\gamma}_{p,n+1}\Delta t \\ e^{xc}_{n+1} - e^{xc}_{n} - \dot{e}^{xc}\Delta t \end{pmatrix} \overset{!}{=} \begin{pmatrix} 0 \\ 0 \end{pmatrix} \tag{4.41}$$

An iterative Newton-Raphson scheme is set up to solve the system of nonlinear equations.

$$\chi^{i+1}_{n+1} = \chi^{i}_{n+1} - \left[\frac{\partial \boldsymbol{r}}{\partial \chi}\bigg|_{\chi^{i+1}_{n+1}} \right]^{-1} \boldsymbol{r}\left(\chi^{i+1}_{n+1}\right) \qquad \text{until} \qquad \|\boldsymbol{r}\| < tol \tag{4.42}$$

Once the nonlinear system of equations 4.42 is solved, the deviatoric part of the stress is

$$\boldsymbol{\sigma}'_{n+1} = \sqrt{2}\tau^{e}_{n+1}\boldsymbol{n}^{tr}_{n+1} \tag{4.43}$$

The next step is to find the consistent moduli $\mathbb{C}^{ep}_{n+1}$ by taking the derivative of stress with respect to stress which is needed in Eq. 4.26. We rewrite the stress in the following form to take its derivative.

$$\boldsymbol{\sigma}_{n+1} = \boldsymbol{\sigma}^{e}_{n+1} - 2\,G(c)\,\eta_{n+1}\,\boldsymbol{n}^{tr}_{n+1} \qquad \text{with} \qquad \boldsymbol{\sigma}^{e}_{n+1} = k e_{n+1}\boldsymbol{I} + \boldsymbol{\sigma}'^{,tr}_{n+1} \tag{4.44}$$

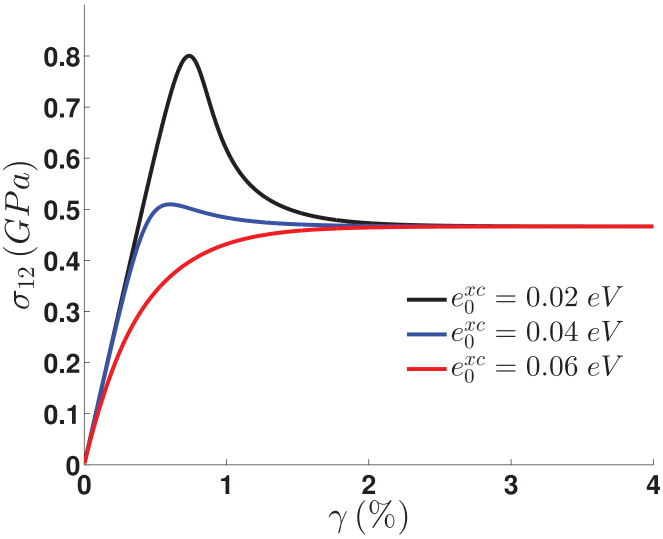

Figure 2 – Shear stress (σ_{12}) versus shear strain(γ) in LiSi nanowires with different initial excess energies. All tests are done at a strain rate of $\dot{\varepsilon} = 10^{-3}/s$ and start immediately after discharging is complete. This test is performed to check the the developed finite element code.

The consistent moduli can be found to be

$$\begin{aligned}\mathbb{C}^{ep}_{n+1} =& \frac{d\boldsymbol{\sigma}_{n+1}}{d\boldsymbol{\varepsilon}_{n+1}}\\ =& \mathbb{C}^{e}_{n+1} - 2\,G(c)\,\boldsymbol{n}^{tr}_{n+1} \otimes \frac{d\eta_{n+1}}{d\boldsymbol{\varepsilon}_{n+1}} - 2\,G(c)\,\eta_{n+1}\,\frac{d\boldsymbol{n}^{tr}_{n+1}}{d\boldsymbol{\varepsilon}_{n+1}}, \quad \text{with} \quad \mathbb{C}^{e}_{n+1} = k\boldsymbol{I}\otimes\boldsymbol{I} + 2\,G(c)\,\mathbb{P}\end{aligned} \tag{4.45}$$

$\mathbb{C}^e$ is the consistent moduli for elastic step, when the plastic strain rate vanishes. The derivatives in the Eq. 4.45 have been are shown below.

$$\frac{d\eta_{n+1}}{d\boldsymbol{\varepsilon}_{n+1}} = \frac{\sqrt{2}\,G(c)}{\tau^{e,tr}_{n+1}}\left[\mathbb{P} - \boldsymbol{n}^{tr}_{n+1}\otimes\boldsymbol{n}^{tr}_{n+1}\right] \tag{4.46}$$

$$\frac{d\boldsymbol{n}^{tr}_{n+1}}{d\boldsymbol{\varepsilon}_{n+1}} = 2\,G(c)\left[\frac{\partial \boldsymbol{r}}{\partial \chi}\bigg|_{\chi^{i+1}_{n+1}}\right]^{-1}_{[1,1]} \boldsymbol{n}^{tr}_{n+1}\otimes\boldsymbol{n}^{tr}_{n+1} \tag{4.47}$$

4.4 Testing and validating the formulation

The developed finite element formulation has been implemented using MOOSE framework [moo(2008)]. In order to verify the implemented code, we perform an element test by loading one two dimensional 4-node quadrilateral (QUAD4) element by a pure shear strain $\dot{\gamma} = 10^{-3}$. The material parameters are taken from Table 1 of Chapter 2. There rate of charging in this example is zero and the composition is Li_1Si. The model is tested with three initial values for excess energy. Figure 2 shows the evolution of shear stress vs. applied shear strain. We validated the implemented code by comparing the results in Fig. 2 with the results of a similar test shown in Fig. 4 in Chapter2.

4.4.1 Thin film charging

In this section, we are simulating a thin film during charging from $x = 1$ to $x = 2$ in Li_xSi . We take Li_1Si as the reference configuration and charge the film with three different rates. The film has a thickness of $h = 100\mu m$ and a length of $l = 1\,mm$ and we simulate it in a plane strain setting. Bottom of the film is fully fixed which models a rigid substrate and a perfect attachment of film and substrate. The schematic of the Fig. 3c shows the boundary conditions on the film. The material parameters are taken from Table 1 of Chapter 2 and we use the constant average values of material parameters throughout the simulation.

Figure 3a shows the stress development in the film for three different rates of charging, i.e. $\dot{x} = C/0.4, C/4, C/40$. Viscoplatic nature of the model along with the evolution of excess energy produces different stress levels for different rates of charging. Stresses are lower for lower rates and higher for higher rates of charging. Figure 3b depicts the evolution of excess energy during discharging. The initial excess energy for all tests is $e^{xc}_0 = 0.04eV$. Excess energy creation happens at a higher rate for higher rate of charging and vice versa. Thus excess energy steadily has higher values for higher rate of charging.

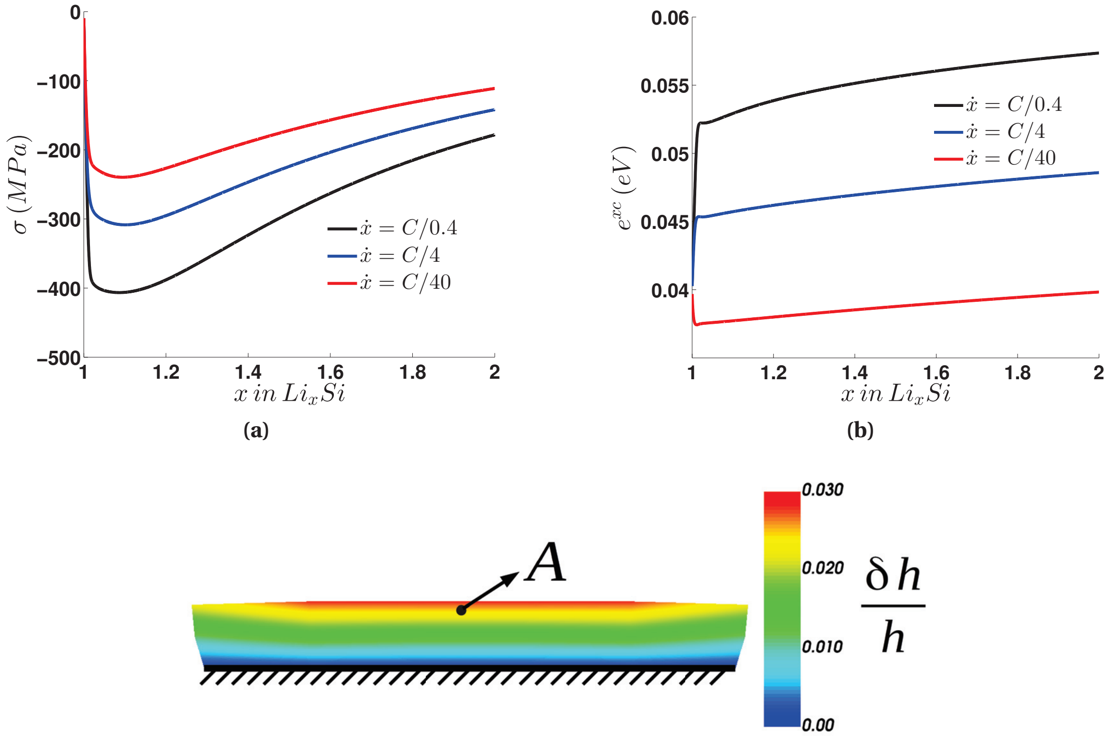

(a)

(b)

(c)

Figure 3 – a,b) FEM simulation of stress and excess energy development in a thin film during charging at point “A”shown in sub-figure (c). c) Geometry of simulated thin film and vertical expansion $\delta h/h$ of the thin film after fully charged. The lower boundary is fully clamped.

4.5 Conclusion

To employ the constitutive model developed in Chapter 2 in realistic geometries, we have developed a nonlinear finite element method which is capable of simulating chemo-mechanical systems with excess energy as an internal variable. The model is based on J_2 type plasticity. At present, the constitutive model does not explicitly address the Li diffusion through and thus diffusion is not incorporated in the FEM model. The developed code is tested and verified and the solution of the chemo-mechanical system for charging of a thin film is presented.

5 Conclusion

Lithium-ion batteries are characterized by high specific energy capacity, high operating voltage and long life[Scrosati and Garche(2010)]. Silicon has the highest known theoretical specific charge capacity in Li-ion batteries. However, the expansion/contraction of Silicon during lithiation and delithiation, introduces stresses that can drive mechanical failure and capacity fading. Furthermore, crystalline silicon undergoes a phase change from crystalline to amorphous [Limthongkul et al.(2003)Limthongkul, Jang, Dudney, and Chiang, Chon et al.(2011)Chon, Sethuraman, McCormick, Srinivasan, and Guduru, Liu et al.(2012)Liu, Liu, Kushima, Zhang, Zhu, Li, and Huang] upon first lithiation, so that stress development and failure process in subsequent charging/discharging cycles are occurring in amorphous Li_xSi alloys. Understanding the mechanics of amorphous Silicon thus becomes important to enable us to optimize the capacity and lifetime of Li-ion batteries with Silicon anodes. The mechanical properties of lithiated Silicon have been shown to be different inside and outside of an electrochemical cell[Zhao et al.(2012b)Zhao, Tritsaris, Pharr, Wang, Okeke, Suo, Vlassak, and Kaxiras]. Thus, I have specifically focused in this thesis on the effect of charging/discharging on the mechanical behavior of lithiated Silicon.

To model plasticity in Li_xSi , I have developed a mechanistically-based constitutive model for amorphous Li_xSi , based on the concept of excess energy stored in the material during charging/discharging. There are no purely phenomenological aspects in our model and aspects such as the glassy plastic flow model based on kinematic evolution of material structure could be enhanced as new understanding of glassy flow emerges. I have used molecular dynamics simulations to validate the basic premises of the model, specifically the accumulation of excess energy and associated plastic softening of the material.

The model is able to predict plastic softening as a function of the chemical and mechanical loading conditions as well as charging/discharging history of the material. One main prediction of the model is that the measured plastic flow stress is a result of the competition between excess energy creation and annihilation mechanisms. As a result of excess energy evolution, the model also predicts that the chemical potential evolves during time. This prediction may be pertinent for explaining observed phenomena and trends in recent experiments.

Specifically, the considerable amount of electrochemical potential hysteresis during charging/discharging of thin film amorphous silicon can not be fully described based only on the contribution of the stress-dependent chemical potential [Sheldon et al.(2011)Sheldon, Soni, Xiao, and Qi]. Excess energy and structural change of lithiated silicon during charging/discharging, if not annihilated within the experimental time scale, might explain the hysteresis in electrochemical potential that cannot be simply explained by stress contribution to the chemical potential. Further theoretical investigations and the design of proper experiments to verify the effects of structural change and excess energy evolution in the electrochemical potential of amorphous Li_xSi during charging/discharging remain open for future research.

The constitutive model developed here has been employed in realistic geometries using the finite element method. This enables us to capture the full complexity of coupled chemical-mechanical evolution including plastic flow that arises in these amorphous battery materials. At present, the proposed constitutive model does not explicitly address the processes of Li diffusion through the material. Thus, I did not incorporate diffusion in the finite element formulation. Diffusion processes could drive either faster relaxation or create further excess energy. The excess energy due to insertion and removal of Li might also affect the driving forces for diffusion. The change in the barriers for diffusion due to excess energy creation/annihilation may be relevant for describing the sharp interface that is observed during the charging of lithium in amorphous silicon. I propose this topic for further research.

The importance of fracture in Li_xSi as the main source of degradation and capacity fading, along with the lack of mechanistic models for the fracture of these materials in the literature, motivates the work in this thesis on modeling the fracture of lithiated silicon. Furthermore, recent experimental studies on the fracture of lithiated silicon show conflicting results [Pharr et al.(2013)Pharr, Suo, and Vlassak, Wang et al.(2015)Wang, Fan, Wang, Wang, Tao, Yang, Liu, Chew, Mao, Zhu, et al.]. I performed systematic atomistic simulations of mode I plane-strain fracture for three different as-quenched compositions ($x = 0.5$, $x = 1.0$ and $x = 1.5$ in Li_xSi), and three discharged samples ($x = 0.5$ discharged from $x_\infty = 1.0, 1.5$ and $x = 1.0$ discharged from $x_\infty = 1.5$ in Li_xSi) and analyzed the R-curves. To better understand and quantify trends in the fracture behavior, I analyzed the nano-mechanisms of fracture, which was shown to be void nucleation and coalescence for all compositions. Due to similarities of the mechanism of fracture of lithiated silicon to the ductile fracture mechanism proposed in Gurson-type models for larger-scale fracture, GTN model was used to help interpret the simulation results. I showed qualitative agreement with the GTN based fracture simulation and concluded that the ductile fracture model based on Gurson type mechanism of fracture can describe the fracture in Li_xSi during charging/discharging.

Amorphous Li_xSi ahead of the crack tip easily cavitates to form voids spaced few nanometers ahead of the crack tip. The Gurson model predicts that the toughness of the material scales with $\sigma_0 D$, and I measured the nanoscale distance from void to the crack tip, D, in MD simulations. This observation can explain very low fracture energy of lithiated silicon despite its high ductility. By scaling the yield stresses of MD to experimental values and assuming the same void spacing, fracture energies close to experimental values is predicted. I also discussed that geometry has a critical effect on fracture test results. Furthermore, discharged samples flow easier and have higher fracture energy in MD simulations. Thus not only the yield stress is a function of charging/discharging history, the fracture toughness in lithiated silicon is also a function of the charging/discharging state of the material as well as the loading rates and composition of the material. Consequently, for precise comparison of MD R-curves and the experimental fracture energies of Li_xSi , a full finite element simulation of fracture based on the GTN model enhanced by the plasticity model I proposed here to capture the dynamic change in the plastic strength, is essential. This route remains open for future research.

A Amorphous samples preparation and characterization

Molecular dynamics simulations can provide insightful information on properties of materials as well as the micro-structural changes during deformation, and enhance our understanding of the failure mechanisms. Moderate cost of computation and ability to predict complex collective behavior of atoms in an amorphous structure leads us to consider MD for the purposes of extracting properties and behavior of this alloy. To conduct MD simulations, the first thing needed is a proper interatomic potential. We have tested two types of interatomic potentials in the preparation of samples, second nearest neighbor modified embedded atom (2NN MEAM) potential [Cui et al.(2012a)Cui, Gao, Cui, and Qu] and a reactive force field (ReaxFF) potential [Zhang(2012)].

Properties which are generally needed for mechanical modeling of deformation and fracture are elastic moduli, surface energies, plastic yield stress, all vs. composition, and possibly temperature and strain rate. Extraction of desired properties requires validation and testing of interatomic potentials, and proper simulation methods. So, here we will find some properties of the alloy and they will be compared to those obtained in experiment or other simulation methods in order to validate the interatomic potential and simulation methods. Due to computational efficiency in thesis we extensively used the second nearest neighbor modified embedded atom (2NN MEAM) potential [Cui et al.(2012a)Cui, Gao, Cui, and Qu] potential for our simulations. Thus comparison of the properties obtained using this potential is essential for validating the results of plasticity and fracture simulations performed in this thesis.

A.1 Bulk properties of Li_xSi

In this section, bulk properties of Li_xSi alloys will be computed using MD simulations based on the 2NN MEAM and ReaxFF interatomic potentials and will be compared to other methods reported in the literature. The first step in MD simulation is to construct a simulation cell with atomistic structure identical to that of the material being simulated. This is usually easy for crystalline materials. However, it is not so trivial for amorphous materials. In this work, the amorphous structure is created via a rapid quench process. The temperature of an initially crystalline structure of a given composition is increased to 3000-3500 °K. The melting temperature depends on the concentration of lithium. Silicon-rich compounds have higher melting temperatures and need elevated temperatures. However, in lithium-rich compounds in order to keep the sample in the liquid phase lower temperatures should be used. Then the temperature is decreased rapidly to the desired final temperature below glass transition temperature to create an amorphous solid. Discharging at experimentally comparable low rates is computationally inaccessible. Thus we used a relatively high rate of discharging $\dot{T} = 3000\,K^o/ns$ for quenching. In crack propagation samples we used slower rate of $\dot{T} = 500\,K^o/ns$ just above glass transition temperature ($T = 700K$) to have a more relaxed sample while keeping a low computational cost. In this appendix we are only descussing the properties of the material prepared with faster quench rate of $\dot{T} = 3000\,K^o/ns$.

Rapid quenching creates an amorphous structure with desired composition. The amorphous nature of the resulted simulation cells is demonstrated by the radial distribution function (RDF). Figure 1 depicts radial distribution functions for different compositions. Simulation cells created do not show any far field correlation between atoms and also peaks for the first and second nearest neighbors are spread out. Thus, It is clearly seen that the samples created

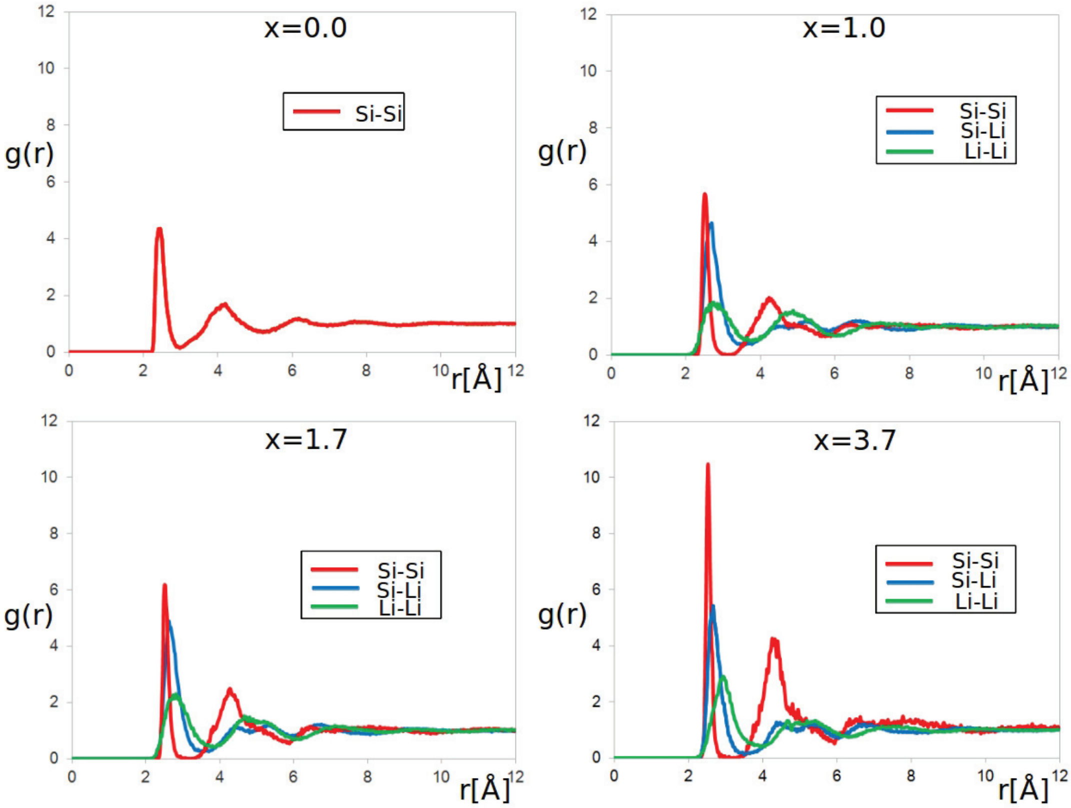

Figure 1 – The Radial distribution functions of Li$_x$Si amorphous alloys created by quenching. The variable x is the stoichiometric value in Li$_x$Si alloy. Radial distribution function are obtained at 0 °K. All these simulations have been done using LAMMPS package [lam(1995)]

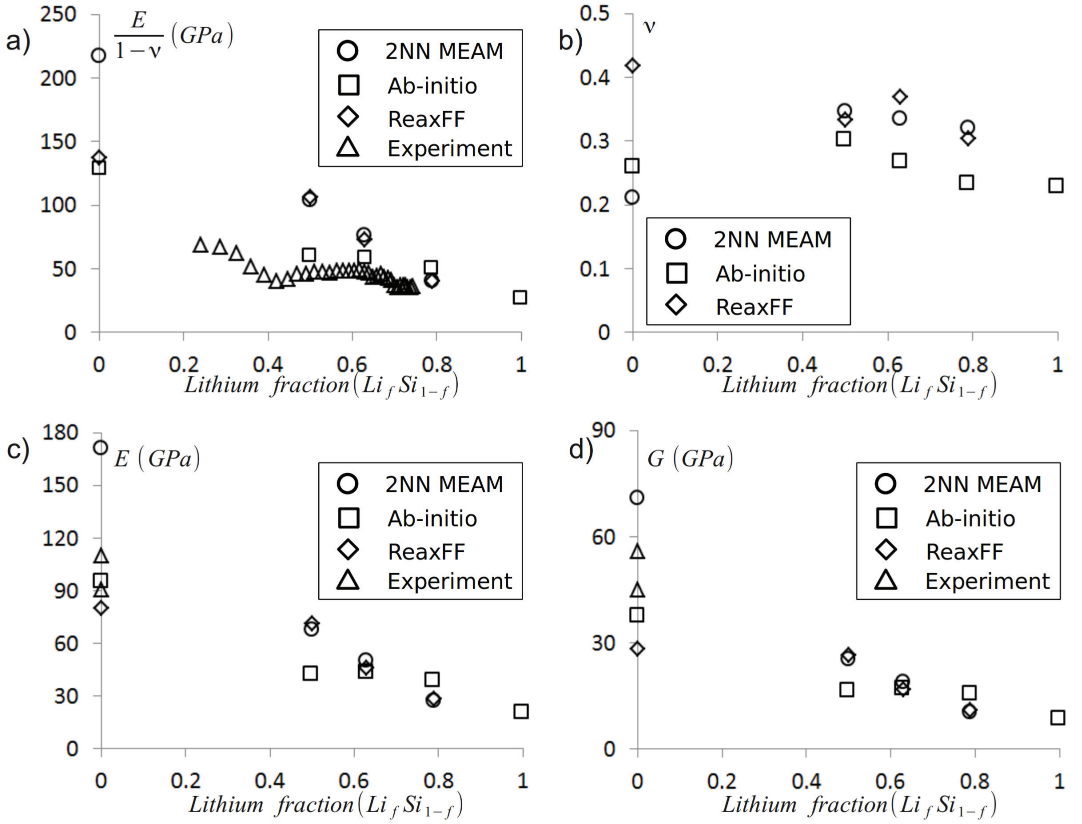

Figure 2 – (a) Biaxial moduli of lithiated silicon. Experimental results are taken from Sethuraman et al. [Sethuraman et al.(2010a)Sethuraman, Chon, Shimshak, Van Winkle, and Guduru] and Ab-initio has been reported by Shenoy et al. [Shenoy et al.(2010)Shenoy, Johari, and Qi]. (b) Poisson's ratio calculated by three methods. Ab-inition results are again from the same reference. (c) Elastic moduli experimental and numerical values. Experimental values are obtained from Searle [Searle(1998)]. (d) Shear modulus experimental and calculated values. Two values has been reported experimentally for amorphous silicon.

by the rapid quenching are indeed amorphous.

In all these alloys silicon seems to be less disordered than Li atoms. This might be due to the fact that Si atoms are still covalently bonded. The bond length for silicon in all the above alloys slightly changes from 2.35Å to 2.55Å after lithiation ($x = 3.7$) in Si-Si bonds. The first neighbor distance for lithium also varies from 2.75Å to 2.90Å for Li-Li with the increment of Li concentration. This distance remains approximately constant at 2.67Å for Li-Si in alloys with different lithium concentrations. These results are generally in a good agreement with the recent ab initio studies [Kim et al.(2011)Kim, Chou, Ekerdt, and Hwang]. It is worth noting that the final structure of amorphous alloy is sensitive to the rate of quenching. Giving more quenching time to the composition results in further local relaxation and even lower energy in the final structure. This effect has been also reported in metal amorphous alloys [Rodney and Schroder(2011)].

Elastic constants of amorphous Li_xSi alloys at 0°K are also calculated from MD simulations. Four elastic constants are shown in 2. As the system is amorphous and isotropic, only two of these constants are independent. From Fig. 2, one can see that for the crystalline systems, the biaxial, shear, and Young's moduli depend very strongly on Li concentration, showing significant softening in the lithium-rich phases. They do not generally obey a mixing rule. Specially for silicon-rich alloys, they show a deviation from the linear mixture rule for modulus. Furthermore, for silicon-rich specimens, a much larger difference can be seen between the ab-initio, experiment, and molecular dynamics results. Specially, MEAM does not work accurately for silicon-rich compositions. It should also be noted that experimental results are from room temperature experiments which generally should exhibit lower moduli compared to 0°K numerical experiments.

Bibliography

[lam(1995)] LAMMPS molecular dynamics simulator, 1995. URL http://lammps.sandia.gov/index.html.

[moo(2008)] The Multiphysics Object-Oriented Simulation Environment, 2008. URL http://mooseframework.org.

[Argon(1979)] A.S Argon. Plastic deformation in metallic glasses. *Acta Metallurgica*, 27(1):47–58, January 1979. ISSN 0001-6160. doi: 10.1016/0001-6160(79)90055-5. URL http://www.sciencedirect.com/science/article/pii/0001616079900555.

[Beaulieu et al.(2003)Beaulieu, Hatchard, Bonakdarpour, Fleischauer, and Dahn] L. Y. Beaulieu, T. D. Hatchard, A. Bonakdarpour, M. D. Fleischauer, and J. R. Dahn. Reaction of li with alloy thin films studied by in situ AFM. *Journal of The Electrochemical Society*, 150(11):A1457–A1464, November 2003. ISSN 0013-4651, 1945-7111. doi: 10.1149/1.1613668. URL http://jes.ecsdl.org/content/150/11/A1457.

[Bower and Guduru(2012a)] A. F. Bower and P. R. Guduru. A simple finite element model of diffusion, finite deformation, plasticity and fracture in lithium ion insertion electrode materials. *Modelling and Simulation in Materials Science and Engineering*, 20(4):045004, June 2012a. ISSN 0965-0393. doi: 10.1088/0965-0393/20/4/045004. URL http://iopscience.iop.org/0965-0393/20/4/045004.

[Bower and Guduru(2012b)] AF Bower and PR Guduru. A simple finite element model of diffusion, finite deformation, plasticity and fracture in lithium ion insertion electrode materials. *Modelling and Simulation in Materials Science and Engineering*, 20(4):045004, 2012b.

[Bower et al.(2011)Bower, Guduru, and Sethuraman] A.F. Bower, P.R. Guduru, and V.A. Sethuraman. A finite strain model of stress, diffusion, plastic flow, and electrochemical reactions in a lithium-ion half-cell. *Journal of the Mechanics and Physics of Solids*, 59(4):804–828, April 2011. ISSN 0022-5096. doi: 10.1016/j.jmps.2011.01.003. URL http://www.sciencedirect.com/science/article/pii/S0022509611000044.

[Bower(2009)] Allan F Bower. *Applied mechanics of solids*. CRC press, 2009.

[Brassart and Suo(2012)] Laurence Brassart and Zhigang Suo. Reactive flow in large-deformation electrodes of lithium-ion batteries. *International Journal of Applied Mechanics*, 04(03):1250023, September 2012. ISSN 1758-8251, 1758-826X. doi: 10.1142/S1758825112500238. URL http://www.worldscientific.com/doi/abs/10.1142/S1758825112500238?af=R.

[Chan et al.(2008)Chan, Peng, Liu, McIlwrath, Zhang, Huggins, and Cui] Candace K. Chan, Hailin Peng, Gao Liu, Kevin McIlwrath, Xiao Feng Zhang, Robert A. Huggins, and Yi Cui. High performance lithium battery anodes using silicon nanowires. *Nature Nanotechnology*, 3(1):31–35, January 2008. ISSN 1748-3387. doi: 10.1038/nnano.2007.411. URL http://www.nature.com/nnano/journal/v3/n1/full/nnano.2007.411.html.

[Cheng and Verbrugge(2009)] Yang-Tse Cheng and Mark W. Verbrugge. Evolution of stress within a spherical insertion electrode particle under potentiostatic and galvanostatic operation. *Journal of Power Sources*, 190(2):453–460, May 2009. ISSN 0378-7753. doi: 10.1016/j.jpowsour.2009.01.021. URL http://www.sciencedirect.com/science/article/pii/S0378775309000639.

[Cheng and Verbrugge(2010)] Yang-Tse Cheng and Mark W. Verbrugge. Diffusion-induced stress, interfacial charge transfer, and criteria for avoiding crack initiation of electrode particles. *Journal of The Electrochemical Society*, 157(4):A508–A516, April 2010. ISSN 0013-4651, 1945-7111. doi: 10.1149/1.3298892. URL http://jes.ecsdl.org/content/157/4/A508.

[Chevrier and Dahn(2009)] V. L. Chevrier and J. R. Dahn. First principles model of amorphous silicon lithiation. *Journal of The Electrochemical Society*, 156(6):A454–A458, June 2009. ISSN 0013-4651, 1945-7111. doi: 10.1149/1.3111037. URL http://jes.ecsdl.org/content/156/6/A454.

[Chon et al.(2011)Chon, Sethuraman, McCormick, Srinivasan, and Guduru] M. J. Chon, V. A. Sethuraman, A. McCormick, V. Srinivasan, and P. R. Guduru. Real-time measurement of stress and damage evolution during initial lithiation of crystalline silicon. *Physical Review Letters*, 107(4):045503, July 2011. doi: 10.1103/PhysRevLett.107.045503. URL http://link.aps.org/doi/10.1103/PhysRevLett.107.045503.

[Christensen and Newman(2006)] John Christensen and John Newman. Stress generation and fracture in lithium insertion materials. *Journal of Solid State Electrochemistry*, 10(5):293–319, May 2006. ISSN 1432-8488, 1433-0768. doi: 10.1007/s10008-006-0095-1. URL http://link.springer.com/article/10.1007/s10008-006-0095-1.

[Chung et al.(2011)Chung, Seo, Zhang, and Sastry] M. D. Chung, J. H. Seo, X. C. Zhang, and A. M. Sastry. Implementing realistic geometry and measured diffusion coefficients into single particle electrode modeling based on experiments with single LiMn2O4 spinel particles. *Journal of The Electrochemical Society*, 158(4):A371–A378, April 2011. ISSN 0013-4651, 1945-7111. doi: 10.1149/1.3549161. URL http://jes.ecsdl.org/content/158/4/A371.

[Cui et al.(2009)Cui, Ruffo, Chan, Peng, and Cui] L.-F. Cui, R. Ruffo, C.K. Chan, H. Peng, and Y. Cui. Crystalline-amorphous core-shell silicon nanowires for high capacity and high current battery electrodes. *Nano Letters*, 9(1):491–495, 2009. ISSN 15306984. doi: 10.1021/nl8036323.

[Cui et al.(2012a)Cui, Gao, Cui, and Qu] Zhiwei Cui, Feng Gao, Zhihua Cui, and Jianmin Qu. A second nearest-neighbor embedded atom method interatomic potential for li-si alloys. *Journal of Power Sources*, 207:150–159, June 2012a. ISSN 0378-7753. doi: 10.1016/j.jpowsour.2012.01.145. URL http://www.sciencedirect.com/science/article/pii/S0378775312002911.

[Cui et al.(2012b)Cui, Gao, and Qu] Zhiwei Cui, Feng Gao, and Jianmin Qu. A finite deformation stress-dependent chemical potential and its applications to lithium ion batteries. *Journal of the Mechanics and Physics of Solids*, 60(7):1280–1295, July 2012b. ISSN 0022-5096. doi: 10.1016/j.jmps.2012.03.008. URL http://www.sciencedirect.com/science/article/pii/S0022509612000622.

[Dal and Miehe(2015)] Hüsnü Dal and Christian Miehe. Computational electro-chemo-mechanics of lithium-ion battery electrodes at finite strains. *Computational Mechanics*, 55(2):303–325, 2015.

[Faleskog et al.(1998)Faleskog, Gao, and Shih] Jonas Faleskog, Xiaosheng Gao, and C Fong Shih. Cell model for nonlinear fracture analysis–i. micromechanics calibration. *International Journal of Fracture*, 89(4):355–373, 1998.

[Falk and Langer(1998)] M. L. Falk and J. S. Langer. Dynamics of viscoplastic deformation in amorphous solids. *Phys. Rev. E*, 57:7192–7205, Jun 1998. doi: 10.1103/PhysRevE.57.7192. URL http://link.aps.org/doi/10.1103/PhysRevE.57.7192.

[Garcia et al.(2005)Garcia, Chiang, Carter, Limthongkul, and Bishop] R. Edwin Garcia, Yet-Ming Chiang, W. Craig Carter, Pimpa Limthongkul, and Catherine M. Bishop. Microstructural modeling and design of rechargeable lithium-ion batteries. *Journal of The Electrochemical Society*, 152(1):A255–A263, January 2005. ISSN 0013-4651, 1945-7111. doi: 10.1149/1.1836132. URL http://jes.ecsdl.org/content/152/1/A255.

[Goldman et al.(2011)Goldman, Long, Gewirth, and Nuzzo] Jason L. Goldman, Brandon R. Long, Andrew A. Gewirth, and Ralph G. Nuzzo. Strain anisotropies and self-limiting capacities in single-crystalline 3D silicon microstructures: Models for high energy density lithium-ion battery anodes. *Advanced Functional Materials*, 21(13):2412–2422, 2011. ISSN 1616-3028. doi: 10.1002/adfm.201002487. URL http://onlinelibrary.wiley.com/doi/10.1002/adfm.201002487/abstract.

[Golmon et al.(2009)Golmon, Maute, and Dunn] Stephanie Golmon, Kurt Maute, and Martin L. Dunn. Numerical modeling of electrochemical-mechanical interactions in lithium polymer batteries. *Computers & Structures*, 87(23–24):1567–1579, December 2009. ISSN

0045-7949. doi: 10.1016/j.compstruc.2009.08.005. URL http://www.sciencedirect.com/science/article/pii/S0045794909002053.

[Graetz et al.(2003)Graetz, Ahn, Yazami, and Fultz] J. Graetz, C. C. Ahn, R. Yazami, and B. Fultz. Highly reversible lithium storage in nanostructured silicon. *Electrochemical and Solid-State Letters*, 6(9):A194–A197, September 2003. ISSN 1099-0062, 1944-8775. doi: 10.1149/1.1596917. URL http://esl.ecsdl.org/content/6/9/A194.

[Gurson(1977)] Arthur L Gurson. Continuum theory of ductile rupture by void nucleation and growth: Part i—yield criteria and flow rules for porous ductile media. *Journal of engineering materials and technology*, 99(1):2–15, 1977.

[Hun et al.(2011)Hun, Chung, Park, Woo, Zhang, and Marie] Jeong Hun, Myoungdo Chung, Myounggu Park, Sang Woo, Xiangchun Zhang, and Ann Marie. Generation of realistic particle structures and simulations of internal stress: A Numerical/AFM study of LiMn2O4 particles. *Journal of The Electrochemical Society*, 158(4):A434–A442, April 2011. ISSN 0013-4651, 1945-7111. doi: 10.1149/1.3552930. URL http://jes.ecsdl.org/content/158/4/A434.

[Hutchinson(1983)] JWt Hutchinson. Fundamentals of the phenomenological theory of nonlinear fracture mechanics. *Journal of Applied Mechanics*, 50(4b):1042–1051, 1983.

[Hwang et al.(2001)Hwang, Lee, Jang, Lee, Lee, Baik, and Lee] Sung-Min Hwang, Heon-Young Lee, Serk-Won Jang, Sung-Man Lee, Seung-Joo Lee, Hong-Koo Baik, and Jai-Young Lee. Lithium insertion in SiAg powders produced by mechanical alloying. *Electrochemical and Solid-State Letters*, 4(7):A97–A100, July 2001. ISSN 1099-0062, 1944-8775. doi: 10.1149/1.1375176. URL http://esl.ecsdl.org/content/4/7/A97.

[Ji et al.(2011)Ji, Ma, and Lee] Ge Ji, Yue Ma, and Jim Yang Lee. Mitigating the initial capacity loss (ICL) problem in high-capacity lithium ion battery anode materials. *Journal of Materials Chemistry*, 21(27):9819–9824, June 2011. ISSN 1364-5501. doi: 10.1039/C0JM03759A. URL http://pubs.rsc.org/en/content/articlelanding/2011/jm/c0jm03759a.

[Kang et al.(2010)Kang, Lee, Han, Kim, Lee, Lee, Kang, and Jo] Kibum Kang, Hyun-Seung Lee, Dong-Wook Han, Gil-Sung Kim, Donghun Lee, Geunhee Lee, Yong-Mook Kang, and Moon-Ho Jo. Maximum li storage in si nanowires for the high capacity three-dimensional li-ion battery. *Applied Physics Letters*, 96(5):053110, 2010. ISSN 00036951. doi: 10.1063/1.3299006. URL http://link.aip.org/link/APPLAB/v96/i5/p053110/s1&Agg=doi.

[Key et al.(2009)Key, Bhattacharyya, Morcrette, Seznec, Tarascon, and Grey] Baris Key, Rangeet Bhattacharyya, Mathieu Morcrette, Vincent Seznec, Jean-Marie Tarascon, and Clare P. Grey. Real-time NMR investigations of structural changes in silicon electrodes for lithium-ion batteries. *Journal of the American Chemical Society*, 131(26):9239–9249, July 2009. ISSN 0002-7863. doi: 10.1021/ja8086278. URL http://dx.doi.org/10.1021/ja8086278.

[Key et al.(2011)Key, Morcrette, Tarascon, and Grey] Baris Key, Mathieu Morcrette, Jean-Marie Tarascon, and Clare P. Grey. Pair distribution function analysis and solid state NMR studies of silicon electrodes for lithium ion batteries: Understanding the (de)lithiation mechanisms. *Journal of the American Chemical Society*, 133(3):503–512, January 2011. ISSN 0002-7863. doi: 10.1021/ja108085d. URL http://dx.doi.org/10.1021/ja108085d.

[Khosrownejad and Curtin(2016)] SM Khosrownejad and WA Curtin. Model for charge/discharge-rate-dependent plastic flow in amorphous battery materials. *Journal of the Mechanics and Physics of Solids*, 94:167–180, 2016.

[Kim et al.(2011)Kim, Chou, Ekerdt, and Hwang] Hyunwoo Kim, Chia-Yun Chou, John G. Ekerdt, and Gyeong S. Hwang. Structure and properties of li-si alloys: A first-principles study. *The Journal of Physical Chemistry C*, 115(5):2514–2521, February 2011. ISSN 1932-7447. doi: 10.1021/jp1083899. URL http://dx.doi.org/10.1021/jp1083899.

[Kocks et al.(1975)Kocks, Argon, and Ashby] U.F. Kocks, A. S. Argon, and M. F. Ashby. Thermodynamics and kinetics of slip. *Progress in Materials Science*, 19(0):171–229, 1975. ISSN 0079-6425. doi: http://dx.doi.org/10.1016/0079-6425(75)90001-8. URL http://www.sciencedirect.com/science/article/pii/0079642575900018.

[Langer and Pechenik(2003)] JS Langer and L Pechenik. Dynamics of shear-transformation zones in amorphous plasticity: Energetic constraints in a minimal theory. *Physical Review E*, 68(6):061507, 2003.

[Lee and Lee(2002)] Heon-Young Lee and Sung-Man Lee. Graphite-FeSi alloy composites as anode materials for rechargeable lithium batteries. *Journal of Power Sources*, 112(2): 649–654, November 2002. ISSN 0378-7753. doi: 10.1016/S0378-7753(02)00461-5. URL http://www.sciencedirect.com/science/article/pii/S0378775302004615.

[Lee et al.(2011)Lee, McDowell, Choi, and Cui] Seok Woo Lee, Matthew T. McDowell, Jang Wook Choi, and Yi Cui. Anomalous shape changes of silicon nanopillars by electrochemical lithiation. *Nano Letters*, 11(7):3034–3039, July 2011. ISSN 1530-6984. doi: 10.1021/nl201787r. URL http://dx.doi.org/10.1021/nl201787r.

[Lee et al.(2001)Lee, Lee, Chung, Lee, Lee, and Baik] Seung-Joo Lee, Jong-Ki Lee, Sang-Hun Chung, Heon-Young Lee, Sung-Man Lee, and Hong-Koo Baik. Stress effect on cycle properties of the silicon thin-film anode. *Journal of Power Sources*, 97-98:191–193, July 2001. ISSN 0378-7753. doi: 10.1016/S0378-7753(01)00761-3. URL http://www.sciencedirect.com/science/article/pii/S0378775301007613.

[Levitas and Attariani(2013)] Valery I. Levitas and Hamed Attariani. Anisotropic compositional expansion and chemical potential for amorphous lithiated silicon under stress tensor. *Scientific Reports*, 3, April 2013. doi: 10.1038/srep01615. URL http://www.nature.com/srep/2013/130408/srep01615/full/srep01615.html?WT.ec_id=SREP-20130409.

[Li et al.(2000)Li, Huang, Chen, Zhou, Zhang, Yu, Jun Mo, and Pei] Hong Li, Xuejie Huang, Liquan Chen, Guangwen Zhou, Ze Zhang, Dapeng Yu, Yu Jun Mo, and Ning Pei. The crystal structural evolution of nano-si anode caused by lithium insertion and extraction at room temperature. *Solid State Ionics*, 135(1–4):181–191, November 2000. ISSN 0167-2738. doi: 10.1016/S0167-2738(00)00362-3. URL http://www.sciencedirect.com/science/article/pii/S0167273800003623.

[Liang et al.(2013)Liang, Yang, Fan, Liu, Liu, Huang, Zhu, and Zhang] Wentao Liang, Hui Yang, Feifei Fan, Yang Liu, Xiao Hua Liu, Jian Yu Huang, Ting Zhu, and Sulin Zhang. Tough germanium nanoparticles under electrochemical cycling. *Acs Nano*, 7(4):3427–3433, 2013.

[Lim et al.(2014)Lim, Liu, Cui, and Toney] Linda Y Lim, Nian Liu, Yi Cui, and Michael F Toney. Understanding phase transformation in crystalline germanium anodes for li-ion batteries. *Chemistry of Materials*, 26(12):3739–3746, 2014.

[Limthongkul et al.(2003)Limthongkul, Jang, Dudney, and Chiang] Pimpa Limthongkul, Young-Il Jang, Nancy J. Dudney, and Yet-Ming Chiang. Electrochemically-driven solid-state amorphization in lithium-silicon alloys and implications for lithium storage. *Acta Materialia*, 51(4):1103–1113, February 2003. ISSN 1359-6454. doi: 10.1016/S1359-6454(02)00514-1. URL http://www.sciencedirect.com/science/article/pii/S1359645402005141.

[Liu et al.(2011)Liu, Zheng, Zhong, Huang, Karki, Zhang, Liu, Kushima, Liang, Wang, et al.] Xiao Hua Liu, He Zheng, Li Zhong, Shan Huang, Khim Karki, Li Qiang Zhang, Yang Liu, Akihiro Kushima, Wen Tao Liang, Jiang Wei Wang, et al. Anisotropic swelling and fracture of silicon nanowires during lithiation. *Nano letters*, 11(8):3312–3318, 2011.

[Liu et al.(2012)Liu, Liu, Kushima, Zhang, Zhu, Li, and Huang] Xiao Hua Liu, Yang Liu, Akihiro Kushima, Sulin Zhang, Ting Zhu, Ju Li, and Jian Yu Huang. In situ TEM experiments of electrochemical lithiation and delithiation of individual nanostructures. *Advanced Energy Materials*, 2(7):722–741, 2012. ISSN 1614-6840. doi: 10.1002/aenm.201200024. URL http://onlinelibrary.wiley.com/doi/10.1002/aenm.201200024/abstract.

[Nakamura and Kamath(1992)] Toshio Nakamura and Sundar M Kamath. Three-dimensional effects in thin film fracture mechanics. *Mechanics of Materials*, 13(1):67–77, 1992.

[Needleman et al.(1992)Needleman, Tvergaard, and Hutchinson] A Needleman, V Tvergaard, and JW Hutchinson. Void growth in plastic solids. In *Topics in Fracture and Fatigue*, pages 145–178. Springer, 1992.

[Obrovac et al.(2007)Obrovac, Christensen, Le, and Dahn] M. N. Obrovac, Leif Christensen, Dinh Ba Le, and J. R. Dahn. Alloy design for lithium-ion battery anodes. *Journal of The Electrochemical Society*, 154(9):A849–A855, September 2007. ISSN 0013-4651, 1945-7111. doi: 10.1149/1.2752985. URL http://jes.ecsdl.org/content/154/9/A849.

[Ono et al.(2002)Ono, O'Hern, Durian, Langer, Liu, and Nagel] Ian K. Ono, Corey S. O'Hern, D. J. Durian, Stephen A. Langer, Andrea J. Liu, and Sidney R. Nagel. Effective Temperatures of a Driven System Near Jamming. *Physical Review Letters*, 89(9):095703, August 2002.

ISSN 0031-9007. doi: 10.1103/PhysRevLett.89.095703. URL http://link.aps.org/doi/10.1103/PhysRevLett.89.095703.

[Pan et al.(2008)Pan, Inoue, Sakurai, and Chen] D Pan, A Inoue, T Sakurai, and MW Chen. Experimental characterization of shear transformation zones for plastic flow of bulk metallic glasses. *Proceedings of the National Academy of Sciences*, 105(39):14769–14772, 2008.

[Pardoen and Hutchinson(2003)] Thomas Pardoen and JW Hutchinson. Micromechanics-based model for trends in toughness of ductile metals. *Acta Materialia*, 51(1):133–148, 2003.

[Park et al.(2011)Park, Lu, and Sastry] Jonghyun Park, Wei Lu, and Ann Marie Sastry. Numerical simulation of stress evolution in lithium manganese dioxide particles due to coupled phase transition and intercalation. *Journal of The Electrochemical Society*, 158 (2):A201–A206, February 2011. ISSN 0013-4651, 1945-7111. doi: 10.1149/1.3526597. URL http://jes.ecsdl.org/content/158/2/A201.

[Pharr et al.(2013)Pharr, Suo, and Vlassak] Matt Pharr, Zhigang Suo, and Joost J Vlassak. Measurements of the fracture energy of lithiated silicon electrodes of li-ion batteries. *Nano letters*, 13(11):5570–5577, 2013.

[Quinn and Bradt(2007)] George D Quinn and Richard C Bradt. On the vickers indentation fracture toughness test. *Journal of the American Ceramic Society*, 90(3):673–680, 2007.

[Rhodes et al.(2010)Rhodes, Dudney, Lara-Curzio, and Daniel] Kevin Rhodes, Nancy Dudney, Edgar Lara-Curzio, and Claus Daniel. Understanding the degradation of silicon electrodes for lithium-ion batteries using acoustic emission. *Journal of The Electrochemical Society*, 157(12):A1354–A1360, December 2010. ISSN 0013-4651, 1945-7111. doi: 10.1149/1.3489374. URL http://jes.ecsdl.org/content/157/12/A1354.

[Rice(1968)] James R Rice. Mathematical analysis in the mechanics of fracture. *Fracture: an advanced treatise*, 2:191–311, 1968.

[Rodney and Schroder(2011)] D Rodney and T Schroder. On the potential energy landscape of supercooled liquids and glasses. *The European physical journal. E, Soft matter*, 34 (9):100, September 2011. ISSN 1292-895X. doi: 10.1140/epje/i2011-11100-2. PMID: 21947901.

[Rodney et al.(2011)Rodney, Tanguy, and Vandembroucq] D. Rodney, A. Tanguy, and D. Vandembroucq. Modeling the mechanics of amorphous solids at different length scale and time scale. *Modelling and Simulation in Materials Science and Engineering*, 19(8): 083001, December 2011. ISSN 0965-0393. doi: 10.1088/0965-0393/19/8/083001. URL http://iopscience.iop.org/0965-0393/19/8/083001.

[Scrosati and Garche(2010)] Bruno Scrosati and Jürgen Garche. Lithium batteries: Status, prospects and future. *Journal of Power Sources*, 195(9):2419–2430, May 2010. ISSN 0378-7753. doi: 10.1016/j.jpowsour.2009.11.048. URL http://www.sciencedirect.com/science/article/pii/S0378775309020564.

[Searle(1998)] Tim Searle. *Properties of amorphous silicon and its alloys*. INSPEC, 1998. ISBN 9780852969229.

[Sethuraman et al.(2010a)Sethuraman, Chon, Shimshak, Van Winkle, and Guduru] V.A. Sethuraman, M.J. Chon, M. Shimshak, N. Van Winkle, and P.R. Guduru. In situ measurement of biaxial modulus of si anode for li-ion batteries. *Electrochemistry Communications*, 12(11):1614–1617, November 2010a. ISSN 1388-2481. doi: 10.1016/j.elecom.2010.09.008. URL http://www.sciencedirect.com/science/article/pii/S1388248110003929.

[Sethuraman et al.(2012)Sethuraman, Van Winkle, Abraham, Bower, and Guduru] V.A. Sethuraman, N. Van Winkle, D.P. Abraham, A.F. Bower, and P.R. Guduru. Real-time stress measurements in lithium-ion battery negative-electrodes. *Journal of Power Sources*, 206:334–342, May 2012. ISSN 0378-7753. doi: 10.1016/j.jpowsour.2012.01.036. URL http://www.sciencedirect.com/science/article/pii/S0378775312000730.

[Sethuraman et al.(2010b)Sethuraman, Chon, Shimshak, Srinivasan, and Guduru] Vijay A. Sethuraman, Michael J. Chon, Maxwell Shimshak, Venkat Srinivasan, and Pradeep R. Guduru. In situ measurements of stress evolution in silicon thin films during electrochemical lithiation and delithiation. *Journal of Power Sources*, 195(15):5062–5066, August 2010b. ISSN 0378-7753. doi: 10.1016/j.jpowsour.2010.02.013. URL http://www.sciencedirect.com/science/article/pii/S0378775310002582.

[Sheldon and Curtin(2004)] Brian W Sheldon and William A Curtin. Nanoceramic composites: tough to test. *Nature materials*, 3(8):505–506, 2004.

[Sheldon et al.(2011)Sheldon, Soni, Xiao, and Qi] Brian W Sheldon, Sumit K Soni, Xingcheng Xiao, and Yue Qi. Stress contributions to solution thermodynamics in li-si alloys. *Electrochemical and Solid-State Letters*, 15(1):A9–A11, 2011.

[Shenoy et al.(2010)Shenoy, Johari, and Qi] V.B. Shenoy, P. Johari, and Y. Qi. Elastic softening of amorphous and crystalline li-si phases with increasing li concentration: A first-principles study. *Journal of Power Sources*, 195(19):6825–6830, October 2010. ISSN 0378-7753. doi: 10.1016/j.jpowsour.2010.04.044. URL http://www.sciencedirect.com/science/article/pii/S0378775310006798.

[Soni et al.(2011)Soni, Sheldon, Xiao, and Tokranov] Sumit K. Soni, Brian W. Sheldon, Xingcheng Xiao, and Anton Tokranov. Thickness effects on the lithiation of amorphous silicon thin films. *Scripta Materialia*, 64(4):307–310, February 2011. ISSN 1359-6462. doi: 10.1016/j.scriptamat.2010.10.003. URL http://www.sciencedirect.com/science/article/pii/S1359646210006846.

[Spaepen(1977)] Frans Spaepen. A microscopic mechanism for steady state inhomogeneous flow in metallic glasses. *Acta Metallurgica*, 25(4):407–415, April 1977. ISSN 0001-6160. doi: 10.1016/0001-6160(77)90232-2. URL http://www.sciencedirect.com/science/article/pii/0001616077902322.

[Steif et al.(1982)Steif, Spaepen, and Hutchinson] P.S. Steif, F. Spaepen, and J.W. Hutchinson. Strain localization in amorphous metals. *Acta Metallurgica*, 30(2):447–455, February 1982. ISSN 0001-6160. doi: 10.1016/0001-6160(82)90225-5. URL http://www.sciencedirect.com/science/article/pii/0001616082902255.

[Tvergaard and Hutchinson(1992)] Viggo Tvergaard and John W Hutchinson. The relation between crack growth resistance and fracture process parameters in elastic-plastic solids. *Journal of the Mechanics and Physics of Solids*, 40(6):1377–1397, 1992.

[Vadillo and Fernández-Sáez(2009)] Guadalupe Vadillo and José Fernández-Sáez. An analysis of gurson model with parameters dependent on triaxiality based on unitary cells. *European Journal of Mechanics-A/Solids*, 28(3):417–427, 2009.

[Verbrugge and Cheng(2008)] Mark Verbrugge and Yang-Tse Cheng. Stress distribution within spherical particles undergoing electrochemical insertion and extraction. *ECS Transactions*, 16(13):127–139, October 2008. ISSN 1938-6737, 1938-5862. doi: 10.1149/1.2987765. URL http://ecst.ecsdl.org/content/16/13/127.

[Verbrugge and Cheng(2009)] Mark W. Verbrugge and Yang-Tse Cheng. Stress and strain-energy distributions within diffusion-controlled insertion-electrode particles subjected to periodic potential excitations. *Journal of The Electrochemical Society*, 156(11):A927–A937, November 2009. ISSN 0013-4651, 1945-7111. doi: 10.1149/1.3205485. URL http://jes.ecsdl.org/content/156/11/A927.

[Wang and Sastry(2007)] Chia-Wei Wang and Ann Marie Sastry. Mesoscale modeling of a li-ion polymer cell. *Journal of The Electrochemical Society*, 154(11):A1035–A1047, November 2007. ISSN 0013-4651, 1945-7111. doi: 10.1149/1.2778285. URL http://jes.ecsdl.org/content/154/11/A1035.

[Wang et al.(2013)Wang, He, Fan, Liu, Xia, Liu, Harris, Li, Huang, Mao, and Zhu] Jiang Wei Wang, Yu He, Feifei Fan, Xiao Hua Liu, Shuman Xia, Yang Liu, C. Thomas Harris, Hong Li, Jian Yu Huang, Scott X. Mao, and Ting Zhu. Two-phase electrochemical lithiation in amorphous silicon. *Nano Letters*, 13(2):709–715, February 2013. ISSN 1530-6984. doi: 10.1021/nl304379k. URL http://dx.doi.org/10.1021/nl304379k.

[Wang et al.(2004)Wang, Padture, and Tanaka] Xiaotong Wang, Nitin P Padture, and Hidehiko Tanaka. Contact-damage-resistant ceramic/single-wall carbon nanotubes and ceramic/-graphite composites. *Nature materials*, 3(8):539–544, 2004.

[Wang et al.(2015)Wang, Fan, Wang, Wang, Tao, Yang, Liu, Chew, Mao, Zhu, et al.] Xueju Wang, Feifei Fan, Jiangwei Wang, Haoran Wang, Siyu Tao, Avery Yang, Yang Liu, Huck Beng Chew, Scott X Mao, Ting Zhu, et al. High damage tolerance of electrochemically lithiated silicon. *Nature communications*, 6, 2015.

[Wen and Huggins(1981)] C. John Wen and Robert A. Huggins. Chemical diffusion in intermediate phases in the lithium-silicon system. *Journal of Solid State Chemistry*, 37 (3):271–278, May 1981. ISSN 0022-4596. doi: 10.1016/0022-4596(81)90487-4. URL http://www.sciencedirect.com/science/article/pii/0022459681904874.

[Weydanz et al.(1999)Weydanz, Wohlfahrt-Mehrens, and Huggins] W.J Weydanz, M Wohlfahrt-Mehrens, and R.A Huggins. A room temperature study of the binary lithium-silicon and the ternary lithium-chromium-silicon system for use in rechargeable lithium batteries. *Journal of Power Sources*, 81-82:237–242, September 1999. ISSN 0378-7753. doi: 10.1016/S0378-7753(99)00139-1. URL http://www.sciencedirect.com/science/article/pii/S0378775399001391.

[Winter and Besenhard(1999)] Martin Winter and Jürgen O. Besenhard. Electrochemical lithiation of tin and tin-based intermetallics and composites. *Electrochimica Acta*, 45 (1–2):31–50, September 1999. ISSN 0013-4686. doi: 10.1016/S0013-4686(99)00191-7. URL http://www.sciencedirect.com/science/article/pii/S0013468699001917.

[Xia and Shih(1995a)] Lin Xia and C Fong Shih. Ductile crack growth-i. a numerical study using computational cells with microstructurally-based length scales. *Journal of the Mechanics and Physics of Solids*, 43(2):233–259, 1995a.

[Xia and Shih(1995b)] Lin Xia and C Fong Shih. Ductile crack growth—ii. void nucleation and geometry effects on macroscopic fracture behavior. *Journal of the Mechanics and Physics of Solids*, 43(12):1953–1981, 1995b.

[Yang et al.(2012)Yang, Huang, Huang, Fan, Liang, Liu, Chen, Huang, Li, Zhu, and Zhang] Hui Yang, Shan Huang, Xu Huang, Feifei Fan, Wentao Liang, Xiao Hua Liu, Long-Qing Chen, Jian Yu Huang, Ju Li, Ting Zhu, and Sulin Zhang. Orientation-dependent interfacial mobility governs the anisotropic swelling in lithiated silicon nanowires. *Nano Letters*, 12(4):1953–1958, April 2012. ISSN 1530-6984. doi: 10.1021/nl204437t. URL http://dx.doi.org/10.1021/nl204437t.

[Yang et al.(2003)Yang, Wang, Wang, Liu, Xie, and Wen] J. Yang, B. F. Wang, K. Wang, Y. Liu, J. Y. Xie, and Z. S. Wen. Si/C composites for high capacity lithium storage materials. *Electrochemical and Solid-State Letters*, 6(8):A154–A156, August 2003. ISSN 1099-0062, 1944-8775. doi: 10.1149/1.1585251. URL http://esl.ecsdl.org/content/6/8/A154.

[Zhang(2012)] Sulin Zhang. Suitable ReaxFF potential for li-si systems, private communication, 2012.

[Zhang et al.(2007)Zhang, Shyy, and Sastry] Xiangchun Zhang, Wei Shyy, and Ann Marie Sastry. Numerical simulation of intercalation-induced stress in li-ion battery electrode particles. *Journal of The Electrochemical Society*, 154(10):A910–A916, October 2007. ISSN 0013-4651, 1945-7111. doi: 10.1149/1.2759840. URL http://jes.ecsdl.org/content/154/10/A910.

[Zhao et al.(2011a)Zhao, Pharr, Cai, Vlassak, and Suo] Kejie Zhao, Matt Pharr, Shengqiang Cai, Joost J. Vlassak, and Zhigang Suo. Large plastic deformation in high-capacity lithium-ion batteries caused by charge and discharge. *Journal of the American Ceramic Society*, 94:s226–s235, 2011a. ISSN 1551-2916. doi: 10.1111/j.1551-2916.2011.04432.x. URL http://onlinelibrary.wiley.com/doi/10.1111/j.1551-2916.2011.04432.x/abstract.

[Zhao et al.(2011b)Zhao, Wang, Gregoire, Pharr, Suo, Vlassak, and Kaxiras] Kejie Zhao, Wei L. Wang, John Gregoire, Matt Pharr, Zhigang Suo, Joost J. Vlassak, and Efthimios Kaxiras. Lithium-assisted plastic deformation of silicon electrodes in lithium-ion batteries: A first-principles theoretical study. *Nano Letters*, 11(7):2962–2967, July 2011b. ISSN 1530-6984. doi: 10.1021/nl201501s. URL http://dx.doi.org/10.1021/nl201501s.

[Zhao et al.(2012a)Zhao, Pharr, Wan, Wang, Kaxiras, Vlassak, and Suo] Kejie Zhao, Matt Pharr, Qiang Wan, Wei L. Wang, Efthimios Kaxiras, Joost J. Vlassak, and Zhigang Suo. Concurrent reaction and plasticity during initial lithiation of crystalline silicon in lithium-ion batteries. *Journal of The Electrochemical Society*, 159(3):A238–A243, January 2012a. ISSN 0013-4651, 1945-7111. doi: 10.1149/2.020203jes. URL http://jes.ecsdl.org/content/159/3/A238.

[Zhao et al.(2012b)Zhao, Tritsaris, Pharr, Wang, Okeke, Suo, Vlassak, and Kaxiras] Kejie Zhao, Georgios A. Tritsaris, Matt Pharr, Wei L. Wang, Onyekwelu Okeke, Zhigang Suo, Joost J. Vlassak, and Efthimios Kaxiras. Reactive flow in silicon electrodes assisted by the insertion of lithium. *Nano Letters*, 12(8):4397–4403, August 2012b. ISSN 1530-6984. doi: 10.1021/nl302261w. URL http://dx.doi.org/10.1021/nl302261w.

Seyed Mostafa Khosrownejad

Chemin des Falaises 3, 1005 Lausanne, Switzerland

EDUCATION

École Polytechnique Fédérale de Lausanne Lausanne– Switzerland
PhD. in Mechanical Engineering *Oct. 2012 – Now*

- Research project: *'Plasticity and fracture in Silicon anode for Li-ion batteries'* under supervision of *Prof. W.A. Curtin*

University of Stuttgart– Polytechnic University of Catalonia Stuttgart– Barcellona
M. Sc. in Computational Mechanics *Sep. 2009 – May 2011*

- Thesis title: *'Dissipative phenomena in electro active polymers'* under supervision of *Prof. C. Miehe*
- Grades average in Germany: *1.06*, Total grades average: *93/100*

Ferdowsi University of Mashhad Mashhad, Iran
M. Sc. in Mechanical Engineering *Sep. 1999 – Jun. 2006*

- Thesis: *'Multiscale simulation of nanoindentation in pure Nickle'*
- Graduated as the second ranked student in bachelors with GPA *16.4/20*.

HONORS AND AWARDS

- Full financial support from Mechanical Eng. doctoral school of EPFL. *Oct. 2012 – Now*
- Erasmus Mundus scholarship from European Commission(*€42.000*). *Sep. 2009 – Jun. 2011*
- Ranked among top 0.2% of about 500,000 participants in university entrance exam. *Sep. 1999*

PUBLICATIONS

Refereed Journal publication:

1. KHOSROWNEJAD, S.M.; CURTIN, W.A. [2015]: *Model for Charge/Discharge-Rate Dependent Plastic Flow in Amorphous Battery Materials.* Journal of the Mechanics and Physics of Solids, Under review.
2. SETOODEH, A. R.; KHOSROWNEJAD, S.M.; MALEKZADEH, P. [2011]: *Exact nonlocal solution for postbuckling of single-walled carbon nanotubes.* Physica E: Low-dimensional Systems and Nanostructures, 43: 1730–1737.
3. SETOODEH, A. R.; ATTARIANI, H.; KHOSROWNEJAD, S.M. [2008]: *Nickel nanowire under uniaxial loads: A Molecular Dynamics simulation study.* Journal of Computational Material Science, 44: 378–384.

Conference publications:

4. KHOSROWNEJAD, S.M.; CURTIN, W.A. [2016]: *Investigation of crack propagation mechanism in amorphous LiSi alloys using molecular dynamics.* 24th International Congress of Theoretical and Applied Mechanics (XXIV ICTAM).
5. KHOSROWNEJAD, S.M.; CURTIN, W.A. [2016]: *Molecular dynamics simulation of fracture in amorphous Li-Si alloys.* European Conference on Fracture (ECF 21).
6. KHOSROWNEJAD, S.M.; CURTIN, W.A. [2014]: *Plasticity in silicon anodes towards the design of Lithium ion batteries.* 11th World Congress on Computational Mechanics (WCCM XI).

7. Setoodeh, A. R.; Khosrownejad, S.M.; Setoodeh, H. [2010]: *Investigation of size effects on the tensile behavior of SiC nanowires.* Proceeding of 4th International Conference on Applications of Traditional and High Performance Materials in Harsh Environment(Sharjah, UAE).
8. Setoodeh, A. R.; Attariani, H.; Khosrownejad, S.M. [2008]: *Molecular dynamics simulations of Bauschinger effects on a defect free single crystal Nickel.* Proceeding of International Conference on MEMS and Nanotechnology (ICMN) (Kuala Lumpur, Malaysia).
9. Setoodeh, A. R.; Sazegaran, M.; Khosrownejad, S.M. [2008]: *Multiscale modeling of nanoindentation with continuum verification.* Proceeding of 4th Iranian Student Conference on Nanotechnology.
10. Setoodeh, A. R.; Attariani, H.; Khosrownejad, S.M. [2007]: *Molecular dynamic simulation of tension in a defect free Argon nanowire.* Proceeding of 15th International Conference of Iranian Society of Mechanical Engineers (ISME).
11. Khosrownejad, S.M.; Jafarnejad, M.; Farshidianfar, A. [2004]: *Fuzzy distributed-lumped modeling with application on uncertain frequency analysis of power transmission system.* Proceeding of 5th Iranian Conference on Fuzzy Systems.

Job and Teaching Experiences

Technical University of Munich Munich, Germany
Research Assistant *Jun. 2011 – May 2012*

Ahar Power Station Service Co.[1] Mashhad, Iran
Design engineer *Mar. 2008 – Sep. 2009*

Faraz Sanat Iria Co.– Faraz Sanat Applied Science University[2] Mashhad, Iran
Sales engineer and Lecturer of industrial automation courses *Dec. 2004 – Feb. 2008*

Ferdowsi University of Mashhad Mashhad, Iran
Teaching Assistant *Jan. 2002 – Dec. 2004*

References

Professor William A. Curtin
Head of Laboratory for Multiscale Mechanics Modeling, EPFL *Lausanne, Switzerland*
Email: william.curtin@epfl.ch; Phone:+41-(0)21-69 37366

Professor Dr.–Ing. Christian Miehe
Head of Chair I of Applied Mechanics in University of Stuttgart *Stuttgart, Germany*
Email: cm@mechbau.uni-stuttgart.de; Phone:+49-(0)711-685 66379

Professor Alireza Setoodeh
Assistant Professor in Shiraz University of Technology *Shiraz, Iran*
Email: setoodeh@sutech.ac.ir; Phone:+98-(0)711-726 4102

---

[1] http://www.aharco.com

[2] http://www.fsiria.ir